UC Santa Barbara
UC Santa Barbara Electronic Theses and Dissertations

Title

Controlling and Characterizing the Impact of Dislocations on the Reliability of InAs Quantum Dot Lasers

Permalink

https://escholarship.org/uc/item/3t5236xk

Author

Hughes, Eamonn Thomas

Publication Date

2023

Peer reviewed|Thesis/dissertation

eScholarship.org Powered by the California Digital Library
University of California

UNIVERSITY OF CALIFORNIA

Santa Barbara

Controlling and Characterizing the Impact of Dislocations on the Reliability of InAs Quantum Dot Lasers

A dissertation submitted in partial satisfaction of the

requirements for the degree Doctor of Philosophy

in Materials

by

Eamonn Thomas Hughes

Committee in charge:

Professor John E. Bowers, Chair

Professor Kunal Mukherjee

Dr. Robert W. Herrick

Professor James S. Speck

December 2023

The dissertation of Eamonn Thomas Hughes is approved.

James S. Speck

Robert W. Herrick

Kunal Mukherjee

John E. Bowers, Committee Chair

December 2023

Controlling and Characterizing the Impact of Dislocations on the Reliability of InAs Quantum Dot Lasers

Copyright © 2023

by

Eamonn Thomas Hughes

ACKNOWLEDGEMENTS

The results I present and discuss in this thesis would not have been possible without the support from the countless individuals I've worked with throughout my graduate years. I cannot name them all (mostly due to spotty memory), but here I will attempt to credit those who have been the most instrumental in getting me to this point.

First, to my thesis committee, I am deeply grateful for the years of guidance and feedback on my work. Especially to my advisors Prof. Kunal Mukherjee and Prof. John Bowers. Kunal was one of the key reasons I chose to study at UCSB. His passion and enthusiasm for research is infectious and could always be relied on as an infinite font of motivation and clarity whenever I felt adrift. After moving to Stanford a few years into my Ph.D., he maintained a deep and detailed interest in my research work, even as it began to diverge from his group's core efforts. His knowledge of dislocations and materials science is humbling and was a key contributor to many of the results discussed here. John became directly involved just before Kunal's move to Stanford when he very graciously took on responsibility for my funding and advising at UCSB. A near peerless expert in silicon photonics, John has been a guiding north star for my research work, ensuring I stayed on track to solving the most critical reliability challenges for our lasers and avoiding drifting off into what I found personally interesting at the moment. He has also been extremely generous with his personal time and resources to help us group members unwind and forge stronger ties, from yearly ski trips, sailing outings, and hiking excursions to annual holiday parties and other celebrations at his home. Dr. Robert (Bob) Herrick has also been an immense aid to my work with his profound expertise in laser reliability and dedication to seeing me make the most out of my research hours. Over the last several years, Bob has set aside countless hours of his own personal time through monthly

meetings and email follow-up keeping up with my research to provide extensive feedback and advice on specific experimental best practices and the wider context of device reliability. Finally, Prof. James (Jim) Speck, who has served on my committee from the start, has repeatedly posed probing questions and offered deep insights to improve my work. His two courses on x-ray diffraction theory and experiment have also been immensely edifying.

Next, I must thank the MBE growers in Bowers group—Justin Norman, Chen Shang, Mario Dumont, Daehwan Jung, Rosalyn Koscica, and recently Alec Skipper for their tireless efforts keeping the growth chambers in (mostly) working order and providing me with samples for my own experiments. Kurt Olsson and John English also played an essential role here. The cleanroom team, including Yating Wan, Kaiyin Feng, M.J. Kennedy, and Jon Peters, have also been essential for taking the massive task of device fabrication out of my hands and letting me focus my time on device reliability and failure analysis experiments. Jennifer (Jenny) Selvidge deserves a special mention for passing along her extensive knowledge of FIB and TEM and for inaugurating much of the work I continued in the years after. I'll always look back with fondness and frustration at the quite considerable amount of time we spent co-writing two of our most significant papers and the countless rounds of rewrites, revisions, and resubmissions. Brian Haidet also deserves special thanks for acting as an informal mentor during my first couple years of graduate school and early forays into MBE growth. His boundless enthusiasm for research and deep intellectual curiosity very nearly outweigh his disturbing passion for puns.

I also need to thank all remaining members of the Bowers and Mukherjee groups (past and present) for their contributions and feedback on my work, particularly (Bowers group) Andrew (Andy) Netherton, Joel Guo, Ted Morin, Zeyu (Robert) Zhang, Chao Xiang, Paolo

Pintus, and Warren Jin and (Mukherjee group) Leland Nordin, Lillian Hughes, Jarod Meyer, Pooja Reddy, Haoxue Yan, Tri Nguyen, Eveline (Evi) Postelnicu, and Kelly Xiao. I am also deeply grateful to all the facility and university support staff for keeping tools and administration running smoothly in the background. In particular to Aidan Taylor, Tom Mates, Claire Chisholm, Ravit Silverstein, and Arda Genc in the microscopy facility for always being generous with their time for guidance on experiments and trainings and for keeping the tools in top condition. And finally, all my family and friends, though not always up to date on the latest minutia of my research, have been a constant source of stability and sanity these last many years, and I am deeply indebted to all of them.

Several chapters of this thesis reproduce co-authored material that has been previously published elsewhere. In Chapter 3, which is reproduced from J. Appl. Phys. 125, 165702 (2019), with the permission of AIP Publishing, I performed the majority of cathodoluminescence experiments, data analysis, and manuscript writing. In Chapter 4, reproduced from Appl. Phys. Lett. 117, 122101 (2020), with the permission of AIP Publishing, I performed ECCI experiments, co-authored half of the manuscript text and figures, and refined the dislocation trapping mechanism. In Chapter 5, reproduced from Appl. Phys. Lett. 118, 192101 (2021), with the permission of AIP Publishing, I performed the aging experiments and data processing and co-authored half of the manuscript text and figures. In Chapter 6, reprinted with permission from Cryst. Growth Des. 2022, 22, 5852−5860. Copyright 2022 American Chemical Society, I performed ECCI characterization and led the experiment conception and manuscript writing. Chapter 7 is reproduced from *Phys. Status Solidi A.* 2023, 2300114, in which I performed ECCI and APT experiments, analyzed data, and contributed to manuscript preparation and editing. A manuscript based on Chapter 8 has

been submitted and accepted at Nanoscale but is not yet published as of this writing, for which I performed the laser aging, degradation characterization, and manuscript preparation.

Curriculum Vitae of Eamonn Hughes

December 2023

EDUCATION

Ph.D.	University of California, Santa Barbara Electronic & Photonic Materials, 2023 Advisors: Prof. Kunal Mukherjee & Prof. John E. Bowers
B.S.	University of Pittsburgh Materials Science and Engineering, 2017 Suma Cum Laude

HONORS AND AWARDS

36th North American Conference on MBE, Best Student Paper	Sep 2022
62nd Electronic Materials Conference, Best Student Paper Award	Jun 2020
ASM International Outstanding Junior and Senior Awards	Feb 2016, 2017
ASM Young Member's Night Poster Competition, 3rd Place	Feb 2016
PPG Summer Research Fellowship	Oct 2015
University of Pittsburgh Honors Full Tuition Scholarship	Mar 2013

SELECTED PUBLICATIONS

- E. T. Hughes, G. Kusch, J. Selvidge, B. Bonef, J. Norman, C. Shang, J. E. Bowers, R. A. Oliver, K. Mukherjee, "Dislocation-induced structural and luminescence degradation in InAs quantum dot emitters on silicon," *physica status solidi (a).* **220**, 2300114 (2023).
- E. T. Hughes, M. Dumont, Y. Hu, D. Liang, R. G. Beausoleil, J. E. Bowers, K. Mukherjee, "Dislocation formation and filtering in III-V regrowth on GaAs bonded on Si," *Cryst. Growth Des.* **22**, 5852 (2022).
- E. T. Hughes, B. B. Haidet, B. Bonef, W. Cai, K. Mukherjee, "Pipe-diffusion-enriched dislocations and interfaces in SnSe/PbSe heterostructures," *Phys. Rev. Mat.* **5**, 073402 (2021).
- C. Shang, E. T. Hughes, Y. Wan, M. Dumont, R. Koscica, J. Selvidge, R. Herrick, A. C. Gossard, K. Mukherjee, J. E. Bowers, "High-temperature reliable quantum-dot lasers on Si with misfit and threading dislocation filters," *Optica* **8**, 749 (2021).
- J. Selvidge, E. T. Hughes, J. C. Norman, C. Shang, MJ. Kennedy, M. Dumont, A. Netherton, Z. Zhang, R. Herrick, J. E. Bowers, K. Mukherjee, "Reduced dislocation growth leads to long lifetime InAs quantum dot lasers on silicon at high temperatures," *Appl. Phys. Lett.* **118**, 192101 (2021).

- J. Selvidge, J. Norman, E. T. Hughes, D. Jung, A.A. Taylor, M. J. Kennedy, R. Herrick, J. E. Bowers, K. Mukherjee, "Defect filtering for thermal expansion induced dislocations in III-V lasers on silicon," *Appl. Phys. Lett.* **117**, 122101 (2020). **[Editor's Pick]**
- E. T. Hughes, R.D. Shah, and K. Mukherjee, "Glide of threading dislocations in (In)AlGaAs on Si induced by carrier recombination: Characteristics, mitigation, and filtering," *J. Appl. Phys.*, 125, 165702 (2019). **[Editor's Pick]**

CONFERENCE PRESENTATIONS

- "Gradual degradation via dislocation microloop formation in InAs quantum dot lasers on Si and GaAs," *65th Electronic Materials Conf.* (2023).
- **[Best student paper]** "Controlling dislocation formation and dynamics in GaAs-based films on silicon via indium alloying," *36th North American Conf. on Molecular Beam Epitaxy* (2022).
- **[Honorable mention for best student presentation]** "Dislocations altering the microstructure and luminescence of InAs quantum dots on silicon," *64th Electronic Materials Conf.* (2022).
- "Enhancing the reliability of InAs QD lasers on silicon," *63rd Electronic Materials Conf.* (2021).
- **[Best student paper]** "Compositional changes at dislocations and interfaces in heteroepitaxial semiconductors studied by atom probe," *62nd Electronic Materials Conf.* (2020).
- "Reducing unwanted motion of dislocations toward reliable III-V devices on silicon," 61st *Electronic Materials Conf.* (2019).

ABSTRACT

Controlling and Characterizing the Impact of Dislocations on the Reliability of InAs Quantum Dot Lasers

by

Eamonn Thomas Hughes

Silicon photonics has over the past decade dramatically expanded in scale and importance and now plays a key role in optical communications for data centers, with many longer-term applications such as LIDAR, optical computing, and biomedical sensing. Monolithically integrated light sources based on III-V alloys grown directly on silicon have for decades been a goal in the field, but this has only recently become a commercially feasible approach after steady reductions in defect densities for III-V-on-Si epitaxy and the introduction of quantum dot (QD)-based active regions.

This work focuses on improving the reliability of such InAs QD lasers on silicon by understanding their fundamental degradation mechanisms, particularly by studying the evolution and impacts of dislocations. Indium alloying of AlGaAs is demonstrated to halt most dislocation motion and dramatically slow all remaining dislocations via an alloy hardening effect. This leads to the most significant finding of this work: describing a formation mechanism for misfit dislocations around the active region of QD lasers and devising a solution. The misfit dislocations form, in part, due to dislocation pinning through the active region, so thin indium alloyed layers, termed trapping layers, are inserted to extend the pinning

effect and displace the dislocations away from the active layers. This yields notable performance improvements but more importantly enhances the reliability of lasers by up to 100×. These trapping layers are later employed for defect reduction in a heterogeneous integration scheme for templated regrowth. The impacts of misfit and threading dislocations on QD luminescence beyond non-radiative recombination is also explored.

The source of lingering gradual degradation in QD lasers is clarified through electroluminescence and TEM imaging of aged and unaged lasers. Degradation is spread uniformly across the laser and is caused by growth of non-visible point defects, some of which coalesce into observable dislocation loops. Trapping layers are also explored in quantum well (QW) lasers on silicon to enhance defect filtering and reliability, but it is expected that untrapped misfit dislocations and remaining threading dislocations will limit reliability of such devices. Finally, suggestions are made for future work to improve QD laser reliability by optimizing trapping layer performance and addressing point-defect-based degradation.

TABLE OF CONTENTS

1. Introduction and Background 1

2. Experimental Techniques 9

I. Introduction 9

II. Molecular Beam Epitaxy (MBE) 9

III. X-Ray Diffraction (XRD) 10

IV. Electron microscopy 12

Scanning Electron Microscopy (SEM) 13

Transmission Electron Microscopy (TEM) 18

V. Focused Ion Beam (FIB) 23

VI. Laser Diode Aging 24

VII. Electroluminescence (EL) imaging 25

3. Controlling the Motion of Dislocations in Films and Devices via Indium Alloying ... 28

I. Introduction 28

II. Experiment Details 30

III. REDG in AlGaAs heterostructures on Si 34

General Features 36

Temperature Dependence 36

Beam Current Dependence 37

Comparison with Prior Measurements of REDG in Bulk GaAs Crystals 38

IV. Metamorphic Indium-Alloyed Heterostructures..40

V. Prospects for dislocation filtering 43

VI. Conclusions 45

4. Enhanced Dislocation Filtering using Indium-Alloyed Trapping Layers 46

I. Introduction 46

II. Proof of Concept with a Model Structure 47

III. Dislocation Filtering in Full Laser Structure 52

IV. Conclusions 60

5. Reliability Impacts of Trapping Layers.. 61

I. Introduction 61

II. Experimental Background 62

III. Enhanced Reliability due to Trapping Layers 65

IV. Plan-View STEM Analysis of Degradation...67

V. Conclusions 73

6. Trapping Layers for Regrowth after Heterogeneous Bonding 74

I. Introduction 74

II. Experimental Details...75

III. Dislocation-Filter-Free Structures 76

IV. Strained Dislocation Trapping Layers 80

V. Dislocation Formation and Trapping Layer Mechanisms...................................88

VI. Alternative Filter Designs and Device Considerations 91

VII. Conclusions 93

7. Structural and Luminescent Impacts of Dislocations 95

I. Introduction 95

II. Sample Details and Experimental Methods 97

III. Recombination Dynamics at Dislocations 99

IV. In-Situ View of Recombination-Enhanced Dislocation Glide 104

V. Impact of Remote Misfit Dislocations on Quantum Dot Formation 105

VI. Growth Modification Near Threading Dislocations 110

VII. Conclusions 116

8. Gradual Degradation in InAs QD Lasers on GaAs and Si 117

I. Introduction 117

II. Laser Aging Trends and Optical Characterization 118

Aging Behavior 118

Electroluminescence 120

III. Microstructural Characterization 122

IV. Dislocation Loop Formation and Possible Mitigations 127

V. Conclusions 130

9. Summary and Future Directions 131

I. Summary of Findings 131

II. Further Addressing Point-Defect Degradation......137

III. Optimization of Trapping Layers......140

IV. Feasibility of a Reliable QW Laser on Silicon with Trapping Layers......147

V. Conclusion......150

10. References...... 151

1. Introduction and Background

The worldwide demand for data is growing rapidly, driven by video streaming, cloud computing, and remote data storage. Data centers, serving the vast majority of this demand, are becoming increasingly centralized, and with the rise of machine learning and cloud computing, the demands on intra-site communication links are expanding rapidly. Long-haul wired data transmission has for several decades now relied on optical links rather than their electrical counterparts. Very short-distance communication links are still dominated by electrical transmission. This is primarily due to the rapid decay in electrical signal integrity with distance, particularly at high frequencies. Optical transmission is far more economical at long distances, taking advantage of the high frequency near-IR carrier waves for high-bandwidth data transmission through optical fibers with extremely low loss [1]. As increasing data rates rapidly raise power requirements for electrical data transmission, these links, particularly at intermediate distances between server racks and within racks themselves, have increasingly transitioned to optical data transmission [2].

The component size, cost, and power consumption required for transducing optical and electrical signals have historically limited optical data transmission to long range applications, but improved miniaturization and integration are increasingly making optical data transmission viable at shorter and shorter distances. In particular, the photonic integrated circuit (PIC)—a device which incorporates multiple optical components such as waveguides, modulators, detectors, and increasingly lasers on a single chip—is driving this revolution. The concept is analogous to traditional electronic integrated circuits (ICs), swapping electrons for photons as the basis for information processing and data transmission [3]. Integrating these

systems on silicon, termed silicon photonics, allows for leveraging the vast knowledge base and infrastructure behind silicon CMOS processing [2] and enables close integration with electrical circuits. The evolution of these platforms is shown in Figure 1.1, with silicon-based platforms in particular undergoing rapid development and gaining widespread interest from industry in recent years. Silicon photonics also has many applications beyond optical communications, such as LIDAR [4], [5], for environmental mapping and autonomous driving; optical computing [6], [7], for example for optical neural networks to reduce energy costs for training and operating machine learning systems; various quantum applications, including communications, computing, and sensing [8]–[11]; and many others [12].

Besides the adjacent benefits of CMOS technology, silicon also makes an excellent platform for photonics since it is transparent in the infrared and has a high-quality oxide for fabrication of waveguides and can support modulators [13] and detectors [14]. Due to its indirect band gap, however, silicon makes a very poor light source. Lasers are therefore commonly built around a separate material system, typically the highly developed and very

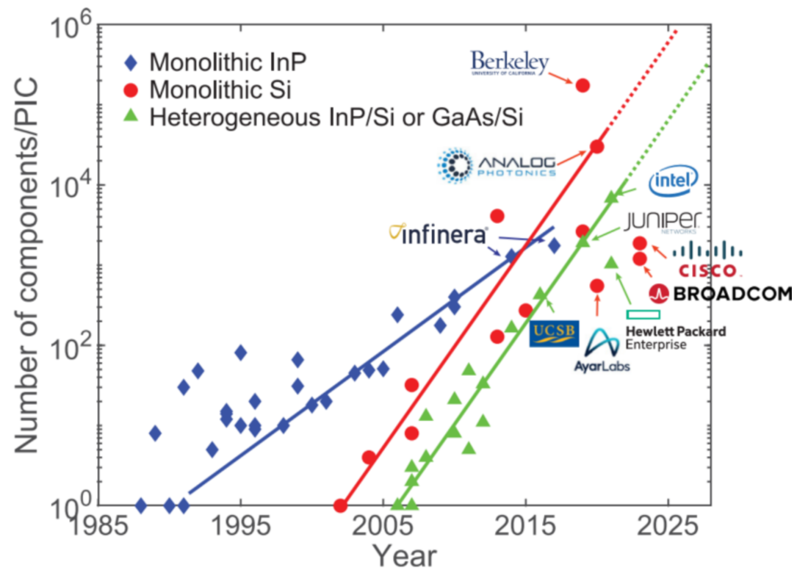

Figure 1.1. Advancement in the complexity of photonic integrated circuits (PICs) over time for InP- and silicon-based platforms. After [2].

efficient III-V materials, and integrated with silicon in one of several ways. The first, hybrid integration, involves growth and fabrication of discrete devices and then aligning and bonding the devices on a silicon platform. A more scalable and cost-effective approach is heterogenous integration, in which a full unprocessed wafer with an epitaxially grown laser structure is bonded to silicon and lasers are subsequently fabricated. This removes the need for precise alignment when bonding and more efficiently utilizes the parallelization advantages of lithography [15]. A third method, monolithic integration, sees the III-V material grown directly on silicon, and potentially offers the lowest cost and highest scalability as lasers can be grown on large 300 mm silicon substrates rather smaller expensive III-V substrates. These latter two wafer-scale integration schemes are depicted in Figure 1.2. This thesis will focus primarily on monolithic integration.

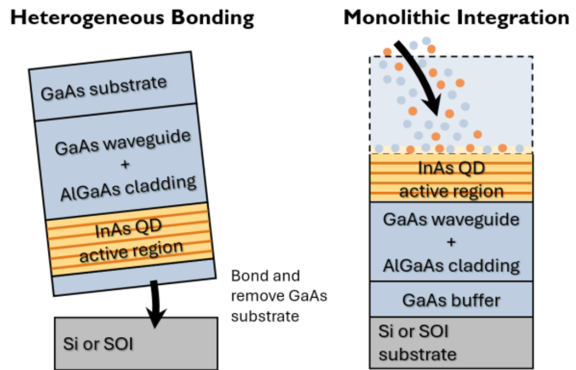

Figure 1.2. Heterogeneous and monolithic integration schemes for a QD laser.

One obvious challenge with monolithic integration is the multitude of material property mismatches between common III-Vs and silicon, summarized in Figure 1.3. Specifically, these are mismatches in lattice parameter, thermal expansion coefficient, and crystal symmetry, which lead to, respectively, high densities of threading dislocations (TDs), residual strain and cracking, and anti-phase domains (APDs). Many years of research have been devoted to solving these challenges. There has been great progress in reducing TD densities through the use of buffer layers and thermal cyclic anneals [16]–[18], and remaining TDs can be addressed with quantum dot (QD)-based active regions, which are far more defect tolerant

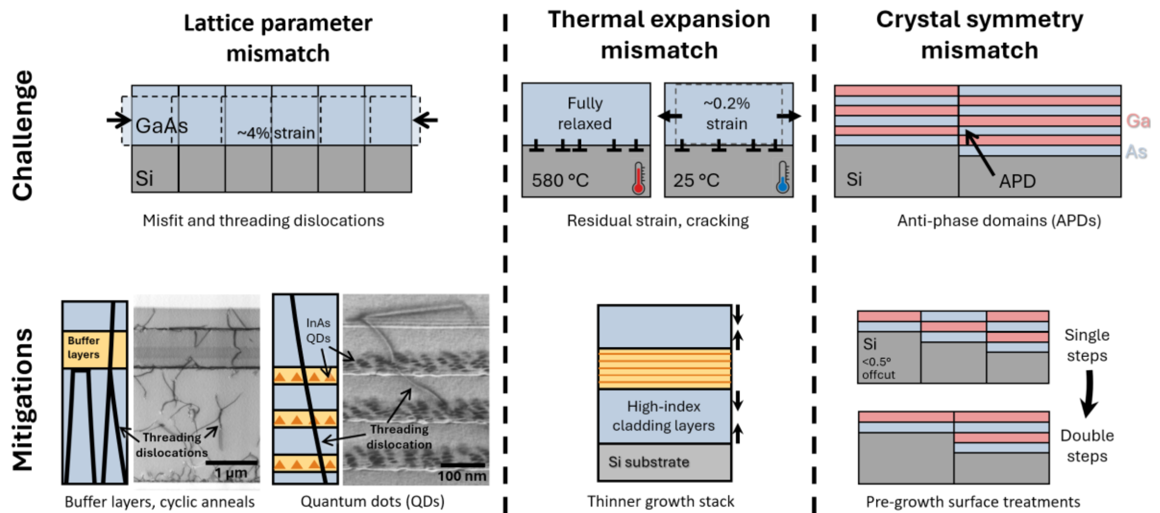

Figure 1.3. Summary of the multiple material properties mismatches between III-V (GaAs) and silicon and common mitigation methods.

compared to quantum wells (QWs) or double heterostructures (DHs) [19]. There have been extensive efforts toward developing QW lasers on silicon, but reliability is extremely low for GaAs-based devices at around 200 h [20] (and typically much shorter). InP-based devices fare better as they have different degradation mechanisms with lifetimes beyond 10,000 h, but these require excessively thick buffer layers and power conversion efficiency is very low [21]–[23]. Issues with cracking can be addressed by limiting total III-V layer thickness, e.g. by reducing buffer layer thickness [18] or using higher index cladding layers for stronger vertical confinement or by patterning the substrate before growth to confine growth to narrow stripes and allow for partial strain relief laterally. APD formation can be avoided by growing on miscut silicon substrates to promote double monolayer steps on the silicon surface over single layer steps [24]. V-grooves can also be etched into the surface to encourage merging and annihilation of APBs [25]. Neither of these methods are optimal for standard CMOS silicon processing. A solution is to grow on silicon with a slight miscut (<0.5°) and perform

specific surface treatments to promote double steps on the silicon surface before nucleating III-V [26], [27].

The improved defect tolerance of QDs is very commonly attributed to the three-dimensional carrier confinement of QDs, where once carriers enter a QD, they are relatively unlikely to thermalize out and therefore cannot reach a defect state, unless a dislocation passes through that specific dot. This is highly unlike since QD densities are on the order of 10^{10} cm^{-2} and TD densities are on the order of 10^{6} cm^{-2}. Findings by Selvidge et al. [28], however, suggest the real picture is somewhat more complicated. In this study, a single layer of QDs with an array of misfit dislocations (MDs) below it is examined by hyperspectral cathodoluminescence (CL) (Figure 1.4). Selecting just the wavelengths corresponding to ground state emission, contrast from MDs is clearly visible at room temperature indicating significant numbers of carriers are recombining non-radiatively at the dislocation from up to about 1 μm away. It is not until the sample is cooled to below 200 K that the contrast is largely faded, indicating that carriers are completely trapped by the QDs and that only the minute fraction of individual QDs neighboring the

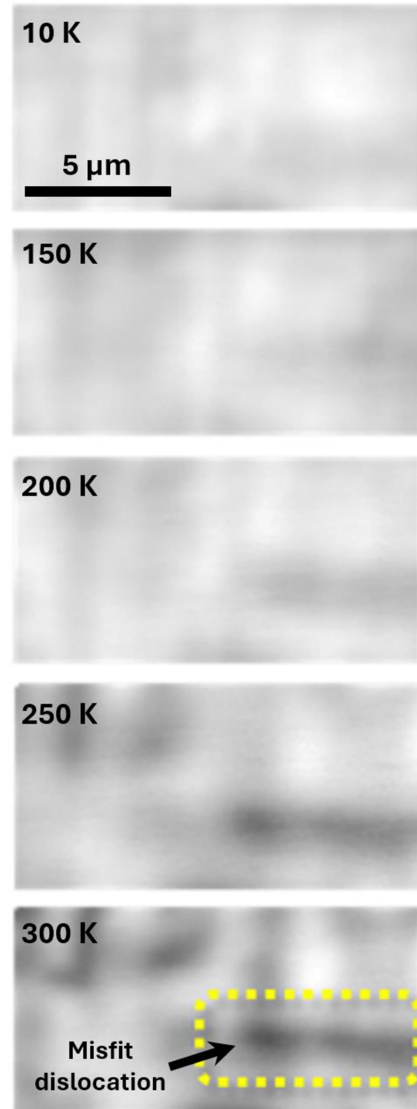

Figure 1.4. Cathodoluminescence (CL) from ground-state QD emission near to a misfit dislocation. After [28].

dislocation are affected. This suggests that at room temperature there is significant thermal mediated exchange of carriers between the QD states and the two-dimensional continuous states of the wetting layer or the encapsulating InGaAs QW enabling diffusion of carriers to the dislocation. This is not to say that QDs are not more defect tolerant than QWs, simply that their tolerance could be stronger with more strongly confining QDs. QDs on silicon do still hold large pre-aging performance advantages over QWs, which is perhaps due to reduced lateral carrier diffusion lengths from scattering and periodic trapping at QDs.

In light of this, it is perhaps not surprising that the reliability of QD lasers on silicon aged at room temperature or above is limited, particularly when defect densities are high. For example, an early aging study found laser lifetimes of just several hundred to a few thousand hours with dislocation densities of about 10^8 cm^{-2} [29]. Later efforts extended this beyond 10^6 h by reducing TD densities to 7×10^6 cm^{-2} [30], [31], which is a dramatic improvement over record QW performance on silicon of 200 h at gentler aging conditions and with a lower TD

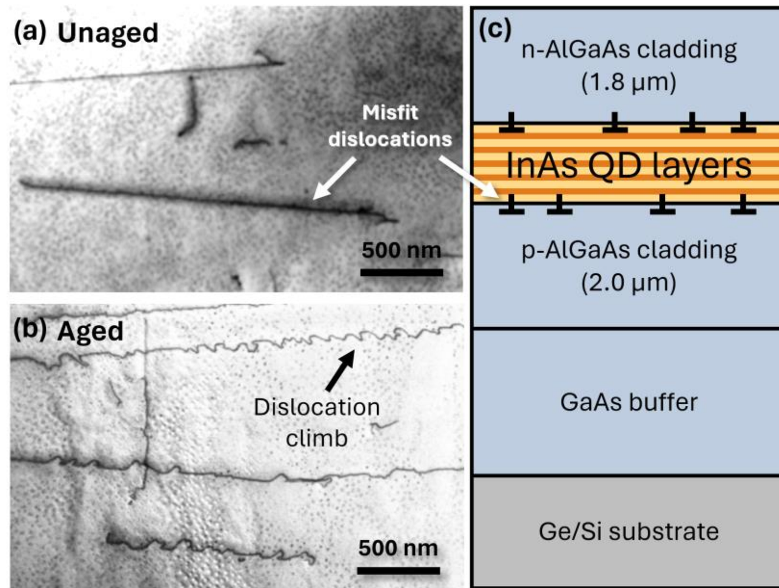

Figure 1.5. Plan-view transmission electron microscopy (TEM) of a QD laser (a) before and (b) after aging. (c) Simplified schematic of the laser structure showing misfit dislocations (MDs) above and below the active region. After [29].

density [20]. At elevated temperatures (60 °C or above), however, QD lifetimes are much shorter, once again around 1000 h. Plan-view transmission electron microscopy (TEM) shows that lasers contain MDs near the active region and that aging causes these dislocations to climb, a process in which the dislocation exchanges point defects with the matrix and changes its shape (Figure 1.5a-b). This is believed to be the primary degradation mechanism. In QW active regions, this climb would proceed unimpeded, but QDs appear to restrict dislocation climb by their strong lateral stress fields. The reason behind why these MDs form in the first place, both above and below the active reigon (Figure 1.5c) was unclear at the time. The active region was grown below the theoretical minimum thickness for relaxation, and QDs themselves largely inhibit relaxation by glide of an existing TD [32]. It was clear though that addressing this issue would be critical to further enhancing the reliability of these InAs QD lasers on silicon. This question, along with other means to enhance QD laser reliability, will be addressed in the following chapters.

In Chapter 2, a general background on the experimental techniques covered in this thesis is presented. Chapter 3 demonstrates how dislocation glide is dramatically slowed by alloy hardening through the addition of indium to an AlGaAs double heterostructure model system. Chapter 4 proposes a mechanism for how MDs form in these lasers and implements a solution to displace them away from the active region, yielding significant performance improvements. Chapter 5 extends this work by aging these modified lasers and demonstrates up to a 100× improvement to reliability at 60 °C. Chapter 6 applies the defect filtering concept from the prior two chapters to a templated heterogeneous integration regrowth process to reduce TD densities by about 30×. Chapter 7 examines the luminescent and structural impacts of dislocations via time-resolved CL and hyperspectral CL. Chapter 8 returns to the issue of

reliability of QD lasers and examines the mechanism behind gradual degradation in both lasers on silicon and on GaAs. Finally, Chapter 9 summarizes the work and discusses how to further address point-defect-based degradation, how MD trapping performance might be optimized, and whether a reliable QW laser on silicon is achievable by applying lessons learned for QD lasers.

2. Experimental Techniques

I. Introduction

This chapter will introduce and discuss the experimental techniques and tools central to this work. The techniques are presented approximately in chronological order starting with material growth by molecular beam epitaxy (MBE) and standard epitaxial material characterization by x-ray diffraction (XRD). Next, electron microscopy is summarized, including scanning electron microscopy (SEM) techniques and transmission electron microscopy (TEM) followed by focused ion beam (FIB) techniques for TEM sample preparation. The details of device fabrication are not covered since they are not a central focus of this thesis. Finally, device aging and back side electroluminescence (EL) imaging methods are discussed.

II. Molecular Beam Epitaxy (MBE)

Molecular beam epitaxy (MBE) is an ultra-high vacuum physical vapor deposition technique that enables the growth of high purity layered structures, which are the basis for most semiconductor lasers discussed in this work. The material's constituent elements are held in individual crucibles which are heated to evaporate or sublimate a steady stream of atoms or molecules onto a substrate for deposition.

The "molecular beam" of MBE refers to the direct ballistic trajectories taken by the evaporated species. At low background pressures, molecules can travel exceptionally long distances (many kilometers) before colliding with another molecule, given a sufficiently large chamber. In atmosphere, for comparison, collision distances are on the order of nanometers which results in diffusive or convective flow after evaporation. The inner chamber walls are

cooled with liquid nitrogen to minimize species bouncing around in the chamber. This enables high purity compounds to be deposited with sharp interfaces between layers by periodically blocking and unblocking the beam flux from different cells as required by the recipe.

The “epitaxy” in MBE refers to single crystal deposition that is templated to the crystal structure of the substrate. This work primarily deals with III-V compounds (GaAs, AlGaAs, InGaAs) grown on silicon and GaP/Si templates. These crystals all have similar structures, so the deposited species can neatly pattern to the substrate, effectively a continuation of the substrate crystal structure. The substrate is heated to several hundred degrees Celsius to achieve smooth, crystalline deposition with low concentrations of contaminant. The unstrained atomic spacing for the substrate and film are generally different, so defects called dislocations will form to mediate the mismatch after a certain critical thickness is exceeded.

Another technique with similar capabilities to MBE for epitaxial film deposition is metalorganic chemical vapor deposition (MOCVD), also referred to as metalorganic vapor phase epitaxy (MOVPE). This is a chemical rather than physical vapor deposition process, in which high-purity gaseous organometallic precursors (e.g. a group III atom bonded to three methyl or ethyl group) and hydride species (e.g. arsine, AsH_3) decompose on a heated substrate to grow a film.

III. X-Ray Diffraction (XRD)

X-ray diffraction (XRD) is a primary tool for characterizing epitaxial film quality and can measure properties such as lattice parameter, strain, composition (in certain cases), dislocation density, interface smoothness, and more. XRD measurements require the generation of an x-ray beam. This commonly achieved by accelerating a beam of electrons at a copper target. As long as they have sufficiently high energy, some small fraction of the electrons knock out inner

shell electrons in the copper. When an electron from the neighboring higher shell relaxes to this position, an x-ray with a wavelength of 1.54 Å is produced, referred to as $Cu_{K\alpha}$ radiation. The K refers to an electron relaxing to the innermost 1s orbital of the K shell. The α refers to the first transition to that position, in this case from 2p orbital of the L shell. This can be divided further into $K\alpha_1$ and $K\alpha_2$ due to fine structure splitting of the 2p orbital with the $K\alpha_1$ line favored for its higher intensity.

To minimize angular divergence and wavelength spread, components such as filters and collimators can be inserted, though these will reduce x-ray intensity. High-resolution single-crystal x-ray experiments require finer beam conditioning using a monochromator, which typically consists of a four-bounce single-crystal arrangement that rejects any portion of the beam with the incorrect angle or energy. This works by the principle of Bragg diffraction, which is the same principle for most x-ray measurements of the sample. Briefly, Bragg diffraction describes the phenomenon in which crystalline materials strongly scatter x-rays at precise angles related to the regular atomic planar spacing of the crystal. This occurs when x-rays scattering off of atoms in a set of planes have a path length difference equal to an integer multiple of the x-ray wavelength, known as Bragg's Law. This is expressed with the equation $n\lambda = 2dsin(\theta)$, where n is a natural number indicating diffraction order, λ is the x-ray wavelength, d is the atomic planar spacing, and θ is the angle between the x-ray beam and atomic planes on interest. The x-ray wavelengths used for experiments are comparable in length to atomic spacings, allowing for well-spaced diffraction peaks for high-resolution measurements.

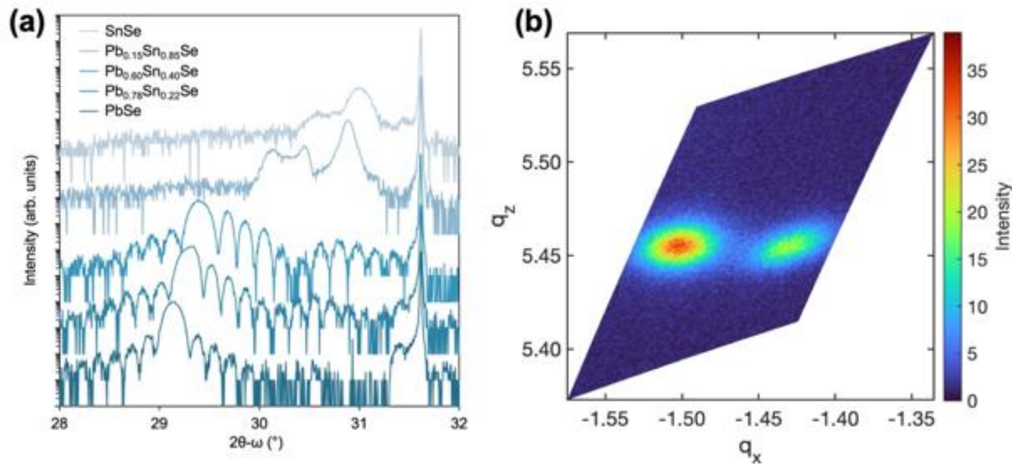

Figure 2.1. (a) High-resolution XRD of several $Pb_xSn_{1-x}Se$ films on a GaAs substrate. (b) A reciprocal space map (RSM) of an orthorhombic SnSe film showing the separation of the of the 10 0 1 and 10 1 0 peaks. Both are visible together because the film has a dual-grain structure with alternating 90° rotated grains. [Data unpublished]

Figure 2.1a shows an example of high-resolution XRD measurements of several $Pb_xSn_{1-x}Se$ films. As Sn content is increased the film changes from cubic rocksalt to orthorhombic Pnma. The fringes around the rocksalt peak near 29° for the three most Pb-rich films are a thin-film interference effect due to smooth interfaces. Figure 2.1b shows a reciprocal space map (RSM) for a SnSe film. This RSM is constructed from a series of 2θ detector scans across a range of ω sample angles and computes and maps the reciprocal lattice positions of two SnSe peaks, which here are split because of the slightly rectangular base of the orthorhombic SnSe unit cell. Both peaks are visible in a single scan since the film consists of two sets of 90° rotated grains.

IV. Electron microscopy

A core characterization technique in this work is electron microscopy. There are multiple types of electron microscopes, with the broadest distinctions being between the scanning electron microscope (SEM), in which a focused electron beam raster scans across a sample to generate signal and form an image, and the transmission electron microscope (TEM), in which a sub-micron thick sample is imaged by electrons passing through it, loosely analogous to how

optical transmission microscopes operate. Generally, the two systems are distinguished by chamber size and electron accelerating voltages, with SEM having a much larger and more versatile chamber and stage allowing imaging of bulk unprocessed samples and TEM having much higher electron energies enabling effective, high-resolution imaging in transmission. There are many sub-techniques which in some ways blur the line between these two systems, such as transmission-SEM (t-SEM), which enables scanning transmission imaging of very thin samples using an underlying detector, and secondary electron imaging in scanning TEM (STEM), but these will not be discussed here.

Scanning Electron Microscopy (SEM)

Imaging Fundamentals. The electron beam in an SEM is generated either thermionically, by heating a material such as a tungsten filament or a LaB_6 crystal to 'boil off' electrons or with a field emission gun, where a strong electric field pulls electrons out of a sharp tipped emitter. These latter sources, though they require higher vacuum and are more expensive, are much brighter than the thermionic sources and improve resolution. This initial electron beam is accelerated to between roughly 500 V and 30 kV and is refined by a sequence of lenses and apertures which help to achieve small beam probe size for improved resolution. There is a tradeoff between minimizing probe size and maximizing beam current. A typical beam probe is on the order of 1 nm. Scanning coils are used to raster the focused beam across the sample, where the size of the raster pattern defines the effective magnification.

When the high-energy primary electrons enter the sample, they interact with the material and generate a number of signals that can be collected to create different kinds of images. The most basic and fundamental signal comes from the secondary electrons, which are low energy electrons (<50 eV) generated during primary electron inelastic scattering events in the material.

Due to their low energy, only secondary electrons generated within a few nanometers of the surface can escape the material to be collected. The strength of the signal will be affected by the surface topography, hence, these electrons are used to form high resolution topographical images of the surface. The most common secondary electron detector is the Everhart-Thornley detector (ETD), which consists of an outer Faraday cage with a modest positive voltage to attract the low-energy secondary electrons. Once captured they are accelerated into a scintillator that generates pulses of light with each electron impact. These light pulses are routed to a photomultiplier tube where the signal is again converted back to electrons and is amplified. Topographic contrast from images generated with the ETD, which is offset to one side of the sample, will appear to have bright and shadowed regions as if illuminated by the ETD itself. This is because secondary electrons emitted by topographical features facing the ETD are more likely to be collected that those facing away.

Incident primary electrons can also scatter off of the dense positively-charged nucleus and backscatter out of the sample with most or all of their initial energy remaining. These are termed backscatter electrons and contain information about average atomic mass (Z-contrast) and crystal orientation. Backscatter electron detectors (BSED) are typically placed just below the microscope pole piece with an opening in the center to allow the primary electron beam through. This position is optimal for detection since backscatter yield is concentrated in the vertical direction. A common BSED is a reverse-biased silicon p–n junction which collects the multiple electrons and holes generated by the high energy electrons passing through. The ETD can also act as a BSED if the cage is biased negatively to reject all secondary electrons; however, given its small solid angle and off-vertical orientation, the signal is weak.

Improved secondary and backscatter electron imaging is achievable through the use of additional electromagnetic or electrostatic optics to collect electrons from just a narrow zone around the incident primary beam and funnel them to one or more detectors inside the lens, called through-the-lens detectors (TLD). This minimizes for example secondary electron signal generated by electrons that backscatter laterally distant from the primary beam location. This can dramatically improve spatial resolution and contrast compared to typical ETD imaging.

Characteristic x-rays have energies specific to certain electron transitions for each element and are generated when primary electrons eject core shell electrons, allowing higher shell electrons to relax to fill the hole. These enable identifying the spatial distribution of elements present in a sample through techniques such as energy dispersive x-ray spectroscopy (EDS) and wavelength dispersive spectroscopy (WDS). Spatial resolution is very poor, however, since x-rays are generated throughout a large multiple-micron interaction volume at typical beam voltages. Similarly, in semiconductor materials with a direct band gap, electrons can be excited from the valence band to the conduction band, which can recombine to generate visible, infrared, or UV light, depending on the energy of the band gap. This phenomenon is termed cathodoluminescence (CL) and will be discussed in more detail briefly.

Electron-Channeling Contrast Imaging (ECCI) is a diffraction-based imaging technique that enables non-destructive imaging of defects in bulk single crystalline and sometimes multi-crystalline materials without little or no preparation. Electron channeling is the phenomenon of the reduced backscatter electron yield that occurs at certain beam angles of incidence slightly above the Bragg angle for a set of lattice planes where the electron wavefunction has a minimum overlap with the lattice [33]. Defects in the crystal are visible because they locally

disrupt electron channeling to enhance backscatter electron yield. In practice the contrast produced at defects is extremely weak due to the large number of primary electrons that initially scatter away from the channeling condition before backscattering and due to the non-parallel nature of the focused beam itself (i.e. much of the beam intensity is angled slightly off the channeling condition). Therefore, ECCI contrast is typically best for SEMs with smaller beam convergence angles, which is more common for analytical long-working distance microscopes than for more specialized high-resolution models. Defects can be detected down to depths of a few hundred nanometers in most materials, with reduced sharpness and contrast with increasing depth.

Aligning the sample to a channeling condition is achieved with the help of the electron channeling pattern (ECP), shown in Figure 2.2a, which is a crystallographic map of the of the crystal. The ECP can be seen at low magnifications as a pattern overlaid on the crystal that is rigidly fixed to the orientation of the crystal; in other words, it remains largely unchanged when translating (for large single-crystal samples) but will move when rotating and tilting. The pattern is visible because the SEM scans by rocking the beam across the sample, changing its angular orientation to the sample across the image. Low magnification scans sweep the beam across a large angular range and produce the largest ECPs. Not all SEMs can produce ECPs as wide as shown in Figure 2.2a, which is taken at 7× magnification (20 mm horizontal field width) although some models have extra scan coils that allow for rocking with beam over a small area.

Figure 2.2b is an example of an ECCI image of a Ge buffer layer on Si, imaged in the same channeling condition shown in Figure 2.2a. Threading dislocations are visible as bright points where they exit at the surface with fading tails corresponding to the sinking segment of the

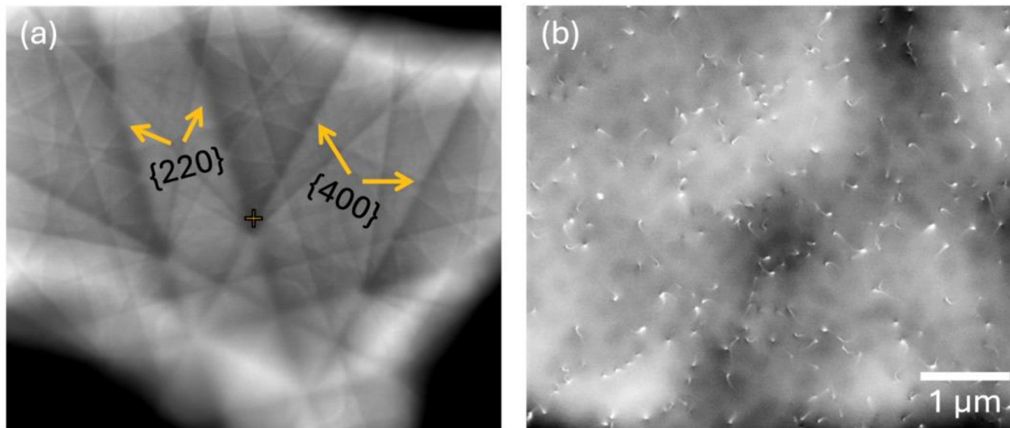

Figure 2.2. (a) Electron channeling pattern of a 001-oriented GaAs sample. Sample is tilted to bring the intersection of the 220 and 400 channeling conditions to the center. (b) Example ECCI image of a Ge buffer on silicon with a particularly high threading dislocation density of 8.8×10^{8} cm^{-2}.

dislocation. Only the top several hundred nanometers are visible to ECCI after which most primary electrons have scattered away from the channeling angle and backscatter electrons no longer exhibit channeling contrast.

Cathodoluminescence (CL). As mentioned earlier, CL is the phenomenon of the emission of light (infrared, visible, or UV) from a material excited by an electron beam. It is especially useful in semiconductors for gauging material quality. For example, non-radiative recombining defects such as dislocations appear as dark spots in CL and their size and contrast can be used to judge the non-radiative strength of the defect and parameters like carrier diffusion length and lifetime. In this way CL is a useful complement to ECCI for defect imaging; the former informs on the optical impact of defects and the latter on their structural nature. The spatial resolution of CL for defect imaging is much poorer than ECCI. Resolution is determined, first, by the volume excited by the primary electron beam and, second, by the carrier diffusion length. This first parameter can be optimized by selecting an appropriate beam accelerating voltage based on resolution required and the depth of the layer of interest. As demonstrated in Figure 2.3, however, below a certain accelerating voltage, resolution is primarily limited by

carrier diffusion length, which is set by the sample. CL imaging of infrared emitting materials is also more challenging than visible-emitters as many common photomultiplier tubes and silicon-based detectors are not sensitive far into the near-infrared.

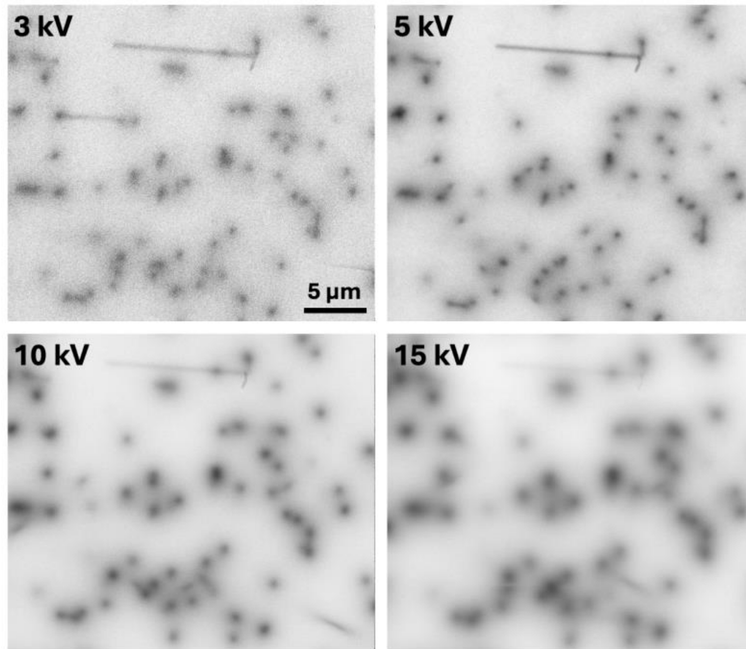

Figure 2.3. Cathodoluminescence imaging series across a range of beam accelerating voltages for an AlGaAs double heterostructure 440 nm below the surface. Lower beam energies improve resolution at the expense of signal but the improvement below 5 kV is negligible since resolution is limited by carrier diffusion. The dislocation density is approximately 1×10^{7} cm^{-2}.

Transmission Electron Microscopy (TEM)

Conventional TEM imaging is somewhat analogous to transmission optical microscopy in that both methods illuminate a sample with a radiation source and form a real image showing contrast variation in the sample. TEM swaps visible light for electrons to attain resolutions far beyond the diffraction limit of light. Unlike optical microscopy, the resolution of TEM is not limited by the wavelength of electrons, which is on the order of a picometer for common TEM electron energies. Aberrations in the electromagnetic lenses used to focus the electrons,

particularly spherical aberration, is the larger challenge, though atomic resolution imaging is readily attainable.

Electrons strongly interact with materials and can only transmit through several hundred nanometers of most materials before most are scattered away at high angles. Therefore, compared to SEM, TEM imaging requires much more intensive sample preparation to form a thin foil of material for imaging. This can be done through careful sectioning, polishing, and ion milling or more commonly now using a focused ion beam microscope, which will be discussed in the next section.

Image contrast in TEM can arise from basic mass-thickness contrast, analogous to optical microscopy, but also from diffraction in crystalline materials. Diffraction contrast can be exploited to image defects, such as dislocations, stacking faults, and anti-phase boundaries, due to the local disruption to the regular crystal structure. Electron wavelengths are much smaller than the x-ray wavelengths used for XRD, so tilt angles required to access common diffraction conditions are usually just a few degrees.

Scanning Transmission Electron Microscopy (STEM) uses a focused electron probe scanned over the sample to form an image. Multiple detectors can be inserted below the sample to capture electrons scattered at different angles, such as a central bright field detector and one or more annular dark-field detectors. Bragg scattered electrons scatter at moderate angles and contain diffraction contrast information whereas very high angle Rutherford scattering primarily provides atomic number (Z) contrast. Newer pixelated electron detectors enable a technique called 4D-STEM in which a diffraction pattern is captured at every pixel of the image, which allows for post-hoc contrast selection and reduces the need to fine tuning camera

length and diffraction pattern position for optimal contrast during imaging. In TEM, this is analogous to selecting any objective aperture position, size, or shape after the fact.

STEM has a number of advantages over conventional TEM. The use of a converged probe enables imaging thicker samples and reduces contrast from bending contours and thickness fringes, which are often distracting and undesirable. This is demonstrated in Figure 2.4. There are no strongly excited post-specimen imaging lenses required for STEM imaging, so chromatic aberrations, which arise from variable electron energy loss in the sample, are minimized.

STEM also enables diffraction contrast imaging of a sample directly on its zone axis, which provides a balanced view of contrast from all diffraction conditions that intersect the zone axis. This is particularly useful for cross section samples with thin layers, where tilting off zone to a diffraction condition can blur layers together. Also, in TEM bright- and dark-field imaging works by inserting an objective aperture to select only the transmitted or diffracted intensity. Therefore, pairs of these images must be collected sequentially. In STEM they can be collected in parallel simply by adjusting the position of the central bright field and annular dark field detectors with respect to the diffraction pattern. The scanned probe used for STEM also allows

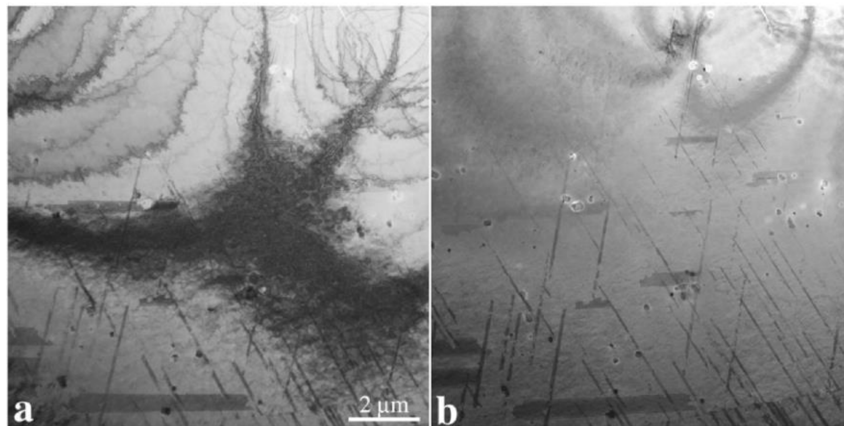

Figure 2.4. (a) TEM and (b) STEM images of the same region of a highly bent foil. The TEM image shows severe bending contours, but these are greatly minimized in the STEM image. After [97].

for integration of energy dispersive x-ray spectroscopy (EDS) and electron energy loss spectroscopy (EELS), two techniques for identifying material composition. The scanned probe also generates directly interpretable atomic resolution images, where bright contrast from a high-angle annular dark field (HAADF) detector represents atomic columns, with intensity roughly proportional to the square of atomic number. TEM atomic resolution images by contrast can undergo contrast reversals when focusing and must be compared to simulations of electron interactions with the crystal structure to correctly interpret. Finally, a simple quality-of-life advantage of STEM is the ability to arbitrarily select the scan rotation angle and aspect ratio to best align to the sample, reducing the need to image at a lower magnification to allow for later alignment and cropping.

Figure 2.5a shows an example of a diffraction pattern in STEM when aligned to the $[\bar{1}10]$ zone axis. The three sets of primary diffraction planes that intersect at this zone are labeled.

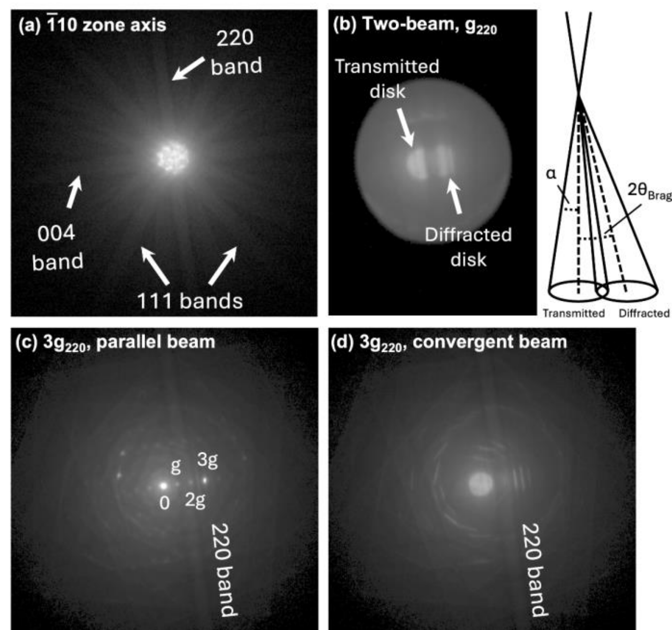

Figure 2.5. Electron beam diffraction patterns on (a) the $[\bar{1}10]$ zone axis, (b) in a two-beam g_{220} condition, and (c-d) in a $3g_{220}$ condition with (c) parallel and (d) convergent beam illumination. The inset in (b) shows how the transmitted and diffracted disks overlap for this combination of beam convergence angle (α) and Bragg angle.

Figure 2.5b shows a typical two-beam condition after tilting several degrees away from the zone axis along the 220 Kikuchi band to minimize diffraction from other conditions. Rather than diffraction spots, STEM produces diffraction disks, which overlap slightly since the beam convergence semi-angle, α, is slightly larger than the Bragg angle, θ, as depicted in Figure 2.5b inset. The $3g_{220}$ condition is excited in Figure 2.5c-d, shown for (c) a near parallel-beam condition typically encountered in TEM in and (d) a convergent beam condition seen in STEM. For the higher order 3g condition excited in Figure 2.5b, the 3g disk is very faint.

Diffraction imaging can be used to identify the Burgers vector of dislocations using a technique called **g·b** imaging. When the dot product of the diffraction vector, **g**, and the Burgers vector, **b**, is zero, the dislocation will have minimal contrast or will be invisible since in this condition the strain field of the dislocation will not significantly distort the diffracting planes. This is demonstrated in Figure 2.6 where an array of misfit dislocations in a GaAs-based sample are imaged in two 400-type diffraction conditions. In each image, there are clearly two dislocations with little to no contrast. Most dislocations in this material have a

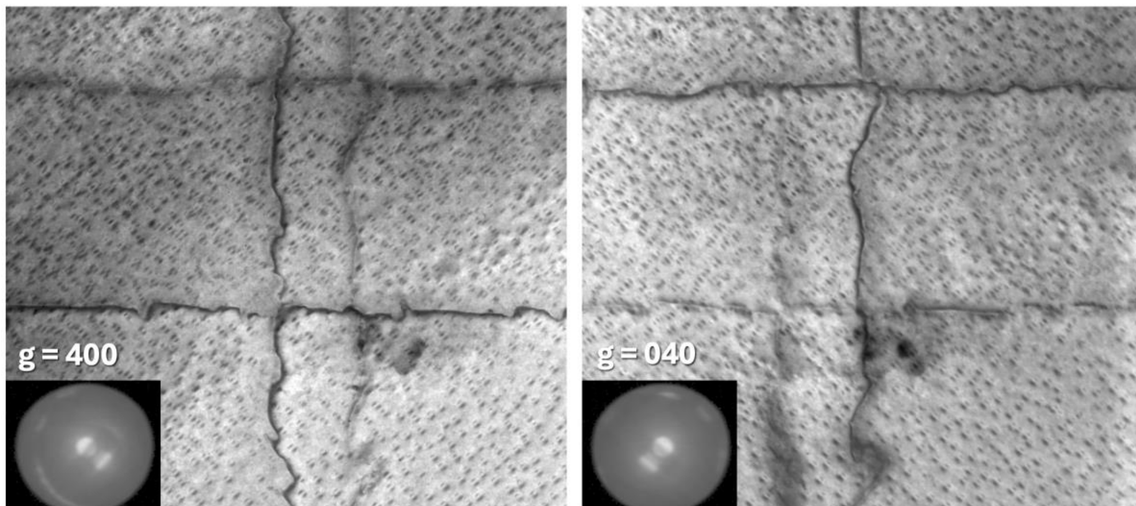

Figure 2.6. Plan-view STEM image of a misfit dislocation array demonstrating **g·b** invisibility conditions. The Burgers vector of the dislocations is of the type $\frac{a}{2}\langle 110\rangle$, so one set is invisible in each of the 400 and 040 diffractions conditions shown above.

$\frac{a}{2}\langle 110\rangle$-type Burgers vector, so in the **g** = 400 image, the Burgers vector of the invisible dislocations is $\frac{a}{2}[011]$ and in the **g** = 040 image, it is $\frac{a}{2}[101]$ (or the negative for either).

V. Focused Ion Beam (FIB)

A focused ion beam microscope operates similarly to an SEM, but swaps the electron beam for an ion beam, usually Ga ions, or Ar or other gases in the case of plasma FIB. The ion beam can image the sample through secondary electron emission, just as in SEM, but more useful, it can mill away material to form trenches. This enables the preparation of site selective TEM samples with high precision and uniformity. A FIB is commonly constructed in a dual-beam configuration with both an electron and an ion beam, allowing for high-resolution, non-destructive imaging and monitoring with an electron beam, while milling and preparing the sample with the ion beam.

Figure 2.7 shows a typical sequence to prepare a cross-sectional TEM sample. First, a thin layer of platinum is deposited by injecting a precursor gas that decomposes when exposed to secondary electron emission where the electron beam is scanning. Next, the sample is tilted to

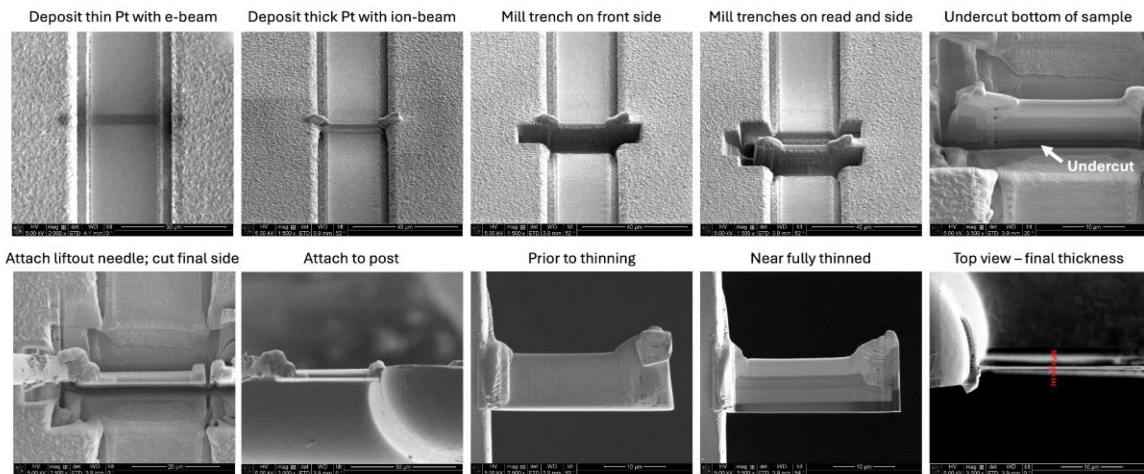

Figure 2.7. Sequence of images detailing the preparation of a cross-sectional TEM sample. All images shown here are taken with the electron-beam.

face the ion beam perpendicularly (52° stage tilt here), and a second thicker layer of platinum is deposited using the ion beam. Trenches are then milled on the front, back, and left side, after which an angled undercut is made to detach the underside of the sample. A micro-manipulator needle is then welded to the sample before milling through the final right side attachment. The sample is then moved using the micro-manipulator and welded to a removable grid post, which can be inserted in the TEM for imaging. The final steps are to thin the sample to an appropriate thickness, here approximately 390 nm. Much thinner samples are achievable, but large sections such as this become unstable and will begin to bend and twist below approximately 250 nm.

VI. Laser Diode Aging

In reliability testing of laser diodes, it is important to test a large enough set of devices to determine the statistical spread in device performance. In this work this is accomplished with an ILX LRS-9434 Laser Reliability and Burn-In Test System, referred to hereafter as an aging rack. The system contains 23 individual fixtures or ovens each of which can accommodate 16 carriers. Each carrier can address two lasers. The fixtures are all individually temperature controlled from about 35 °C to 150 °C. Devices can be tested in ACC (automatic current control) or APC (automated power control), but in the latter mode, only one device per carrier can practically be aged. Figure 2.8 provides an overview of the aging rack system, showing the individual test fixtures with carriers in place. Singulated laser dies are mounted on the AlN carriers with either a 60-40 In-Pb solder paste or an AlN-loaded or silver-loaded epoxy for high thermal conductivity.

All lasers in this work are aged in ACC mode, since this is simpler to implement and allows for testing more devices, particularly since high performing devices tend to cluster together and thus many good lasers share the same singulated die. Devices are aged at constant current

for up to 50 h before measuring a light output–current–voltage (LIV) sweep at the test aging temperature and a standard base temperature of 35 °C. This cycle is repeated for the length of the aging run, typically 2000 h, after which the recipe can be repeated if further aging is desired.

Figure 2.8. (Left) Overview of aging rack system with 7 shelves with up to 4 fixtures per shelf. (Bottom right) View of an opened fixture with 16 slots for laser carriers. The fixture head with spring-loaded contact pins and photodiodes (pictured in top right) is placed on top of this. (Top middle) Magnified view of carriers in testing slots next to a fixture head alignment pin.

VII. Electroluminescence (EL) imaging

Electroluminescence (EL) is the phenomenon of light emission in a material under electrical injection, in this case of a p-n junction of a laser. This light emission can be imaged with a microscope and camera sensitive to the appropriate wavelengths. The top-contact devices discussed in this work must be imaged from the bottom through the substrate, so the underside must be smooth, and all layers must be transparent to the device emission wavelength. EL imaging is a powerful technique since it enables rapid assessment of an entire device, to identify any regions of concentrated degradation, for example, at the laser facets or

at a defect in the bulk. None of the other methods used in this work are capable of examining more than a small area of the device (usually a 10-20 μm-long section), so EL is critical for answering two questions: (1) are a few areas of severe degradation responsible for most of the aging, or is degradation just the accumulation of many small defects? The latter proved to be true. (2) Are near-facet defects a major cause of device degradation? In QD lasers aged several milliwatts of output power, they are not. Also, the fact EL is non-destructive allows us to characterize the device before and after aging and watch how defects grow. Even though most devices degrade fairly uniformly, this is still useful information since it validates further microstructural characterization of a small sections of the device by TEM or other techniques.

Figure 2.9 shows a simple EL setup used for characterization in this work. It consists of an InGaAs camera sensitive to photons from 0.9 to 1.7 μm wavelengths connected to a set of infinity corrected objective lenses on a turret with a 90° turning mirror and a tube lens for image formation. The microscope system is mounted on a 3-axis stage with a differential drive micrometer on the z axis for fine focus adjustment. In this implementation, the microscope moves, rather than the sample and stage, due to the difficult of moving both sample and probes without damaging the device. Vibration control is essential for high resolution EL imaging and time lapse sequences, but this setup suffers slightly in this respect due to some looseness in the objective turret mechanism and mild instability of the 3-axis stage supporting the long microscope assembly. Vibration can be greatly reduced by removing the turret and screwing in a single objective directly. The stage vibration issues may be improved by using separate x, y, and z axis stages with wider bases to provide a more stable platform for the microscope. An overhead camera view of a probed device is also shown in Figure 2.9 along with an example

of an EL image from a 3 μm wide laser ridge, showing several instances of dark line defects, horizontal and vertical, that correspond to misfit dislocation near the active region of the laser.

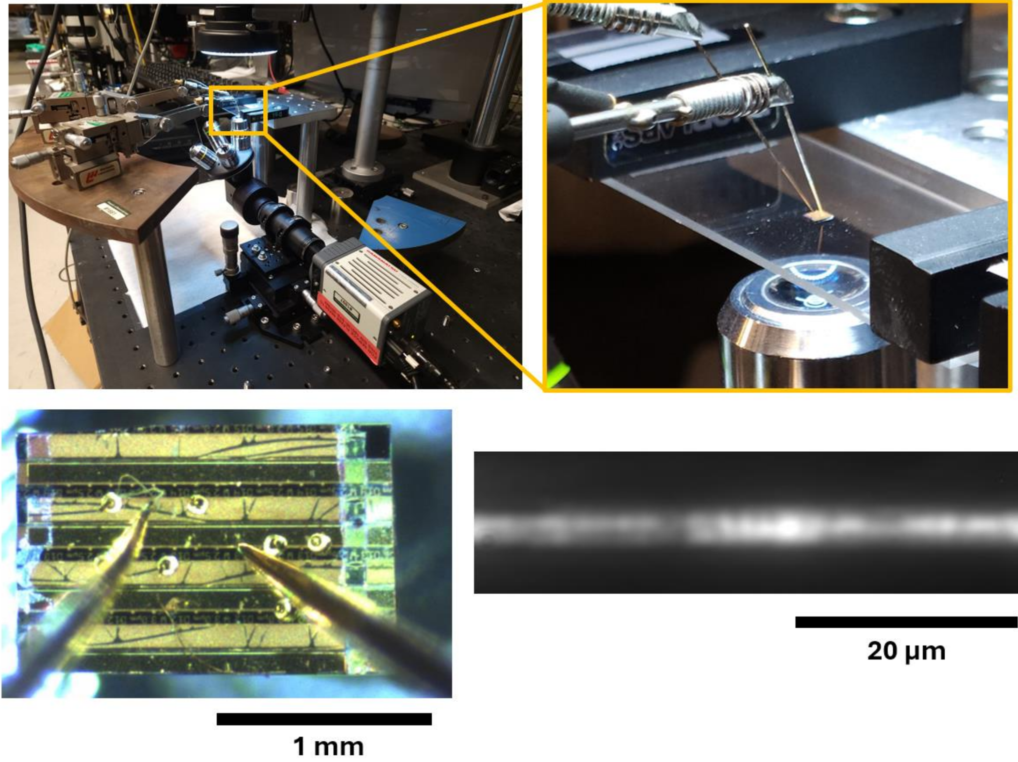

Figure 2.9. (Top) Setup used for electroluminescence (EL) imaging. (Bottom left) Top view of a probed laser during EL imaging. (Bottom right) EL image of a laser showing several horizontal and vertical dark line defects that correspond to (clusters of) misfit dislocations.

3. Controlling the Motion of Dislocations in Films and Devices via Indium Alloying

I. Introduction

There is great effort rightly spent working to reduce threading dislocation densities (TDDs) in lattice-mismatched heteroepitaxial films, such as GaAs on Si, the focus of this work. Schemes such as strained or metamorphic buffer layers [18], [34], [35], thermal cyclic annealing [16], and epitaxial lateral overgrowth [36] can help achieve very low TDDs, and as TDD is strongly correlated with device performance and reliability [30], the efforts are entirely worthwhile. But further reductions in TDD become increasingly difficult because most schemes rely on dislocation annihilation or fusion reactions which become statistically less likely as TDD is reduced. For certain device types, particularly QW-based devices, even a single dislocation may be sufficient to rapidly degrade performance [20], [37]. An additional route to dislocation engineering, beyond solely reducing total TDD, is to better understand and control the behavior and impacts of the dislocations that remain behind.

Due to a mismatch in the coefficient of thermal expansion (CTE) between III-V or Ge films (CTE = 5.7 and 5.9 ppm/K respectively at 300 K) and the Si substrate (CTE = 2.6 ppm/K at 300 K) [38], a substantial residual tensile strain of 0.15–0.2% exists in the films at room-temperature. This strain coupled with a remarkable class of processes known as recombination- or radiation-enhanced dislocation glide and climb (REDG and REDC), can enable rapid dislocation growth during device operation in these otherwise brittle materials [20], [39], [40]. These processes form part of the larger space of photoplastic effects in semiconductors relating to the strong coupling of electrical and mechanical properties of dislocations [41], [42].

A better understanding of of REDG and REDC of dislocations in III-V thin films on Si is essential for reliable monolithic integration of optoelectronic devices. Normally, dislocations cannot move (glide or climb) at room temperature in GaAs due to high energy barriers. Dislocation glide is a diffusionless process by which a dislocation can move rapidly through a crystal, effectively advancing or retracting a partially slipped plane usually in response to stress. Dislocation climb is a typically much slower diffusion-mediated process in which point defects attach or detach along the dislocation core and enable dislocation motion outside of its normal glide plane. REDG is the process by which energy released during non-radiative recombination at dislocations briefly lowers these barriers enabling rapid dislocation glide even at low temperatures [43], [44]. Here, both the initial barrier height and the extent of barrier lowering due to recombination depend on the type of dislocation. Most of our understanding of these important processes have come from the study of bulk crystals, but the density, character (line direction, Burgers vector, and core chemistry), and recombination properties of TDs generated during heteroepitaxy on silicon are not like those generated by deformation or indentation in bulk crystals. Hence, characterizing REDG in samples with dislocation configurations similar to that in heteroepitaxial devices is important to understand failure mechanisms.

A few groups have noted that adding small amounts of indium in the active region of GaAs-based quantum well lasers impedes the formation of dislocation-related dark line defects [45]–[47]. There is debate over the mechanism for this. It is not clear if indium merely reduces the residual tensile strain in the active region or if there are additional metallurgical hardening effects at room temperature. In the latter case, different mechanisms could be at play from those seen in high temperature studies (>300 °C) of plasticity on bulk crystals. Hence, a direct

study of REDG at the single dislocation level in strain-controlled indium containing samples would be useful to decouple these effects.

In this chapter, we study the dynamics of REDG of TDs in (In)AlGaAs-based double heterostructures (DH) grown on Si using scanned cathodoluminescence (CL) intensity maps. Electron-hole pairs generated by the scanning electron beam induce REDG as they recombine non-radiatively at TDs. The residual strain in the epilayers arising from CTE mismatch provides the overall driving force for glide. This chapter provides (1) a description of the REDG behavior seen in AlGaAs heterostructures on Si, (2) a demonstration of strong reduction in REDG by adding a few percent of indium in carefully designed metamorphic samples, and (3) preliminary findings from an REDG-based dislocation filtering experiment where we remove a large fraction of glissile TDs.

II. Experiment Details

We deposited our thin films on 150 mm silicon substrates offcut from [001] by 6° towards $[\bar{1}11]$ to discourage antiphase domain formation [48]. This directional notation is consistent with the orientation of the subsequent GaAs film. First, a 1.2 μm layer of germanium was grown by an Epi Centura low pressure chemical vapor deposition (LPCVD) reactor using a two-temperature step procedure [49], [50]. These samples underwent five cycles of thermal annealing between 650 °C and 850 °C. Next, 150 nm of GaAs was grown in a Thomas Swan/Aixtron metalorganic chemical vapor deposition (MOCVD) reactor with a high AsH_3 overpressure [51], [52]. These wafers were cleaved into smaller pieces and used as "pre-threaded" substrates for subsequent (In)AlGaAs film growth.

Double heterostructures with an $In_x(Al_{0.15}Ga_{0.85})_{1-x}As$ active layer and $In_x(Al_{0.25}Ga_{0.75})_{1-x}As$ barriers were used for this study; x was chosen as 0 (indium-free), 0.02, and 0.05. Figure

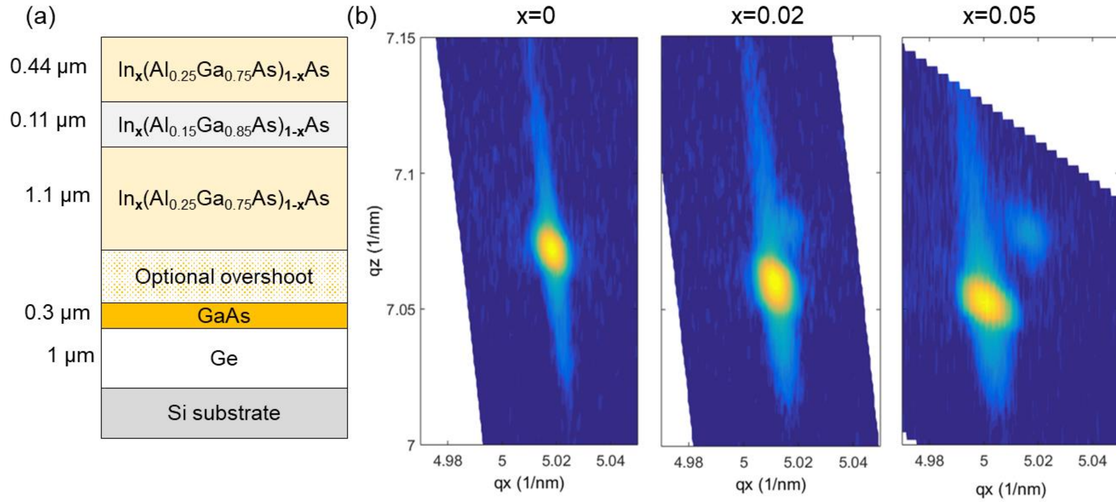

Figure 3.1. (a) Layer structure of the arsenide heterostructures on silicon. The indium-free x=0 sample is used for the detailed characterization of REDG in III.A and filtering in III.C. The indium containing x=0.02 and x=0.05 form the basis of III.B where REDG is seen to be arrested. An overshoot layer is used for a second x=0.05 sample to modify the residual strain. (b) A portion of the $\bar{2}24$ x-ray reciprocal space maps of the films for the compositions indicated. The weaker peak seen in x=0.02 and 0.05 correspond to GaAs/Ge. We used larger scans that included the Si substrate peak to calculate the residual strain at room temperature. The sample with overshoot is not shown here. After [83].

3.1(a) shows the heterostructures layer design. We include a fourth sample in our study also with x=0.05 but with the addition of an overshoot layer. This layer provided fine control of the residual strain in the x=0.05 (overshoot) heterostructure as is discussed subsequently. The films were grown at 725 °C with a V/III ratio of about 40 with H_2 as the carrier gas. The growth rates ranged from 1–1.4 nm/s, and the films were doped n-type $\approx 1\times10^{17}$ cm^{-3} using disilane. A 120 nm GaAs regrowth was performed on all samples before depositing (In)AlGaAs to reduce the effects of surface contamination from wafer cleaving and transfer. We ensure a similar starting dislocation density by growing the four DHs on “pre-threaded” substrates. The thicknesses of the lower cladding, active layer and upper cladding layers are 1080 nm, 110 nm, and 440 nm, respectively, verified by transmission electron microscopy. After the growth of the upper cladding layer, we annealed these samples at the growth temperature for 300 s in the

growth chamber to allow for maximum strain relaxation. A 3 nm thick capping layer of lattice-matched $In_xGa_{1-x}As$ was grown to prevent oxidation of the underlying Al-containing layers.

Table 1. Measured residual strain

Indium content (x)	Overshoot layer	Residual strain (tensile)
0	No	0.17%
0.02	No	0.16%
0.05	No	0.11%
0.05	Yes	0.16%

We measured the residual strain in our films using x-ray diffraction (XRD) using a Bruker D8 diffractometer with a Cu $K_{\alpha 1}$ radiation source and a linear array detector. Symmetric 004 and asymmetric $\bar{2}24$ HR-XRD reciprocal space maps (RSM) were collected and used to calculate the in-plane and out-of-plane lattice constant, while correcting for crystallographic tilt which may have developed during the growth [53]. Fig 1(b) shows the $\bar{2}24$ RSMs of the III-V layers for the three samples. The GaAs/Ge peak is distinct for the indium-containing films. Table 1 lists the measured residual tensile strain. This strain is the net effect of residual compressive strain after the high temperature processes (growth and subsequent anneal), tensile strain due to integrated CTE mismatch of 0.2%, and any plastic relief of this tensile strain during cooldown. Uncertainty in the strain measurements is ±0.02%. The lower strain in the x=0.05 sample is due to under-relaxation of compressive strain during growth. We compensated for this using the x=0.05 (overshoot) sample using an overshoot layer of $In_{0.08}(Al_{0.15}Ga_{0.85})_{0.92}As$ (200 nm).

We measured CL emission using an FEI Quanta 400F scanning electron microscope (SEM). The electron beam scan-rate parameters were chosen to match an image capture rate of one frame per second. We used a beam accelerating voltage of 5 kV for good dark spot

defect resolution and contrast. Monte Carlo simulations using CASINO [54] show that the primary beam does not penetrate all the way into the DH active layer, however electron-hole pairs generated by the beam should easily be able to diffuse into the active layer. We estimate that the carrier concentration is less than 10^{17} e-h pairs/cm^3. A mirror positioned directly above the sample directed the emitted light towards a photomultiplier tube sensitive up to about 870 nm. All CL data was taken at the same magnification, resolution, and dwell time to avoid unwanted artifacts due to the scanning nature of the probe, and we ensured that the area of interest was not exposed prior to imaging.

We measured the velocities of TDs by averaging the total distance traveled over a number of frames, with points manually chosen to ensure that the TDs were free from the influence of nearby defects. The CL contrast due to non-radiative recombination at the TDs was calculated as the positive difference in CL intensity between the TD and the bright background, normalized by the background intensity. Since no systematic or significant change in intensity was noted as the TDs moved, the CL intensity of the TDs was simply averaged from three points along the path of the moving TDs. For rapid analyses on this large dataset, we automated tracking of TDs using a single particle tracker as implemented in the Fiji plugin Trackmate [55]. Here, a Laplacian of Gaussians method detects TDs as dark spots. Tracks were established by linking TD positions using the linear assignment problem (Simple LAP) tracker. The tracking is not yet effective near tight clusters and complex crossings and hence the automated tracked images are used in a semi-quantitative manner to provide an overall view of this phenomenon.

III. REDG in AlGaAs heterostructures on Si

TDs in the indium-free (x=0) AlGaAs heterostructures on Si are very clearly visible as dark spots in cathodoluminescence images, each with an average spot diameter of approximately 1 μm when excited with a 5-kV beam. The CL contrast from dark spots is between 0.3–0.5 and relatively constant over a two-order-of-magnitude change in probe current.

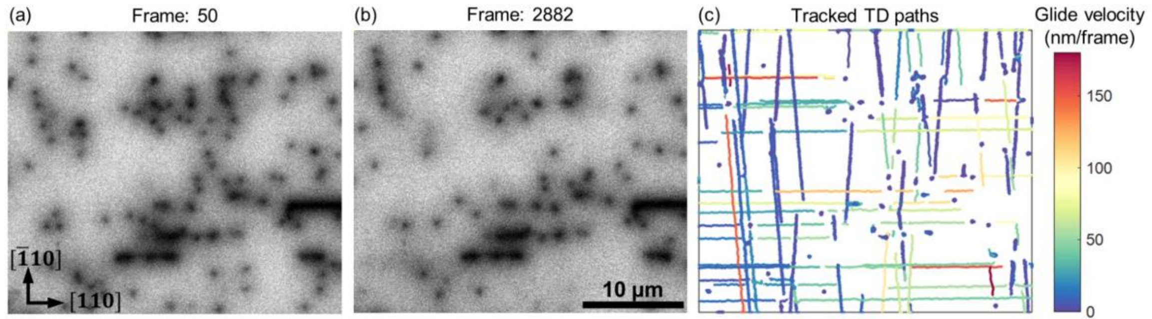

Figure 3.2. Panchromatic cathodoluminescence emission from the AlGaAs (x=0) heterostructure showing dark spots due to non-radiative recombination at threading dislocations. The images are taken with a 3 nA absorbed current and show the position of threading dislocations after (a) 50 frames and (b) 2882 frames (also in supplementary videos). A number of dislocations have exited the imaging area by REDG. (c) Tracks of the gliding TDs colored by the glide velocity. Four types of dislocation behavior are seen: slow and fast motion along $[\bar{1}10]$, fast motion along $[110]$, and stationary dislocations. The inclined lines are due to the substrate offcut. After [83].

Repeated scans from the same area reveal that a number of TDs move by glide under the influence of the scanning electron beam, an effect we ascribe to REDG [56], [57]. The driving force for REDG is the relief of tensile residual strain in the III-V layers. Importantly, we do not see a change in CL spot contrast during glide indicating that non-radiative recombination at TDs in these heterostructures is most likely intrinsic to the dislocation core as opposed to arising from an atmosphere of impurities [58]–[60]. Figs. 2(a) and 2(b) show panchromatic CL emission intensity maps at the start and end, respectively, of a 2800 frame scan, taken at one frame per second using a 3 nA sample absorbed current (also in supplementary video). A number of TDs have exited the area due to REDG and others have re-organized. Figure 3.2(c)

presents an overall view of this phenomenon in the AlGaAs heterostructure, with the tracked glide path of TDs highlighted and the color of the path corresponding to the mean velocity

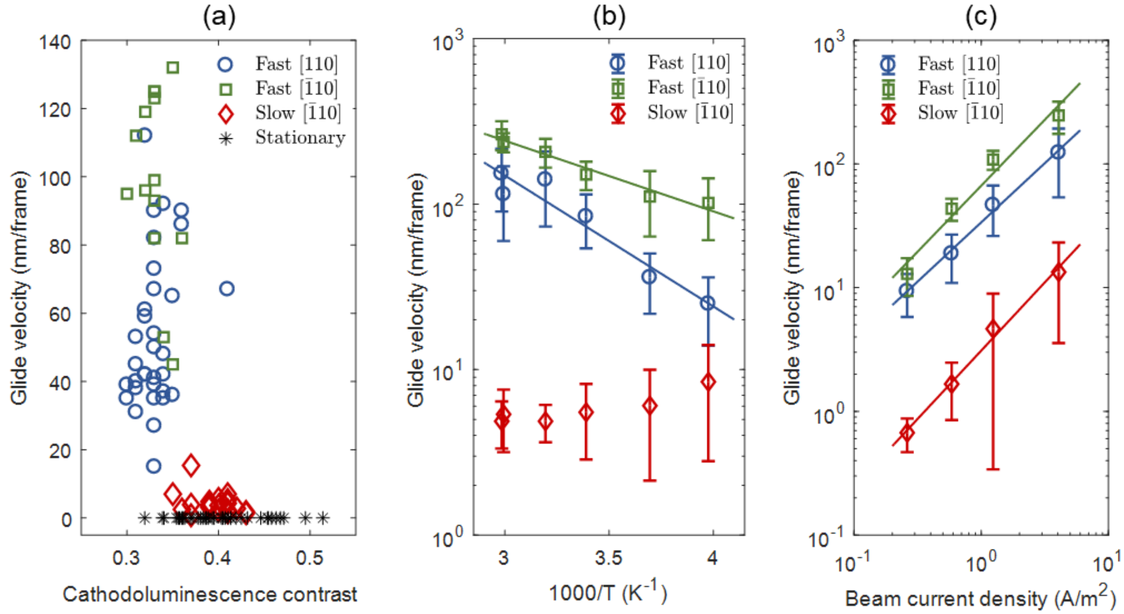

Figure 3.3. (a) Relationship between cathodoluminescence contrast due to non-radiative recombination and the corresponding REDG velocity. The sample absorbed current is 1 nA. (b) Temperature dependence of REDG velocity showing very low activation energies for the fast dislocations. The sample absorbed current is 1.5 nA. The slow dislocation glide velocity does not show appreciable temperature dependence. (c) Beam current dependence of REDG velocity showing a nearly linear dependence. After [83].

(total displacement/total time). While glide velocities are normally in units of nm/s, we use nm/frame (1 frame captured every second) as the excitation is intermittent rather than continuous due to the scanning nature of the e-beam. Finally, due to the substrate miscut, the intersection of the {111} TD glide planes and the substrate surface is no longer parallel and there are two families of MDs in the [$\bar{1}$10] direction that are slightly inclined to each other [35]. For all the discussion that follows in the paper, these slightly inclined directions are still referred to as TDs moving in the [$\bar{1}$10] direction.

General Features

For the purposes of comparison between samples used in this study, we broadly categorize TDs into one of four types: (1) slow and (2) fast dislocations, both gliding along the offcut direction of $[\bar{1}10]$, (3) fast dislocations gliding along [110], and (4) dislocations that are stationary (within the detection limit). This is seen best in Figure 3.2(c). The ratio of the number of mobile and stationary dislocations is measured as near 1:1, an important data point concerning sessile and glissile TD densities that we will return to in III.C. In the population of mobile TDs, the ratio of the number of fast [110], slow $[\bar{1}10]$, and fast $[\bar{1}10]$ TDs is approximately 2:2:1. As we have a large number of TDs imaged, we can look for correlations between the CL contrast and REDG velocity. Figure 3.3(a) shows this connection for the three types of mobile dislocations. The slow TDs have a measurably higher CL contrast in the range of 0.35–0.43 compared to both sets of fast TDs that exhibit contrast between 0.3–0.36. Yet in the class of fast TDs, we find no change in the CL contrast for an order-of-magnitude range of velocity. We think that CL contrast and REDG velocity is uncorrelated within a given category of TD, but there might be a link between non-radiative recombination and the category of TD. Interestingly, we do not see $\langle 110 \rangle$ dark line defects in the CL images that should form due to the glide of the upper parts of TDs. We think that the MDs form at some depth below the active layer of the double heterostructure in a self-regulating manner where the excess carrier concentration is very low. This process enables relatively unimpeded glide of TDs leading to smooth glide motion.

Temperature Dependence

We probe the energetics of the REDG process in TDs by measuring glide velocities at temperatures from -20 °C to 60 °C, typical for device operation. Figure 3.3(b) is a plot of the

REDG velocity as a function of inverse temperature for the three-glissile types of dislocations. We do see an increase in TD glide velocity with increasing temperature for the fast TDs. The operation of REDG is approximately 50–100% faster at 60 °C compared to room temperature. The CL contrast of the TDs does not change in this temperature range suggesting no change in the non-radiative recombination mechanism. Assuming that the TD velocity v follows a simple Arrhenius form $v \propto e^{(-E_a/kT)}$ [61], we measure very small activation energies E_a of 0.16 eV and 0.08 eV for the glide of fast TDs along [110] and $[\bar{1}10]$ respectively. The velocity of the slow TDs along $[\bar{1}10]$ did not exhibit a well-behaved temperature dependence in the limited temperature range, so we could not obtain an activation energy. It is presently unclear why this happens. Finally, we note that we are altering the strain state slightly by varying the temperature since the strain in these films is due to a thermal expansion mismatch. This counteracts the changes in velocity from temperature alone. Correcting for this effect using a stress-velocity relation for α-dislocations from Maeda et al. [62], only slightly larger activation energies of 0.17 eV and 0.10 eV are found.

We also note that due to the offcut substrate, the resolved shear stress varies among the set of active slip planes. While this contributes to the spread of measured velocities in both directions, it cannot entirely explain the spread of measured velocities evident in Figure 3.3 as the difference is only about 17% between the maximum and minimum resolved shear stresses.

Beam Current Dependence

Figure 3.3(c) shows the dependence of REDG on the carrier injection level. Here too, we note that the CL contrast of TDs remains similar for all levels of injection. The TD glide velocity is linearly dependent on the current for all types of TDs. Maeda et al. see similar linear behavior in dislocations in bulk GaAs, which they say arises due to a diffusive carrier flux to

the dislocation that is proportional to the excess generated electron-hole pairs [62]. This linear beam current dependence of REDG velocity also provides insight into the microscopic mechanism of enhanced TD glide. In the diffusive kink model of dislocation glide, the activated processes of kink-pair formation and kink migration control the glide velocity. Maeda et al. have shown that a linear dependence of REDG velocity on current injection implies that non-radiative recombination enhances kink pair formation at the very least [44]. It is much more challenging to verify if non-radiative recombination also enhances kink migration as this depends on the whether the TD glides in a kink-collision or kink-collisionless regime. This can be the subject of future work where samples of different TD segment lengths are probed.

Comparison with Prior Measurements of REDG in Bulk GaAs Crystals

The differences in mobilities and CL contrast between TDs that we have seen are very likely due to differences in structures and core-chemistries of the dislocation, analogous to reports in bulk crystals [63]. Yet, due to complexities in the nature of TDs, a definitive assignment of TD type cannot be made by comparing to REDG behavior in bulk crystals. Briefly, dislocations in the glissile-set in bulk GaAs with $\langle 110 \rangle$ line directions are categorized as α-type (As-core), β-type (Ga-core), and screw-type. Each dislocation type has a different REDG velocity and activation energy that also depends on doping [63]. Simply extrapolating bulk crystal REDG measurements of isolated dislocations to room temperature, α-type dislocations should have REDG velocities five orders of magnitude higher than β-type dislocations and three orders of magnitude higher than screw dislocations. We do not see such a drastic difference in velocities among TDs in this study. Among the moving dislocations, there is a maximum anisotropy of 1–1.5 orders of magnitude between fast and slow TDs along $[\bar{1}10]$ at room temperature. Additionally, fast TDs in the two orthogonal directions have

different activation energies that are both lower than that reported in bulk GaAs crystals. Understanding this difference requires looking closer at the nature of TDs.

In heteroepitaxial lattice-mismatched films, MDs are easier to describe but TDs are more complicated. Specifically, for a given in-plane ⟨110⟩ direction and a given sense of strain relief, the core type of the glissile 60° MD is well defined. For instance, tensile strain in GaAs is relieved by 60°(α) MDs along [110] and 60°(β) MDs along [$\bar{1}$10]. In contrast, the core structure of a TD does not have such a unique configuration for a given sense of strain. The most discussed structure of the two TDs attached to a MD in a half-loop is one where the TDs lie along out-of-plane ⟨011⟩ directions with obtuse angles to the corresponding MDs. This implies that the one TD has the same core type (60° α or β type) as the MD and that the other has a screw configuration. If we consider only such TDs, the measured [$\bar{1}$10] TDs are identified as 60 β and screw dislocations (it is not possible to uniquely assign the TD type with the fast/slow type), the fast [110] TDs as 60° α dislocations (no screw dislocations can be explained by cross slip) and the immobile dislocations as sessile dislocations. However, this assignment is not a unique solution since other orientations are possible. Although discussed infrequently in literature, arguments have been made for the necessity of a reverse 60° TD configuration, i.e. a TD that makes an acute angle with a MD [64], [65]. In such a case, the core type of the TD has the opposite polarity as the MD, hence reversing the assignment of the 60° TD core. This possibility prevents an assignment of TDs solely based on their direction of motion.

Additional differences arise due to the line direction of TDs. To minimize line tension during film growth, TDs may not be of pure screw or 60° type as described above but instead have an average line direction such as ⟨112⟩ and ⟨123⟩ [66]. Such directions would have some kinks or jogs with different REDG velocities than pure ⟨110⟩ type segments. TEM images of

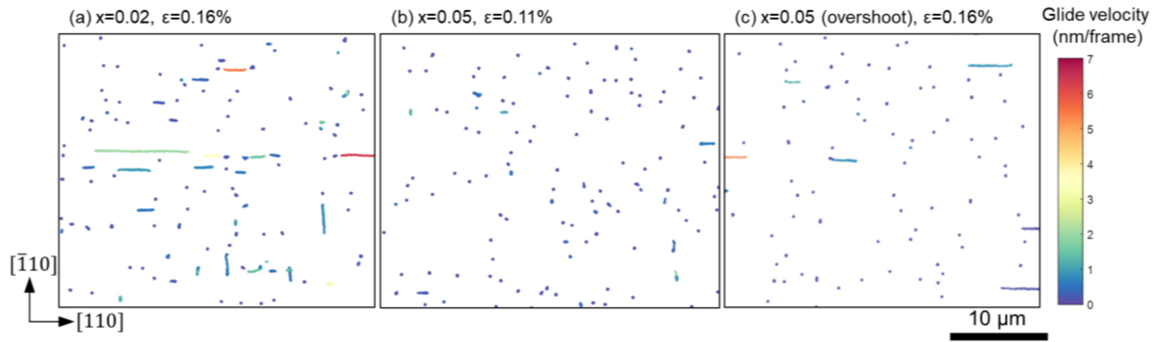

Figure 3.4. Tracks of threading dislocations undergoing recombination-enhanced glide colored by their velocity (also in supplementary videos). The samples (and number of frames) are x≈0.02 (2100), x=0.05 (1600), and x=0.05 (2100) with the overshoot layer. The residual strain is also listed. A sample absorbed current of ≈3 nA is used. The dislocation glide velocity clearly reduces upon the addition of indium and a majority of dislocations is stationary. After [83].

non-straight TD segments are common. Lastly, impurities at the dislocation core are expected to be different for grown-in dislocations in the epitaxial films as compared to those created by mechanical deformation. Such differences in the core can change the non-radiative recombination properties at defects associated with the dislocation and hence have a significant impact on REDG velocity and its activation energy.

Due to the several possible configurations of TDs described above, we cannot determine the core type of the TDs with REDG data alone; further study of REDG in heteroepitaxial systems using advanced transmission electron microscopy is required [67], [68].

IV. Metamorphic Indium-Alloyed Heterostructures

We now consider the effect of alloying 2% and 5% indium in the entire heterostructure to probe its effect on REDG. Here, we introduce indium via metamorphic structures ensuring that the films remain in a state of tension at room temperature. This would not have been the case in more conventional compressively strained (pseudomorphic) InGaAs quantum wells as the addition of more indium reduces/negates CTE-mismatch induced tension. As a reminder, the residual tensile strains in our samples are ε=0.16% for x=0.02 and slightly lower at ε=0.11%

for x=0.05. As strain influences glide velocity, we also study a sample x=0.05 (overshoot) where the strain is increased back up to ε=0.16%.

We find that the addition of indium in the heterostructure dramatically reduces the REDG velocities of all TDs, seen in Figure 3.4 (also in supplementary videos). At the same time, the CL contrast at TDs is unaffected. In the x=0.02 indium alloy (Figure 3.4(a)), only a quarter of the TDs can be characterized as moving, with about three times more TDs gliding along the [110] compared to the [$\bar{1}$10]. Looking at the maximum TD velocities, the presence of 2% indium reduces the REDG along [110] by a factor of 20–30 compared to the indium-free heterostructure. The total length of TD glide reduces by more than two orders of magnitude. This is significant for device reliability, as REDG-formed MD segments not only act as immediate non-radiative sites but also as sites for REDC. It is notable that the glide of the TDs remains smooth and continuous as in the indium-free sample.

Increasing the indium content to x=0.05 practically stops all TD motion as seen in Figure 3.4(b). As part of this reduction is due to the lower residual strain, we also compare to the x=0.05 indium sample with the overshoot layer. In this sample (Figure 3.4(c)), less than a tenth of all TDs glide and all of them do so along the [110] with lower velocities than that of the x=0.02 sample. The total MD length is further reduced to only half that of the x=0.02 sample. In summary, we have shown that alloying indium via metamorphic heterostructures significantly reduces REDG by lowering both the fraction of mobile dislocations and their velocities. We have shown this while controlling for the CTE-induced residual tensile strain.

Let us now consider different mechanisms that can explain the decrease in REDG velocity. We can straightaway rule out decreased carrier recombination at the TD based on the CL contrast, which is quite similar to the indium-free samples. Slowing due to pinning of TDs at

the MD network between GaAs and InAlGaAs is also unlikely as the film is thick [69]. Any pinning strain at that interface would decay rapidly only slightly higher from the interface, leaving sufficient driving force for TD glide. Prior results on atom probe tomography (APT) at single dislocations in InGaAs layers grown similarly [70] do not provide clear evidence of local substitutional segregation at the core as suggested by Kirkby [71]. Other groups have proposed another form of core segregation where interstitial indium migrates to shuffle sites only on the α-type partial cores, leading to preferential slowing of α-type or screw dislocations [72], [73]. While such segregation would be undetectable by APT, it seems unlikely that non-radiative recombination could dynamically move interstitial indium atoms as the dislocation glides. Even if this were possible, this would indicate that TDs should glide progressively slower the farther they travel as they accumulate In in their cores [72], a trend we do not see. This leaves solute hardening first proposed by Ehrenlich and Hirth [74] as the likely mechanism. Here the hardening agent is actually the $InAs_4$ tetrahedron, which is 21% larger in volume than the $GaAs_4$ tetrahedron[75], and the strain field around such fixed centers could slow down the migration of kinks along the dislocation. Higher indium concentrations would result in a greater number of such obstacles and hence a lower glide velocity. What remains unexplained is the asymmetry in reduction of REDG along [110] and $[\bar{1}10]$. This could arise due to asymmetric relaxation of the metamorphic buffer, not characterized in this study. Additionally, it is not known if such an asymmetric reduction in velocity could arise due to core chemistry and line directions impacting solute hardening [72].

In summary, we have shown that metamorphic structures containing indium significantly reduce REDG most likely by solute hardening. Importantly, such a hardening mechanism is not limited to REDG. It could also reduce thermal glide during strain relief at higher

temperatures involved in growth, subsequent cool down, and during device processing. This opens the possibility of employing lattice hardening to alleviate misfit line defects seen in recent work on III-V lasers on Si [76].

V. Prospects for dislocation filtering

The existence of REDG in III-V materials on Si presents the intriguing prospect of recombination-enhanced filtering of TDs using excitation sources such as light, electron beams, or even current injection. Naturally, such a technique would be most useful in patterned mesa regions where the TD can exit at the free edges. To quantify the efficacy of such a filter in the x=0 indium-free sample, we present results from an automated count of the TDs in the e-beam exposed region as a function of time in Figure 3.5. The starting TD density is approximately 1×10^{7} cm^{-2}. Here, the TDs simply glide out of the imaged area until the carrier recombination stops. We observe an initial rapid increase in the TD density of around 20% followed by a decline. The ungrouping of closely spaced TDs that could not be individually distinguished is responsible for the initial rise. As an

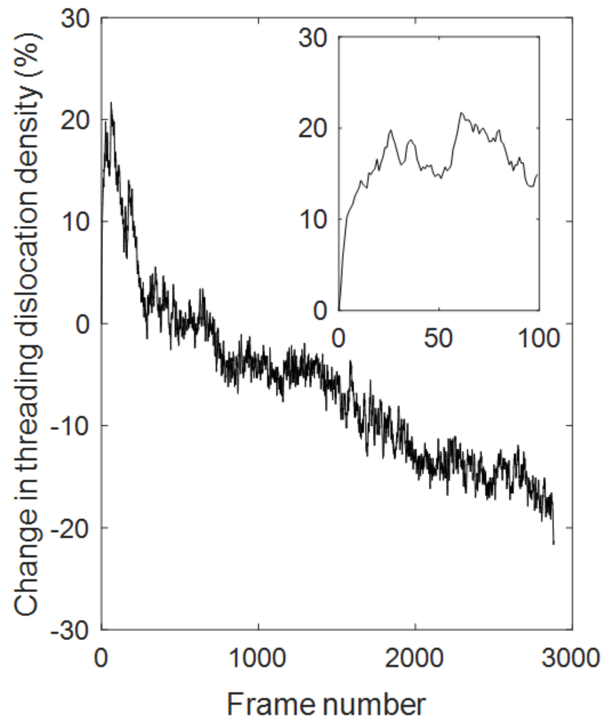

Figure 3.5. The efficacy of a recombination-enhanced glide-based dislocation filter. The change in the threading dislocation density in a 1000 μm^2 area is shown as a function of frames (time) for a sample absorbed current of ≈3nA. The starting dislocation density is $\approx1\times10^{7}$ cm^{-2}. The inset shows the apparent increase in the dislocation density in the first 100 frames due to de-clustering of TDs. After [83].

aside, this shows that static CL images could lead to an undercount of the dislocation density in critical applications due to TD clusters. Once, the TDs are sufficiently separated, a total decline from the highest TD count of about 30% is measured after 40 minutes of scanning e-beam exposure involving two stages of reduction. A sharp decline in count occurs for the first 300 frames corresponding to the fast TDs gliding out of the imaging area (an average glide velocity of 100 nm/frame). A slower second stage of TD decline follows, corresponding to slower TDs gliding out of the area. At the end of the measurement, the sample is yet to reach steady state, with some glissile TDs still moving in the frame.

Since REDG only impacts glissile dislocations, the efficacy of such a filter depends primarily on the fraction of TDs that are glissile. Ward et al. estimate a steady state fraction of glissile dislocations to be 50% for FCC-type semiconductors like GaAs, based on continued interactions between populations of glissile and sessile dislocations during heteroepitaxy [77]. Knall et. al reported the fraction of glissile dislocations as two thirds for InGaAs films on thermal cyclically annealed GaAs/Si templates [78]. Thus, a REDG-based filter could remove up to 66% of TDs—significant for metamorphic minority carrier devices as conventional efforts to reduce dislocation densities approach practical limits. However, our results show that a complete removal of glissile dislocations might not be possible. We see that some slow TDs are attracted to TD super structures resembling sub-grain boundaries previously noted in bulk GaAs wafers [79]. We also see the sporadic appearance of new TDs and TD-pairs throughout the excitation process either from existing TDs (which do not appear to be initially clustered) or appear into existence from CL-invisible sources deeper in the metamorphic buffer. Such sources and reaction events respectively increase and decrease dislocation density by a small amount (<5%) and will be discussed in a subsequent study. In summary, REDG-based filtering

is very capable of removing the fastest glissile TDs that are arguably the more damaging to optoelectronic devices. We advise the use of such filtering only after reaction-based filtering reaches a limit as the treated area is rendered largely devoid of glissile dislocations, which are necessary for further annihilation/fusion events [77]. Further work on this technique should focus on TD pinning and TD sources, interactions that also likely limit conventional growth-based defect filters.

VI. Conclusions

This chapter has examined an AlGaAs-based double heterostructure epitaxially grown on silicon as a model system to study REDG at the level of individual TDs. The motion of dark spots in the cathodoluminescence signal shows that the unique structure of TDs in films on silicon leads to REDG behavior that is distinct from that in bulk crystals. We show that REDG itself removes glissile TDs from an area quite effectively and has potential as a dislocation-filtering tool. Better statistics on dislocation populations is now more important than ever to make continued improvements in defect density and reliability. Perhaps most importantly, we show how the addition of a few percent of indium reduces REDG by two orders of magnitude at room temperature, and effectively freezes the motion of most dislocations, most plausibly by a solute or alloy hardening effect. The implications of this finding with be exploring in the following two chapters.

4. Enhanced Dislocation Filtering using Indium-Alloyed Trapping Layers

I. Introduction

After exploring the remarkable efficacy with which even dilute indium alloying slows and pins otherwise glissile dislocations, we now apply those findings to address a long-standing issue with GaAs-based lasers, specifically those whose active regions contain indium. For several years, we have been observing a disturbingly high density of misfit dislocations (MDs) in the active region of InAs QD lasers on silicon. These are a key performance-limiting defect, and strangely, they are found both along the upper and lower boundaries of the active region, even in record lifetime QD lasers [29], [76]. These ⟨110⟩-oriented MDs, like TDs, limit performance and reliability because they too are potent non-radiative recombination centers [28], but the MDs are far more damaging since they have a much larger interaction area with the active region. MDs normally form during growth in layers exceeding the critical thickness for dislocation glide [80]; to prevent this, the active layers in both QW and QD lasers are carefully designed to be below critical thickness [81]. Previous researchers, too, have noticed similar MDs in GaAs-based devices on silicon with sub-critical thickness active region, for example, Groenert et al. see MDs in QW-based devices grown on silicon via metalorganic chemical vapor deposition (MOCVD) [40], [82] and Hasegawa et al. report ⟨110⟩-oriented dark line defects in electroluminescence measurements on unaged QW layers on silicon [46]. It is truly surprising that there are not more reports of such MDs in such QD and QW lasers, but we tentatively attribute this to the practical difficulties of observing them, as QD strain contrast masks MD strain contrast in conventional cross-sectional transmission electron

microscopy (XTEM) [76]. Thus, MDs have seemingly gone unaddressed for decades in these systems.

In this chapter, we propose a formation mechanism for these MDs centered on thermal expansion mismatch rather than lattice mismatch and validate it a simplified model structure. We then demonstrate a MD filter that consists of thin alloy hardened layers, termed "trapping layers," placed directly above and below the laser active region in the epitaxial stack. These layers displace MDs away from the QDs, rather than removing them entirely, an atypical filtering strategy but one that performance yields improvements comparable to an order of magnitude reduction in TDD.

II. Proof of Concept with a Model Structure

We first examine model structures using scanning electron microscopy (SEM)-based cathodoluminescence (CL) spectroscopy to directly observe the effects of MDs on QD emission. The trapping-layer-free "baseline" structure (described in Ref. [28]) consists of a GaAs film with a single InAs QD layer 100 nm below the surface of a GaAs-on-Si template. CL images were collected at room temperature on an Attolight Rosa at 10 kV. The CL map of the wetting-layer emission at 1005 nm (Figure 4.1a) shows a network of ⟨110⟩-oriented dark lines and spots, corresponding to MDs and TDs, respectively. The sharp dark lines indicate that MDs lie sufficiently close to the QD layer to substantially lower light emission in their vicinity. The InAs QD ground-state luminescence map collected at 1245 nm (Figure 4.1b) has these same dark features, although they appear more diffuse.

The single QD layer is below critical thickness, so we hypothesize the MDs in this system form not during growth but during cooldown. Since GaAs has a larger thermal expansion coefficient than silicon ($\alpha_{GaAs} - \alpha_{Si} \approx 3\times10^{-6}\ K^{-1}$), GaAs layers, which are

essentially unstrained by the end of growth at 540 °C, become up to 0.1% biaxially tensile strained during cooldown as they approach 300 °C. Due to this thermal strain, the still-mobile TD segments can glide in the GaAs layers thicker than just a few hundred nanometers. This is not surprising: we know thermal stress can drive dislocation glide—thermal cyclic annealing (TCA) takes advantage of this very principle to reduce TDDs [16]. Even so, TDs gliding during cooldown is not inherently problematic. If, however, the indium-containing QD layer inhibits lateral TD motion [83], as shown in Figure 4.1c, then as the free TD segment in the thick GaAs layer glides away, the TD segment in the QD is left behind, and a MD forms at the QD layer interface. We hypothesize that this mechanical hardening arises from uneven stress fields generated by the strained QDs [32] and alloy fluctuations in the $In_{0.15}Ga_{0.85}As$ QW.

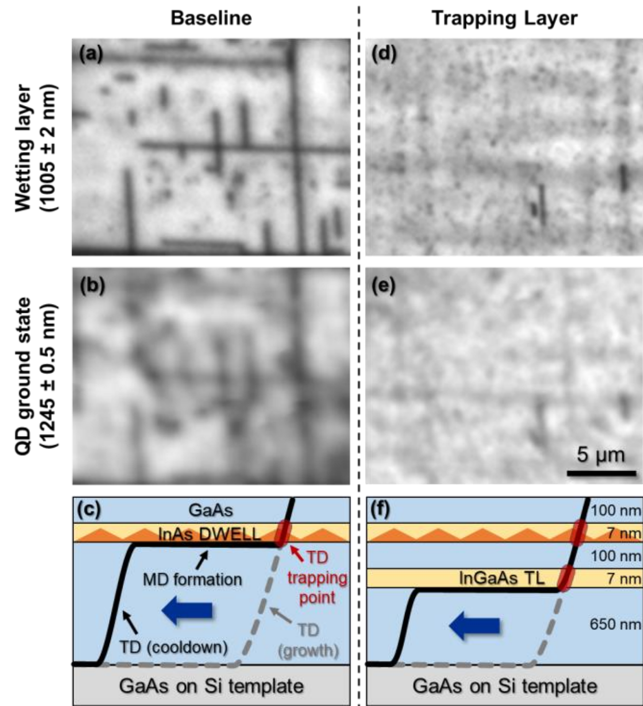

Figure 4.1 (a-b) Monochromatic cathodo-luminescence (CL) images of the baseline structure at **(a)** QD wetting-layer emission wavelength (1005 nm) and **(b)** QD ground-state emission wavelength (1245 nm). **(c)** Schematic representation of approximate dislocation evolution in baseline structure. During cooldown, enough tensile stress builds in the thick GaAs layer below the QD layer for the threading dislocation (TD) to glide from its growth position (gray dotted line). The QD layer traps the TD (red box), causing a misfit dislocation (MD) to form at the bottom interface. The 100-nm GaAs cap is too thin to relax, so no MD forms here. **(d-e)** Comparable CL of the trapping layer structure from **(d)** the wetting layer **(e)** and the QD ground state. Total dark line length in the QD layer is 20× lower than in the baseline. **(f)** While the TD in the thick GaAs layer still glides in response to the tensile stress, by introducing an additional TD trapping point, the trapping layer displaces MD formation away from the QD layer. After [94].

The latter effect, similar to the alloy hardening phenomena reported on previously in bulk semiconductors [84], [85], occurs because the difference in covalent radii of indium (142 pm) and gallium (124 pm) generates in-layer stress fluctuations [75]. Finally, note that no TD glide (and thus no MD formation) occurs above the QDs because the GaAs capping layer is too thin to relax.

If our proposed mechanism is correct, we should be able to leverage this hardening effect to displace the MDs from the QD layer. By inserting a 7-nm $In_{0.15}Ga_{0.85}As$ "trapping layer" 100 nm below the QDs, we can reduce the MD length at the QD layer by 20× (Figure 4.1d-e). The trapping layer itself should have a negligible impact on the TDD because it is below critical thickness, and indeed, the measured TDD is comparable to that of the baseline structure. Instead, introducing an additional TD trapping point (red box) (Figure 4.1f) forces TD glide and the resulting MD formation to occur below the trapping layer, rather than at the QDs. This agrees with the observed faint, broad dark lines that we attribute to MDs below the trapping layer. Assuming the distance between the hardened layers is sufficiently small (i.e. the intermediate GaAs is below the critical thickness induced by the thermal contraction), no MDs can form between the trapping layer and the QD layer. And, just as with the QD layer, MDs cannot pass through the trapping layer due to the tensile-to-compressive strain reversal at this interface.

To gain more detailed insight into the structural evolution of MDs and TDs, we use a diffraction-based SEM technique, electron-channeling contrast imaging (ECCI), to directly observe a continuation of the MD formation process that occurs during cooldown at room temperature (Figure 4.2). Prior work has demonstrated that electron beams generate electron-hole pairs that recombine at dislocations and can drive dislocation glide in heteroepitaxial thin

film semiconductors with sufficient residual stress [57], [86], as is the case in our system, as well as in bulk semiconductors with an externally applied stress [62], [63]. Although glide processes cease below ~300 °C, the thermally induced tensile stress continues to build, so the GaAs layers experience a 0.15% biaxial tensile strain at room temperature. Figure 4.2a—collected on a Thermo Fisher Apreo S SEM at 30 kV in the (400)/(220) channeling condition—shows a time-lapse evolution of a single TD in the baseline model structure. Initially, only a spot of point contrast is visible where the TD segment exits the film surface. Electron-beam irradiation supplies energy that reanimates TD glide, so the free TD segment below the mechanically hardened QD-layer glides away, forming a MD that lengthens over time (orange arrows). We see no point contrast on the growing end indicating that this end sinks down into the film beyond the detection range of ECCI, just as depicted in Figure 4.1c. If, instead, MDs formed due to the QD layer exceeding critical thickness, we would expect to see the upper TD segment gliding, but here it is stationary. This provides direct evidence that our proposed mechanism—based on thermal strain buildup during cooldown and local TD trapping—drives MD formation.

Figure 4.2b-e—collected on a FEI Quanta SEM under the same conditions as Figure 4.2a—compare MD densities between the baseline and the trapping layer structure before and after heavy electron-beam irradiation. The as-grown baseline structure (Figure 4.2b) contains MDs, marked with black arrows, following growth and cooldown. Based on the limited 100-200 nm depth sensitivity of ECCI, these sharp-contrast MDs must be reasonably near the film surface, most likely just below the shallow QD layer, as in Figure 4.1a-c., Electron-beam irradiation causes new sharp-contrast MD segments, marked with orange arrows, to form and grow (Figure 4.2c). In the as-grown trapping-layer structure

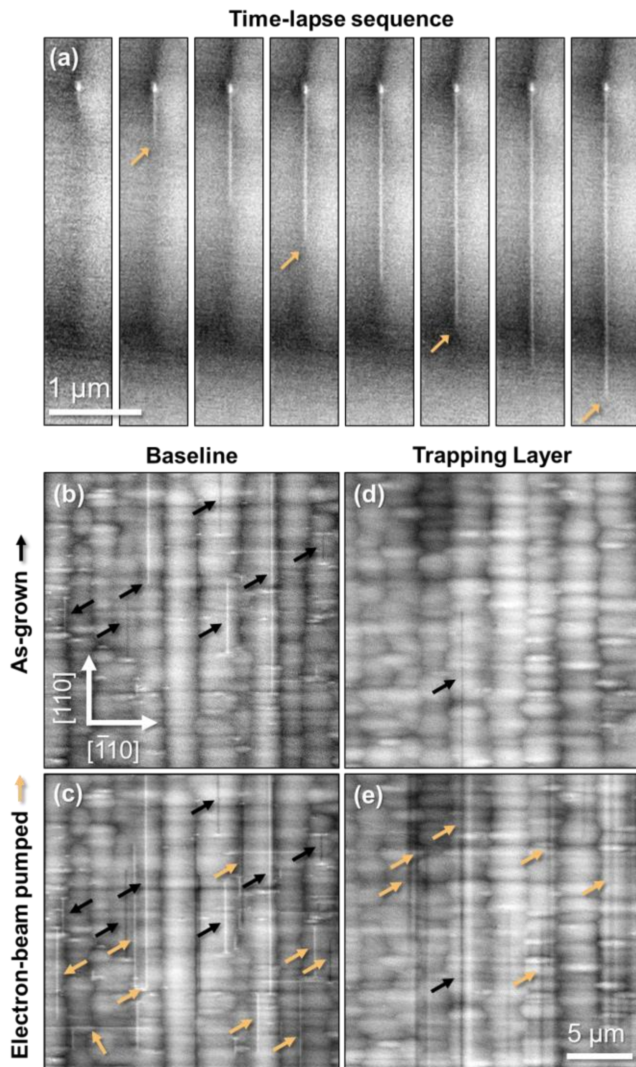

Figure 4.2 (a-e) Electron-channeling contrast imaging (ECCI) of the baseline and trapping layer model structures. **(a)** ECCI time-lapse sequence (~550 s image interval) showing growth of a misfit dislocation (MD) (orange arrows) from a stationary, trapped threading dislocation (TD) segment in the baseline structure. **(b-c)** Corresponding ECCI of the baseline structure **(b)** before and **(c)** after electron-beam illumination. Black arrows indicate as-grown MD positions; orange arrows indicate MD growth from electron-beam pumping. **(d-e)** ECCI of the trapping layer structure **(d)** before and **(e)** after electron-beam illumination. Compared to the sharp line contrast of MDs in (b-c), the diffuse line contrast in (e) is due to MDs lying deeper in the structure, i.e. at the trapping layer. After [94].

(Figure 4.2d), we measure a 20× reduction in total shallow (high-sharpness) MD length from baseline (over a 2500-μm^2 area), in agreement with CL. Electron-beam irradiation generates a high-density network of diffuse-contrast MD lines (Figure 4.2e). Their diffuse contrast indicates that these dislocations are located deeper in the structure, likely at the trapping layer [87]. Notably, the density of high-sharpness, shallow dislocations remains constant, indicating that SEM irradiation does not increase MD length near the QD layer. As recombination-enhanced dislocation motion (REDM) processes are common failure mechanisms in semiconductor lasers, this is promising for laser reliability.

III. Dislocation Filtering in Full Laser Structure

To investigate the efficacy of misfit trapping layers in full lasers, we fabricated InAs QD ridge structures on (001) Si with trapping layers in the epitaxial stack, shown schematically in Figure 4.3a, alongside a baseline sample with no trapping layers, both grown from the same 3×10^7 cm^{-2} TDD buffer (see references for buffer [17] and full laser [88] growth details). All lasers were fabricated together into 3-μm wide, 1500-μm long, cleaved-facet, deeply etched ridge structures. Unlike with the model structures, the GaAs/AlGaAs layers above the active region here are sufficiently thick to relax during cooldown, enabling MD formation at both the uppermost and lowermost QDs, as seen in Ref. [76]. To trap defects from both sides, we insert two sub-critical thickness 7-nm trapping layers 80 nm above and below the active region, composed of $In_{0.15}Ga_{0.85}As$ and $In_{0.15}Al_{0.85}As$, respectively. These dissimilar alloys minimize electrical barriers due to band misalignment, but we expect them to have near-identical trapping ability. Since the covalent single-bond radii of aluminum (126 pm) and gallium (124 pm) are nearly identical, an equivalent indium alloying fraction should harden both layers similarly; note that these similar covalent radii also explain why the AlGaAs layers do not

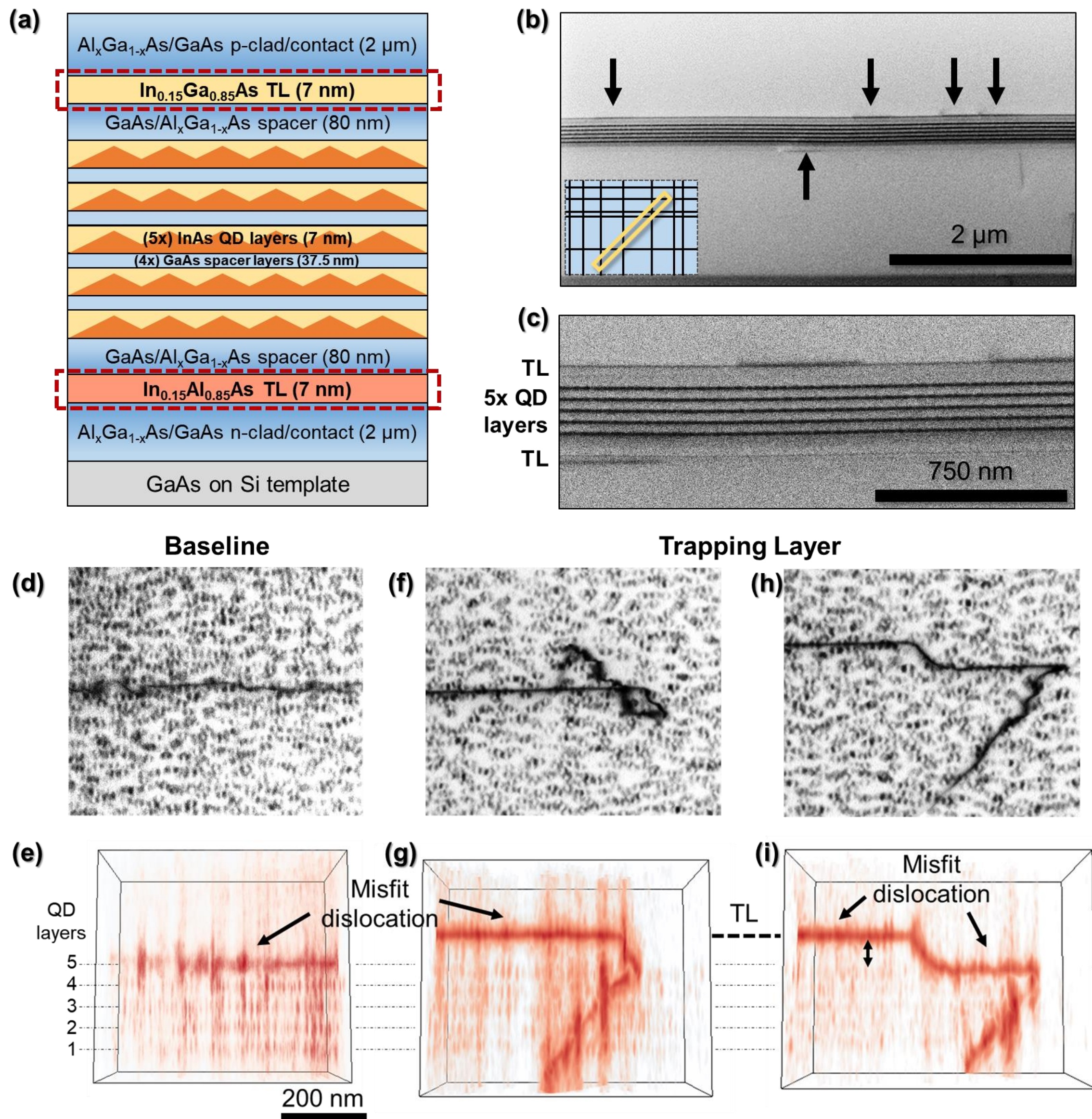

Figure 4.3 (a) Schematic of a quantum dot (QD) laser with trapping layers (TLs) (red boxes) above and below the QD layers. Baseline samples are equivalent but lack trapping layers. **(b)** Cross-sectional bright-field (BF) STEM ([100] zone) of a trapping-layer laser. Inset shows orientation of foil relative to misfit dislocations (MDs). Arrows mark MD segments at the trapping layers. **(c)** High-magnification image of (b). **(d-e)** Baseline laser: **(d)** BF plan-view (PV)-STEM image (**g = 220**) showing a MD among QDs. **(e)** Cross-sectional tomographic reconstruction showing the MD at the fifth QD layer. **(f-i)** Trapping layer laser: **(f)** BF PV-STEM showing a MD terminating in a threading dislocation (TD). **(g)** Reconstruction shows the MD lying at the trapping layer. **(h)** MDs at two heights with a TD end. **(i)** Reconstruction reveals a short MD at the top QD layer with the rest lying at the trapping layer. After [94].

inhibit TD glide. Figure 4.3b-c show the effect of trapping layers on MD formation via bright-field (BF) on-zone ([100]) cross-sectional STEM. All STEM images were acquired using a

Thermo Fisher Talos 200X G2 TEM/STEM (200 kV) with a standard BF STEM circular detector and beam convergence angle of 10.5 mrad. The sample lift-out geometry, oriented at 45° to the orthogonal MD arrays (Figure 4.3b inset), ensures that all MDs appear as equal-length horizontal lines. As shown in both low (Figure 4.3b) and high (Figure 4.3c) magnification images, MDs (black arrows) are displaced from the active region to the upper and lower trapping layers.

Figure 4.4 shows a cross sectional view of misfit trapping including the attached threading dislocation. Two images where a threading dislocation (marked with black arrow) passes through the QD layers and gives rise to a misfit segment at the top trapping layer (analogous to Figure 4.3f-i). Due to the tilt, these two misfit segments appear to lie at different heights, but they both lie at the trapping layer. From this, we can infer that the misfit segments lie at different depths from the face of the foil. In both images, we can additionally see MDs lying in the direction of the foil thickness (marked with white arrows). From the length of these

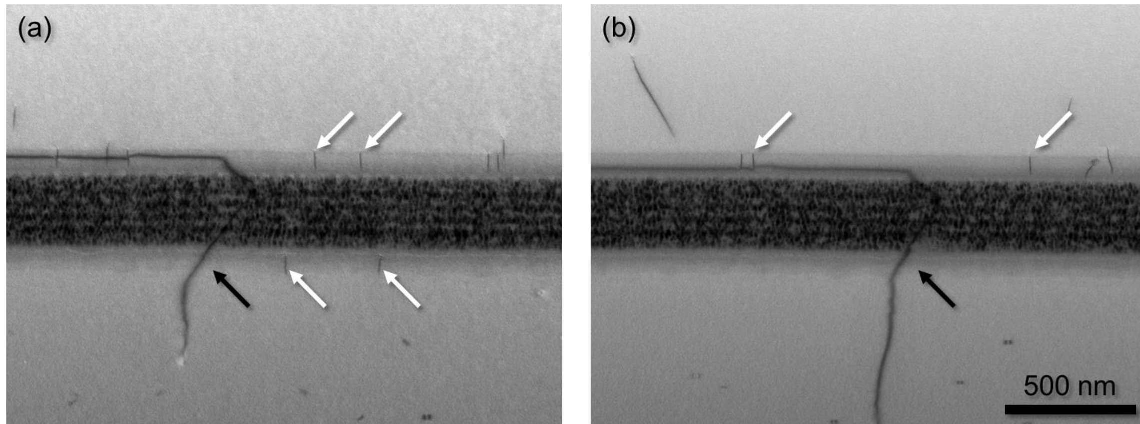

Figure 4.4 Both (a) and (b) show cross sectional scanning transmission electron micrographs of both misfit and threading dislocations in a trapping layer laser. Samples were lifted out along a [110] direction and imaged at a tilt (**g** = **002**) resulting in certain misfits running parallel to the length of the foil and others running perpendicular to it (marked with white arrows). Due to the tilt, the perpendicular misfits appear as vertical lines and the spacer layers between the quantum dots (QDs) disappear among the QD strain contrast. Critically, the misfit dislocations are clearly at different heights than the QDs. Threading dislocations, marked with black arrows, give rise to the misfit dislocations, as described.

misfits and tilt angles, we can determine the foil thickness. It is worth noting, in both images, that QDs adjacent to the TD appear slightly different from the others both in density and in appearance. This suggests that the TD has not moved from its growth position in the QD layers. The consistency between these images and Figure 4.3b and Figure 4.3f-i provides strong evidence for the success of both the upper and lower trapping layer.

We illustrate the differences between the trapping layer and baseline structures using strain-contrast electron tomography generated from BF plan-view (PV)-STEM images taken across ~60° tilt range. Tomography is traditionally performed by tilting along a single axis, but here we followed the **g** = **220** Kikuchi band using a double-tilt holder to maximize strain contrast and used the BF detector as a virtual aperture. A sample PV-STEM image for the baseline (Figure 4.3d) shows a MD amid a field of QDs. The tomographic reconstruction (Figure 4.3e), created with Tomviz (https://tomviz.org), resolves the five QD layers and shows that this MD lies at the uppermost QD layer. In a trapping layer laser, Figure 4.3f-g show a PV-STEM image and a tomographic reconstruction, respectively, of a MD and a terminating TD segment. Although strain-contrast tomography cannot resolve the trapping layer itself, the MD clearly lies away from the QD layer at the trapping layer's height. The TD forms no additional MD segments as it travels downward through the QD layers. Figure 4.3h also shows a PV-STEM image of a dislocation in a trapping layer laser, but here, there is a short, angled section along the MD, indicating a change in height. The tomographic reconstruction (Figure 4.3i) confirms that the MDs lie at the trapping layer and the uppermost QD layer. We expect that because the trapping-layer hardening effect arises from alloy fluctuations, it is locally uneven. This can allow TDs to glide briefly until they reach a region with enough trapping to prevent further motion. Unfortunately, this causes a MD to form at the outermost QD layer.

Nevertheless, trapping layers successfully displace most MD length from the QDs as confirmed with PV-STEM (not shown).

In Figure 4.5a, we analyze a simplified case of mechanical hardening where a threading dislocation is completely mobile in GaAs and trapped in both the $In_{0.15}Ga_{0.85}As$ trapping layer and the QD layer above it. To glide in GaAs, the TD segment only needs to overcome the short-range, interatomic Peierls stress, τ_p (~4 GPa in GaAs [89]). This happens readily with relatively small resolved shear stresses either at elevated temperatures or through REDM processes [56], as explored in Figure 2.

The stress states in the two indium-alloyed layers are more complex. We therefore employ the concept of an effective stress (τ_{eff}), where, by our convention, the threading segments in these indium-alloyed layers can only glide with the free segment in the GaAs if $\tau_{eff} > 0$ [61], [90], [91]. During cooldown, the sub-critical thickness $In_{0.15}Ga_{0.85}As$ and QD layers remain compressively strained. The threading segments in these layers experiences a shear stress

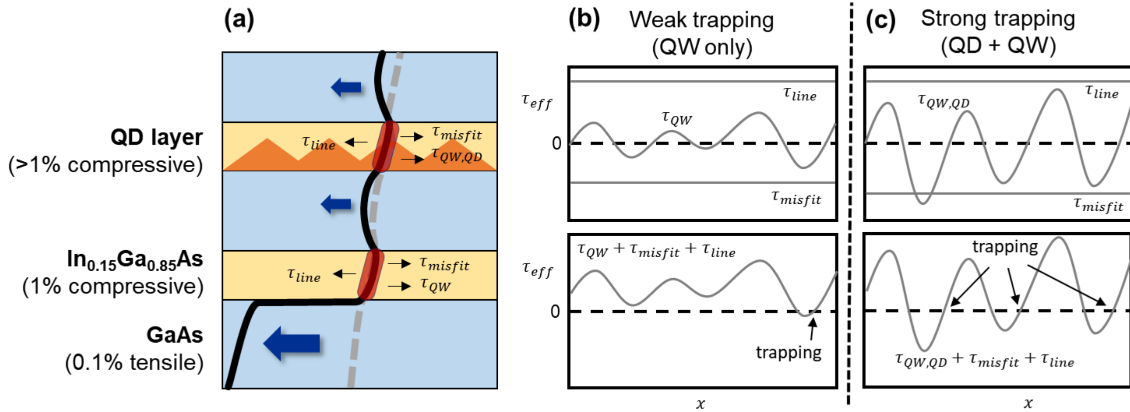

Figure 4.5. (a) Schematic showing a dislocation traveling upwards through a GaAs-based film on Si, trapped by both the trapping layer and the QD layer. τ_{line} represents the shear due to dislocation line tension; τ_{misfit}, the shear due to lattice mismatch between GaAs and the strained indium-alloyed layers; and τ_{QW}, a resistive hardening shear due to alloy compositional fluctuations. (b-c) Rough sketch of the effective stress landscape in (b) the In0.15Ga0.85As trapping layer where trapping is relatively weak and (c) the QD layer, where the combination of QDs inside a QW results in strong trapping.

(τ_{misfit}) due to this strain, but since the layers are below critical thickness, by definition $\tau_{line} > \tau_{misfit}$ where (τ_{line}) is the maximum value of dislocation's line tension. This maximum is assumed to occur when the threading segment forms a near-perpendicular kink. Without any additional resistive shear stresses, the shear from the dislocation line tension would normally drag these short threading segments along with it—no misfit segments would form [91]. Clearly, this is not the case for either the trapping layer or the QD layer.

To prevent TD glide as we observe, there must be an additional stress that adds to τ_{misfit} to at least match the magnitude of τ_{line}. The source of this additional stress in the trapping layer, (τ_{QW}), is an effect similar to alloy hardening effects observed in certain bulk semiconductor alloys [84], [85]. In both cases, natural compositional variations generate in-layer stress fluctuations. Thus, the effective stress state in the trapping layer resembles that shown in Figure 4.5b. In our case, the hardening effect results from the 21% volume difference between the $InAs_4$ and $GaAs_4$ tetrahedra [75]. Note that an alloy like AlGaAs, where the $AlAs_4$ and $GaAs_4$ tetrahedra are of near-identical size, should have no alloy hardening effect. In Figure 4.5b, if the long-range resistive stress field, τ_{QW}, is large enough such that at some point $\tau_{eff} = \tau_{line_\perp} - (\tau_{misfit} + \tau_{QW}) = 0$, then the TD segment is trapped at that point in the trapping layer, and a MD segment will form. Note that the misfit segment cannot simply glide upward through the trapping layer due to the repulsive compressive strain in that layer.

The magnitude of the stress field in the QD layer is substantially larger than in the trapping layer, as shown in Figure 4.5c. Mechanical hardening in the QW once again provides a resistive shear, but as Beanland et al. have shown, the QDs also provide their own resistive shear, trapping threading segments so effectively that they nearly triple the critical thickness as compared to a QW [32]. These effects agree with metallurgical research showing that

mechanical properties of both elemental metals and alloys become increasingly temperature independent, or athermal, with increasing temperature. This is because long-range fluctuating stress fields, generated both by compositional fluctuations and structural features such as precipitates and line defects, are no easier to surmount at high temperatures than at low ones [92], [93].

Room temperature photoluminescence spectroscopy and continuous-wave (CW) light output-current-voltage (LIV) curves of a representative high performing device from both designs are shown in Figure 4.6a-b, respectively. Introducing trapping layers increases

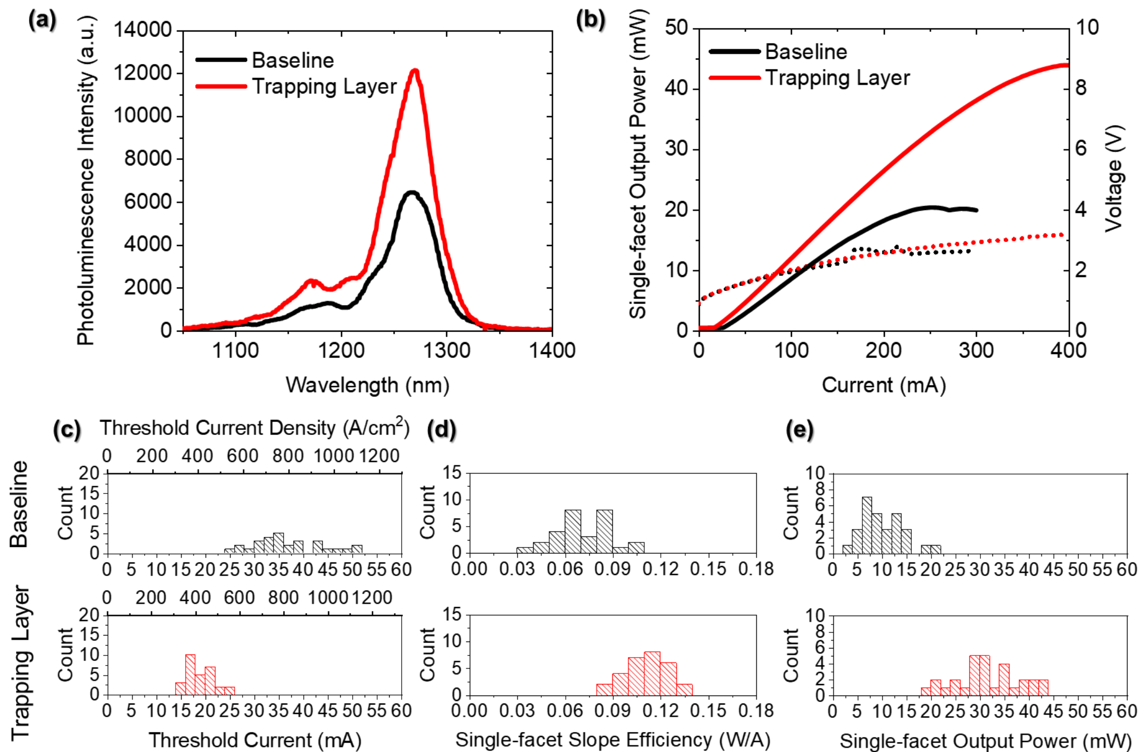

Figure 4.6. (a-e) Comparison of baseline (black) and trapping layer (red) lasers. **(a)** Photoluminescence intensity comparison of trapping layer and baseline lasers. **(b)** Single-facet output power (mW) (solid) and voltage (V) (dashed) as a function of current (mA). A lower threshold current and higher slope efficiency and peak output power are observed in the trapping layer laser compared to baseline. Current-voltage (IV) curves are comparable for both designs. **(c-e)** Histograms showing performance improvements of trapping layer devices along key performance metrics: **(c)** threshold current (mA), **(d)** slope efficiency (W/A), and **(e)** output power (mW). After [94].

photoluminescence intensity by approximately 2× compared to baseline (Figure 4.6a). This agrees with the marked improvements in threshold current, slope efficiency, and output power shown in the representative LIV curves (Figure 4.6b). Histograms comparing the structures along these same metrics (Figure 4.6c-e) further support these performance improvements. The trapping layer design shows a 2× reduction in median threshold current from baseline. The lowest measured threshold current (16 mA) represents a 40% decrease from baseline minimum. This is also 20% below identically designed state-of-the-art lasers on Si [88], even with a 4× higher TDD here. We additionally observe an impressive 60% increase in median slope efficiency and a 3.4× increase in median peak single-facet output powers for trapping layer lasers. Finally, the median electrically dissipated power at rollover for trapping layer lasers (0.85 W) is approximately twice that of baseline (0.46 W) (not shown). This indicates—assuming comparable thermal impedances—that the inclusion of trapping layers increases the lasers' optical amplification (gain). We cannot determine whether trapping layers adversely impact electrical transport in these lasers due to large variability in the series resistances across both sets of devices. But as higher-than-usual specific contact resistances across all devices (p: 2.3×10^{-5} $\Omega\cdot cm^2$, n: 5.5×10^{-5} $\Omega\cdot cm^2$) represent a limiting factor on output power, we anticipate processing modifications will further improve device performance.

The relative performance improvements reported here—achieved simply by displacing existing MDs—are comparable to previous gains achieved by reducing TDD by an order of magnitude (7×10^7 cm^{-2} to 7×10^6 cm^{-2}) [30]. As device thicknesses are critical for many applications, it is highly advantageous that these performance gains made using thin misfit trapping layers compare favorably to those achieved using hundreds of nanometers of traditional TD filters. This same single order-of-magnitude reduction in TDD also resulted in

a nearly four order-of-magnitude increase in device lifetimes [30]. In these low TDD and low strain systems, the total active-region MD line length is determined by TDD and glide kinetics, so this dramatic increase in lifetime is likely explained in part by an unseen reduction in total MD line length. All dislocation line length, whether MD or TD, within the active region degrades laser performance and lifetime; the inclusion and optimization of trapping layers thus complements important, ongoing TDD reduction efforts [18]. In future work, we will determine whether eliminating MDs enables epitaxially integrated InAs QD lasers to finally meet commercial lifetime requirements at 60 °C operating temperature.

IV. Conclusions

We have proposed a mechanism that describes how TDs give rise to highly damaging MDs that form during post-growth cooldown in certain epitaxial III-V-on-silicon structures. We mitigate this by inserting thin alloy hardened layers to locally inhibit TD glide and displace MD formation away from the QDs, removing 95% of MD length in model structures. In lasers, these "trapping layers," placed above and below the active region, represent a significant departure from traditional defect filtering: they displace, rather than remove, defects that form during cooldown, rather than during growth. In the next chapter, we will explore the remarkable implications of these trapping layers on QD laser reliability.

5. Reliability Impacts of Trapping Layers

I. Introduction

In the previous chapter, we showed that MDs in the active region of InAs QD lasers do not form conventionally by exceeding the lattice-mismatch critical thickness; instead, they form after growth during sample cooldown due to a combination of thermal expansion mismatch between (Al)GaAs and silicon and mechanical hardening effects in the QDs [94]. These hardening effects arise due to: (1) alloy hardening resulting from the different covalent radii of gallium and indium [75], [83] and (2) coherency strain hardening from the highly strained QDs [32]. Thus, MD formation through this process may be unique to (Al)GaAs-based devices grown on Si. We mitigate this issue by inserting an indium-alloyed MD trapping layer (TL) on both sides of the QD active region to extend the dislocation pinning region into doped regions of the device to shift MD formation away from the active region and substantially improves both initial performance [94] and, very recently, reliability [95].

In this chapter, we age and then analyze lasers by plan-view TEM, to link the degradation in device performance to structural changes in the dislocations. In lasers without trapping layers (no-TL), we show extensive evidence of recombination-enhanced dislocation climb (REDC), a failure mechanism in GaAs-based lasers [29], [96]–[98], consistent with the large reductions in peak power and increases in threshold current. We attribute this to MDs (positioned directly along the outermost QD layers) catalyzing significant non-radiative recombination of minority carriers. In devices with trapping layers, by contrast, most MD lie outside the depletion region and show no evidence of REDC.

II. Experimental Background

To perform this comparative lifetime analysis, we grew and fabricated three sets of ridge laser structures, using the procedure outlined in Refs. [88] (laser structure), [17] (buffer), and [94] (trapping layer). The TDD of the templates was 2–4×10^7 cm^{-2}. These are not the lowest TDD samples investigated for InAs QD lasers on silicon but serve well to investigate the significant impact of MDs over TDs. Figure 5.1a shows a simplified schematic of the general laser structure. Two of the three structures contain 7 nm thick $In_{0.15}Al_{0.85}As$ and $In_{0.15}Ga_{0.85}As$ MD trapping layers at the indicated positions in the n-cladding and p-cladding, respectively, at 80 nm (‘TL80’) and 180 nm (‘TL180’) from the nearest QD layer. The trapping layer indium composition and thickness were chosen simply to match the quantum wells encasing the QDs in the active region. $In_{0.15}Al_{0.85}As$ was used in place of $In_{0.15}Ga_{0.85}As$ on the n-side to minimize band misalignment. Trapping layer positions were chosen to yield a spacing between the QD and TLs that is below a 20 %-nm strain-thickness product [81] that serves to approximate the classical one-sided dislocation glide critical thickness limit. Without access to the precise strain and glide kinetics *in-situ*, we design for III-V/Si thermal-expansion induced tensile strains in the range of 0.1–0.2%, yielding critical TL spacings of 200 nm (met by TL180 and TL80) and 100 nm (met by TL80), respectively. We expect similar alloy hardening from $In_{0.15}Al_{0.85}As$ and $In_{0.15}Ga_{0.85}As$. The third ‘No-TL’ structure lacks MD trapping layers but is otherwise equivalent. Laser bars were coated with quarter-wave thickness SiO_2 and Ta_2O_5 layers for 60% (1 pair) and 99% (8 pairs) reflectivity on front and back facets, respectively, both to reduce threshold current and protect facets from degradation. The bars were then singulated, soldered onto AlN carriers, and wirebonded before being loaded into a Newport ILX Lightwave LRS-9434 laser diode reliability test system. We aged three No-TL,

five TL180, and six TL80 ridge lasers (3 μm × 1500 μm) under automatic current control (ACC) at 60 °C, excluding any devices with a threshold current density above 500 A cm^{-2} or a maximum output power below 10 mW at 20 °C after facet coating. The devices were aged for up to 3000 hours at approximately twice their initial 60 °C threshold current—70 mA for the No-TL devices and 37 mA for the TL devices. Light output-current (LI) and voltage-current (VI) measurements were collected automatically at 35 °C and 60 °C every 50 hours. We selected the device with the largest reduction in maximum output power from each group for PV-STEM analysis and prepared a foil containing the active region (including the trapping layers for TL80 and TL180) using standard focused ion beam lift-out processes. We also generate electron tomograms from small portions of the TL80 and TL180 foils, taking several bright-field systematic row [99] images (beam convergence angle = 10.5 mrad, BF circular detector collection angle = 26 mrad) at 5° increments in tilt along the (220) Kikuchi line to maximize dislocation contrast. We use a double tilt holder to ensure each image is acquired in the desired diffraction condition but align the sample such that the tilt axis is approximately parallel to the ⟨110⟩ direction to improve the reconstruction. We reconstruct the dataset using the software *tomviz* (https://tomviz.org), manually aligning the images and setting a tilt axis, followed by a simple back-projection reconstruction.

Figure 5.1b presents a composite cross-sectional scanning transmission electron microscopy (STEM) image from a typical TL180 laser. The left portion is imaged along the [110] zone axis of the sample; the right portion is imaged by tilting the sample about the horizontal axis to reveal in-plane misfit dislocations. The yellow arrows in the magnified outset indicate MD segments lying flat along the projected thickness of the upper trapping layer

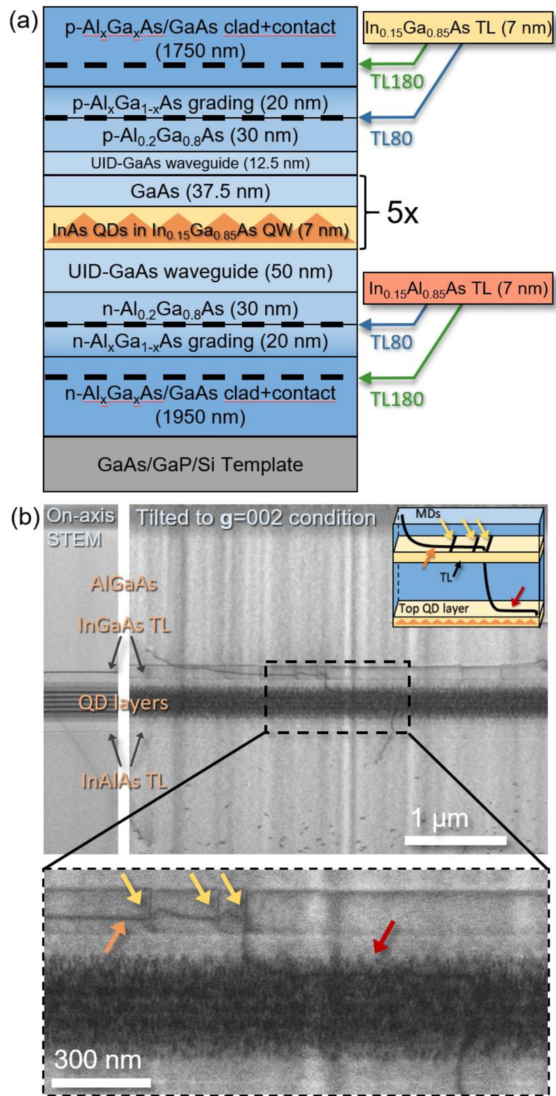

Figure 5.1. **(a)** Schematic of the No-TL laser structure indicating where trapping layers are inserted in TL80 and TL180 structures. In TL180 lasers, the trapping layer lies 100 nm further from the active region. **(b)** Cross-sectional scanning transmission electron microscopy (STEM) image of a TL180 laser structure along the [110] zone axis (left) and tilted into a **g**=002 diffraction condition (right). The outset presents a high magnification image of the dashed region. A threading dislocation rises through the QD layers and forms a short misfit dislocation (MD) segment (red arrow) at the QD layers and a trapped MD (orange arrow) segment at the upper TL. The yellow arrows mark several perpendicular MDs lying along the upper trapping layer. These appear as short vertical segments in projection, as shown schematically in the inset. After [191].

(shown schematically in Figure 5.1b inset). The dislocation running perpendicular to these lies mostly at the trapping layer (orange arrow) but a short segment lies at the uppermost QD layer (red arrow), a rare instance of partial failure of the trapping layer. While we have not yet identified the mechanism that leads to these partial failures, these two segments illustrate that the mechanical hardening effects that displace MD formation to the trapping layers also occur in the QD layers themselves. Without the trapping layers, all the MD length (100%) forms along the outermost QD layers [94], [100]. With trapping layers, our prior work suggests that only about 5% of the total MD length reaches the QD layers [94].

III. Enhanced Reliability due to Trapping Layers

Figure 5.2a-5.2c presents LI and VI measurements at 50-hour increments of aging time for a high performing device from each group. We have previously attribute the differences in the initial performance between the no-TL and TL devices to reduced non-radiative recombination losses at MD [94]. These differences continue to widen during operation as No-TL lasers degrade much faster than either TL laser, while turn-on voltage and series resistance are similar for all devices. We note that the steady decrease in rollover current over time in the LI curves and the slow degradation of the VI curves suggest an increase in the junction temperature due to increased non-radiative recombination. Both effects are noticeably less pronounced in TL80.

Figure 5.2d-5.2g summarizes degradation metrics (change in threshold current, peak power, current required for 10 mW of output power, and current at rollover, respectively) for these devices derived from the LI measurements. The No-TL device degrades rapidly, with output power falling below 10 mW after only 600 hours and threshold current increasing 55% and peak output power dropping 48% after 3000 hours. In contrast, both TL devices undergo less than 9% increases in the threshold current and current required for 10 mW of output power. TL80 performs best overall, with a peak power drop of only 11%, compared to TL180's 20% drop. To better understand whether the differences in the rollover behavior between TL180 and TL80 devices are real, we performed a Mann-Whitney U statistical test on the change in peak power at rollover for all TL lasers from each group and find a statistically significant difference ($\alpha = 0.05$) in peak power drop within the first 15 hours of operation.

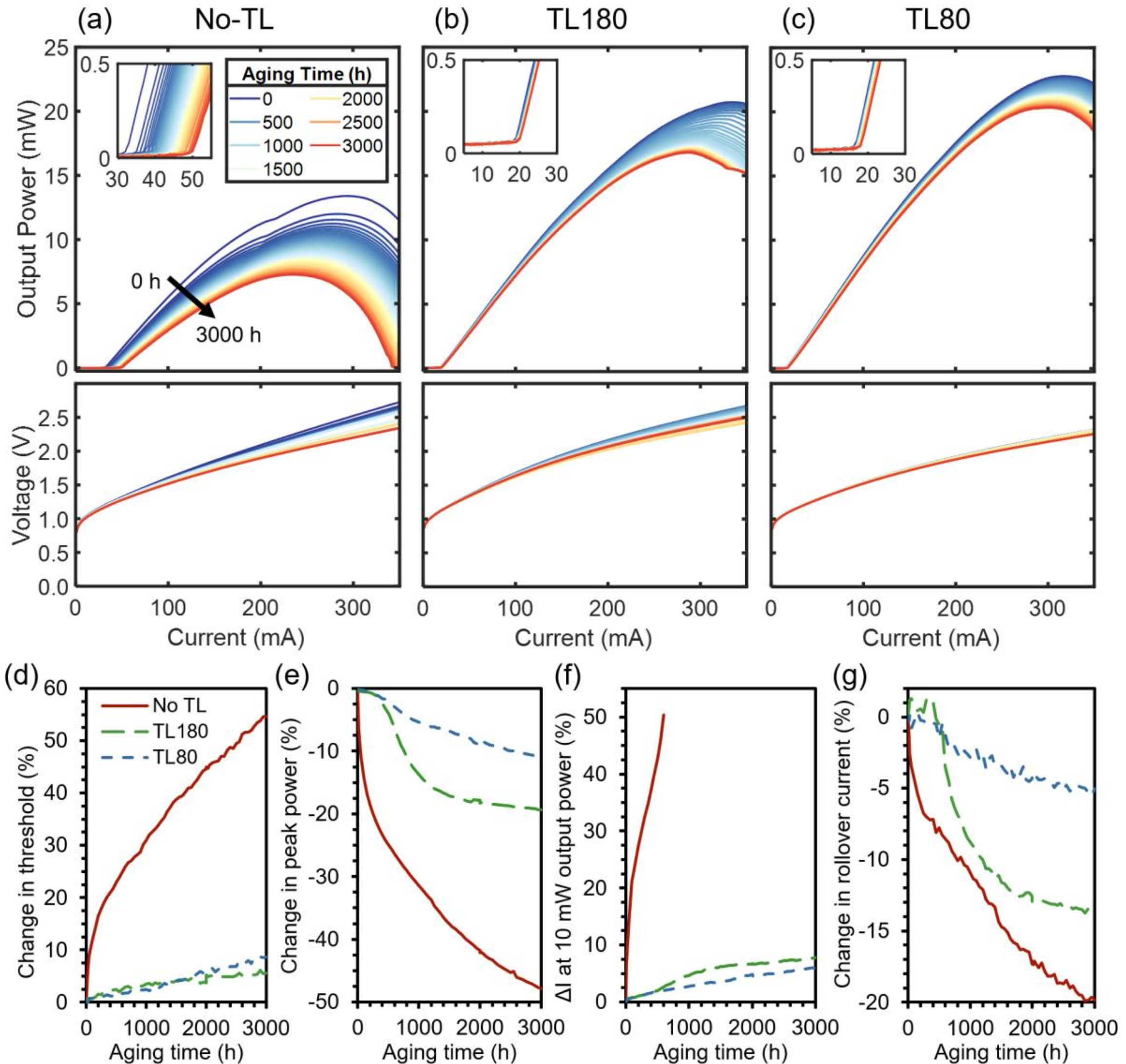

Figure 5.2. 60 °C reliability data from a high performing device of each design. **(a-c)** Light-output and voltage vs. current (LIV) measurements at 50 h intervals over the course of aging for (a) No-TL, (b) TL180, and (c) TL80. **(d-g)** Degradation behavior for the same three lasers measured by (d) change in threshold current, (e) change in peak output power, (f) change in the current required for 10 mW of output power, and (g) change in current at rollover during aging. After [191].

We also compare performance of TL lasers to recently reported QD lasers grown on GaAs aged under similar conditions [101] in Figure 5.3 and find very similar rates of 35 °C threshold current increase, while other metrics show slightly slower degradation rates for the native-substrate lasers. While different device dimensions and facet coatings make an exact comparison between these devices difficult, the qualitative similarities in their behavior are

nevertheless noteworthy. Substantially reducing the density of MDs lying within the active region results in reliability metrics that appear far more like native substrates than otherwise equivalent devices on silicon. This suggests that most degradation in the No-TL lasers results from MDs in the active region.

IV. Plan-View STEM Analysis of Degradation

We examine MD networks in aged lasers using PV-STEM to explain differences in degradation between the three designs and to verify that the trapping layers perform as intended. The No-TL and TL180 devices were removed from the aging rack after 1200 hours of operation, but the TL80 device was aged for an additional 600 hours to allow for a drop in peak power of at least 15%, which we expected would produce sufficiently clear changes to dislocation structure. Figures 5.4a-5.4c show a large section of each plan-view foil. The MD

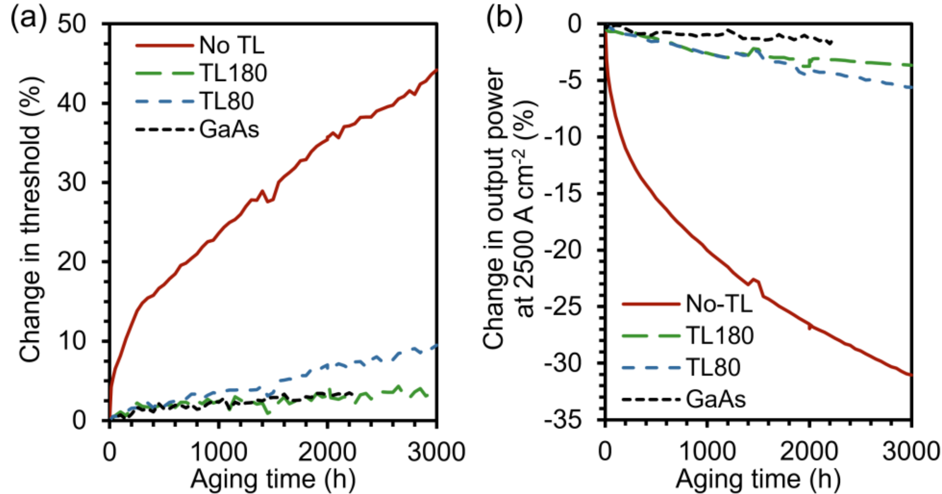

Figure 5.3. 60 °C lifetime testing with performance measurements acquired at 35 °C for high performing devices in this work and similar device structures on GaAs (Ref. 35). The degradation behavior, assessed by comparing (**a**) change in threshold current and (**b**) change in output power at 2500 A cm^{-2} injection, appears remarkably similar between the TL lasers and the native substrate device. Note that due to limitations of the reliability data set for the devices on GaAs, we compare degradation metrics measured at 35 °C (although all devices were aged at 60 °C). Similarly, we compare power output drop at an equivalent current density since laser ridge dimensions are not equal and since peak output power for the device on GaAs was not measured.

densities are all similar at 4.8 μm^{-1} in the No-TL foil and 4.4 μm^{-1} in each TL foil, which reflects the similar MD formation process and the equivalent starting TDD of the templates; the trapping layers simply displace the location of MDs vertically, but this is not discernable from this plan-view projection alone.

The No-TL device in Figure 5.4a shows that many MDs, which are straight before aging [29], have become wavy due to REDC. A closer examination in Figure 5.4d reveals that, in fact, all MDs show some signs of REDC as small jagged features along their length. Without TLs, all MDs in this sample lie along the uppermost or lowermost QD layer (shown schematically in Figure 5.4a inset) and facilitate significant non-radiative recombination. Further, the energy released in this process allows MDs to increase their length by emitting point defects (i.e. undergo REDC), which explains the sharp degradation in No-TL laser performance. We believe that the large variation in the extent of climb of individual MDs is, in part, a result of whether a given MD lies above or below the active region. As the active region itself is modulation p-doped, MDs on the bottom (near the n-doped cladding) may see larger minority carrier densities and hence undergo more REDC than those above the active region. At the same time, we expect MD densities to be lower on the n-side [102]–[104], so only a few MDs show such large amounts of climb.

Dislocations in the aged TL180 and TL80 lasers, shown in Figure 5.4b and 5.4c, appear entirely straight with no evidence of REDC. Looking more closely, however, in Figure 5.4e and 5.4f we see a few instances of climbed MDs, marked by yellow arrows, based on their faintly jagged appearance. Overall, only 9% and 1% of the total MD length in the TL180 and TL80 foils, respectively, show clear signs of climb compared to 100% of the MDs in the no-TL laser. All remaining MDs appear entirely straight, which indicates that both TL designs

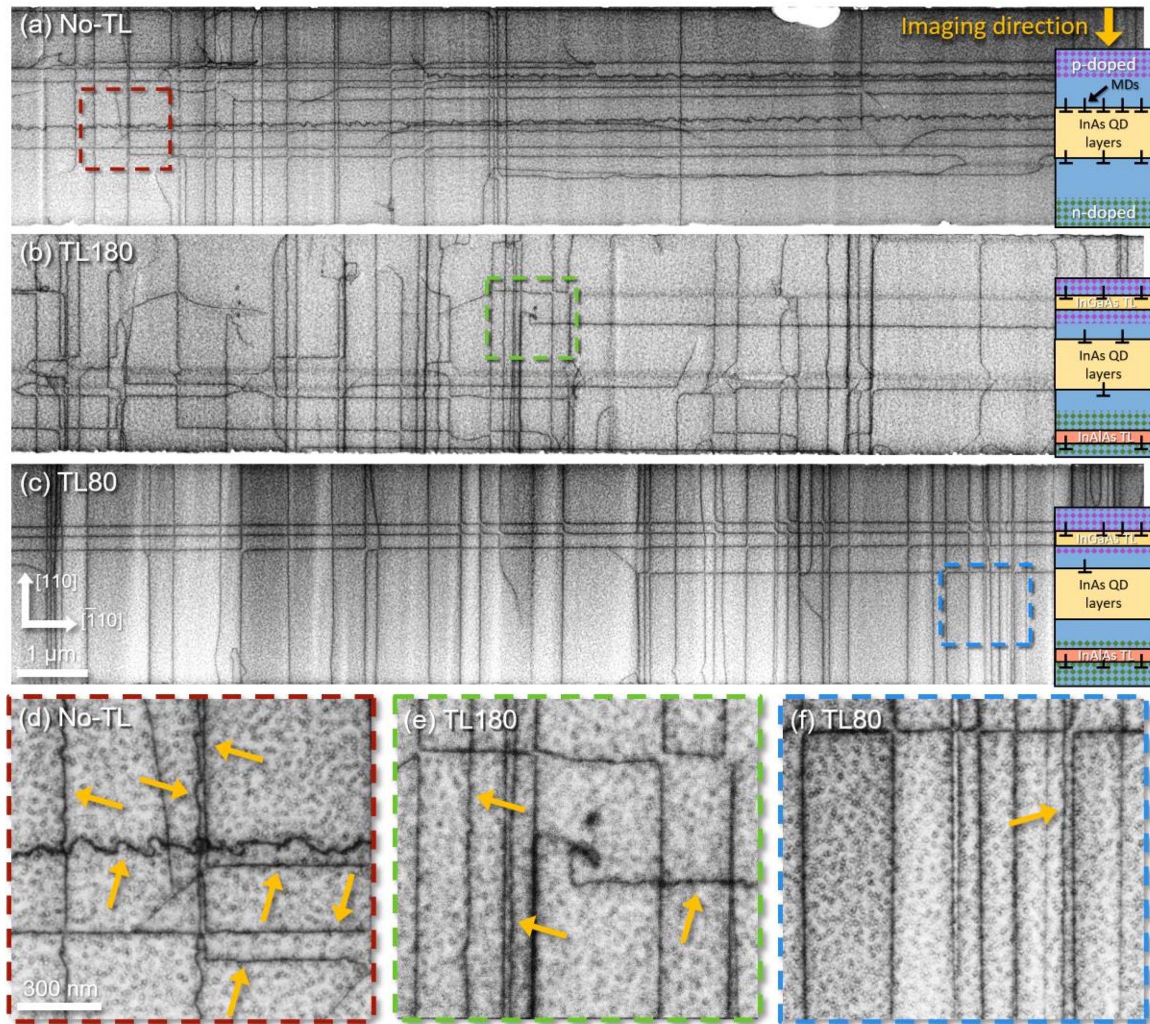

Figure 5.4. **(a-c)** Plan-view scanning transmission electron microscopy images (imaged slightly off the (001)-zone axis to improve dislocation contrast) from aged (a) No-TL (1200 h), (b) TL180 (1200 h), and (c) TL80 (1800 h) lasers. Their misfit dislocation (MD) densities are 4.8μm^{-1}, 4.4μm^{-1}, and 4.4μm^{-1}, respectively. The schematic insets denote where we expect the MDs lie in each structure. In (a) the No-TL laser, these lie adjacent to the upper and lower QD layers, so MDs here show moderate to extensive degrees of waviness due to recombination-enhanced dislocation climb (REDC), as detailed in (d). In the TL lasers, most MDs lie at the trapping layer and do not show any signs of climb, consistent with lying at the TLs. Some exceptions are noted in (e) and (f), marked by yellow arrows. 100% of MDs in No-TL show evidence of REDC compared to 1% (9%) of MDs in TL80 (TL180). The peak output power drop after 1200 h for the devices from (a-c) is 84%, ~30%, and 8%. Each foil is ~600-950 nm thick with ~70 μm^2 of total imageable area. After [191].

expel MDs sufficiently far into the doped regions where minority carrier concentrations are sufficiently low that REDC is not apparent. We note that the TL80 device appears the least degraded, despite operating for an additional 600 hours, a result of these trapping layers being

more effective at holding MDs away from the active region. Further improvements may be possible with even closer spacing, however, at some spacing, degradation due to REDC of trapped MDs will outweigh the benefits of increased trapping effectiveness.

To confirm that the small fraction of climbed MDs in the TL samples indeed lie at the QD layers rather than the trapping layers, we generate a tomographic reconstruction (Figure 5.5) of the section of the TL80 foil from Figure 5.4f by taking multiple PV-STEM images across a range of tilts. The depth resolution obtained in this work clearly distinguishes between the individual QD layers spaced vertically about 40 nm. While the trapping layers themselves are not visible in the tomogram, most MDs lie at the

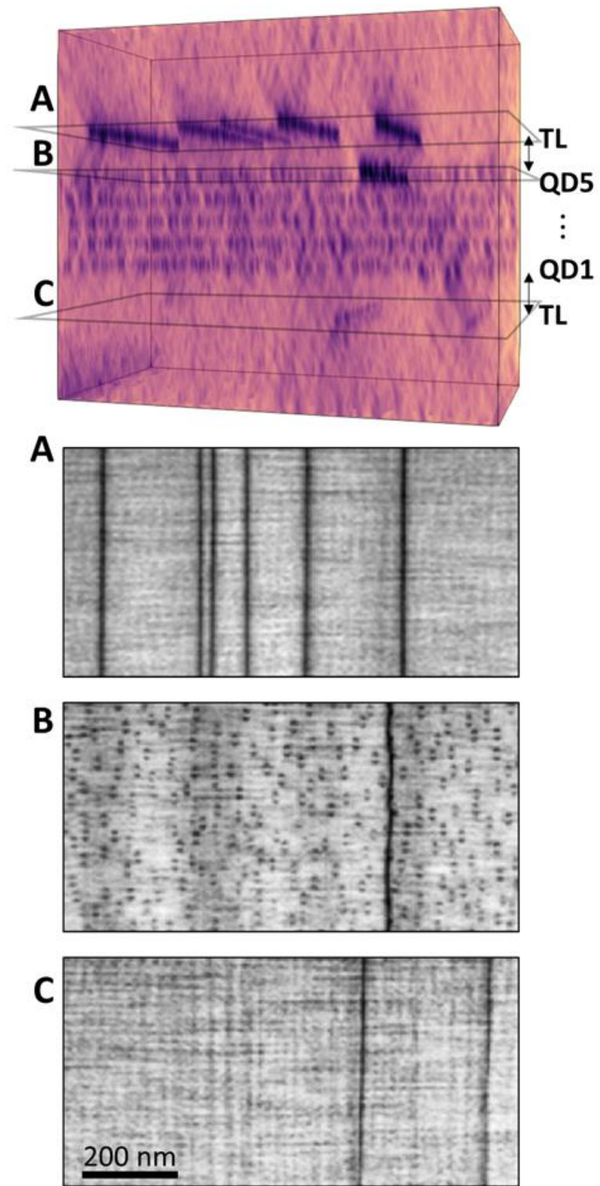

Figure 5.5. Tomographic reconstruction from electron micrographs of TL80 laser active region and trapping layers. Thin pseudo-plan view images show a single misfit dislocation (MD) lies near the QD layers (section B); all other MDs lie at the position of the upper trapping layer in the p-doped cladding (section A) or at the lower trapping layer in the n-doped cladding (section C). The trapping layers themselves are not visible in the reconstruction due to low, uniform strain. After [191].

expected height (~80 nm) either above the active region in the p-doped cladding (section A) or below in the n-doped cladding (section C). As predicted, only the single wavy MD with unambiguous evidence of REDC lies at the QD layer (section B), in this case just above. Figure 5.6 presents an analogous tomographic reconstruction of TL180, showing one trapped MD and one MD at the fifth QD layer. As in TL80, the MD at the QD layer shows evidence of REDC, while the trapped MD remains straight. Note that, in both reconstructions, we cannot extract vertical positional information from MDs with a line direction perpendicular to the tilt axis, so we exclude these sections from the reconstructed areas in Figures 5.5 and Figure 5.6. For tomograms of comparable no-TL structures, see Refs. [94], [100].

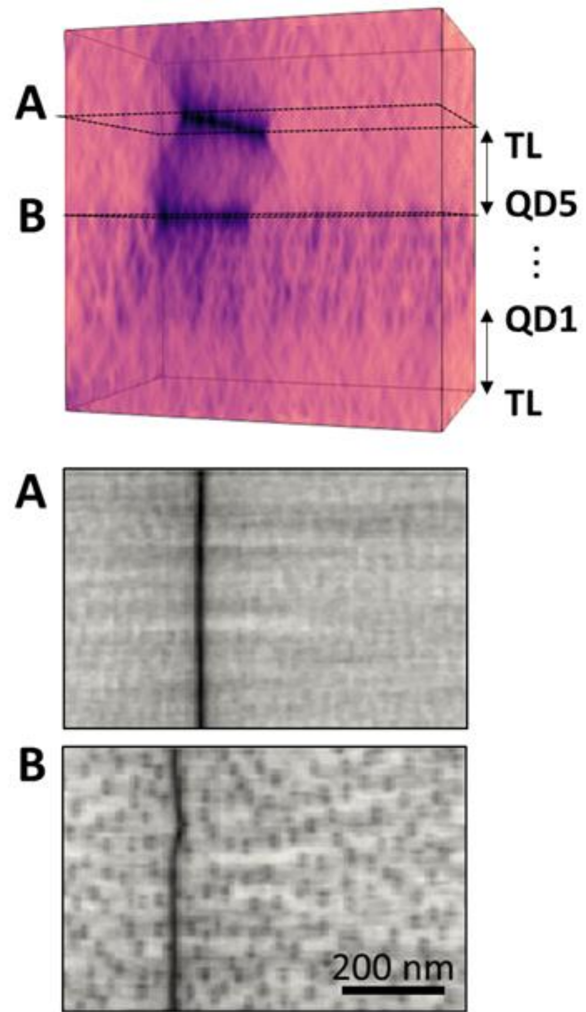

Figure 5.6. Tomographic reconstruction from electron micrographs of TL180 laser active region and trapping layers. The pseudo-plan view images from heights A and B each show a misfit dislocation (MD). The MD at the upper trapping layer in the p-doped cladding (section A) appears straight, while the MD near the QD layers shows evidence of recombination enhanced dislocation climb (section B). The trapping layers themselves are not visible in the reconstruction due to low strain.

The 9× lower MD length undergoing climb in TL80 compared to TL180 likely holds clues to making the trapping layers completely effective in displacing MDs and offers scope for further improvement. Although we have not yet identified the exact mechanism that results

in some MDs forming at the QD layers in TL structures, the reliability data and microstructure analysis of TL lasers suggest that the spacing between the QDs and trapping layers plays an important role in the process. The performance difference appears rapidly during lifetime testing, so we suspect that during cooldown (or possibly during the thermal cycling that occurs during growth of the various layers), a wider TL spacing results in a larger driving force for the threading segment between the QD layer and trapping layer to glide and form a MD segment at the QD layer. Therefore, trapping layers are more effective when placed closer, however the MDs located there will see increasing minority carrier concentrations as they approach the edge of the doped cladding, so a balance between the factors is necessary for optimal performance.

In early GaAs-AlGaAs double heterostructure and quantum well lasers, REDC proceeded rapidly resulting in huge dislocation networks called dark line defects [105]. The situation is different for InAs QD lasers where REDC proceeds only gradually thanks to their unique electrical [28] and mechanical properties [32], in a similar vein to InGaAsP [106]–[109] lasers. In both TL structures (Figure 5.3b, 5.3c), the total change in line length we observe is nearly negligible and may seem incongruous with the changes in their performance. Increasing MD length necessarily increases the total number of dislocation trap states but only to an extent. Thus, we must also consider the generation of point defects by REDC which are invisible in PV-STEM. As we note in Ref. [100], assuming a 5 μm point defect diffusion length, a uniform lateral excursion of a MD of only 10 nm emits approximately 10^{18} cm^{-3} point defects in the active region. These generated point defects can facilitate additional non-radiative recombination and lead to additional darkening. The origin and nature of point defects participating in REDC therefore requires further investigation.

Finally, the dissipation of heat through non-radiative recombination increases the junction temperature [110]–[113], which may, in turn, increase local point defect diffusion and exacerbate REDC. Besides the obvious problems posed by these mutually- and self-reinforcing processes (e.g. thermal runaway at hotspots has been shown to kill InAs QD lasers [114]), the increased junction temperature poses additional problems: both gain [88], [115]–[117] and T_0 [118] in QD lasers have been shown to decrease with increasing temperature. Improvements in rollover and VI behavior, particularly for TL80, suggest that trapping layers substantially reduce excess junction heating.

V. Conclusions

In summary, we have demonstrated that inserting trapping layers above and below the active region of InAs QD lasers substantially improves reliability, even outlasting lasers with lower TDDs. Trapping layers are robust and prevent dislocation climb on about 91–99% of the observed MDs even after 1800 hours of aging. This has a variety of beneficial effects with substantially lower defect generation leading to lower device heating and greatly improved laser performance over time. Within the trapping layer design space, we find that a displacement of just 80 nm away from the QD layers is more effective than 180 nm since fewer MDs form at the QD layer interface while the MDs at the closer trapping layers do not show signs of increased climb. However, the work to improve TL design is ongoing. Their ideal thickness, composition, and placement require optimization on both the p- and n- sides of the junction. This is detailed further in Chapter 9. With the impact of MDs largely eliminated from InAs QD lasers, we will soon turn to examining the slower point-defect-based gradual degradation processes (Chapter 8). In the final chapter, we will explore how trapping layers might be applied to InGaAs QW lasers on silicon.

6. Trapping Layers for Regrowth after Heterogeneous Bonding

I. Introduction

This chapter examines an alternative heterogeneous integration scheme, in some ways a mix of typical heterogeneous and monolithic integration methods. This involves first bonding a thin high-quality III-V template layer onto silicon and then growing the laser structure on top. The motivation for this is that it inherits some advantages of direct growth, such as enabling III-V growth and processing on larger silicon substrates, thus reducing costs, while the bonding eliminates egregious sources of defects such as lattice mismatch and crystal structure mismatch [119]. Additionally, the post-bond regrowth technique has advantages over the full stack bonding-based heterogeneous integration method with increased flexibility for dense and interspersed integration. Multiple epitaxial structures for different photonic integrated circuit devices may be integrated through separate regrowths by having specific sections of the wafer masked off. While this multiple-regrowth technique is also possible with direct growth, the accompanying thick buffer layers for defect filtering add growth time and place the device structures farther from the substrate and makes certain coupling schemes like evanescent coupling challenging [120].

The bonded film will typically also have a mismatch in coefficient of thermal expansion with the substrate, which strains the film at growth temperature. Therefore, even subsequent homoepitaxial or lattice-matched regrowth has some 'thermal' critical thickness for stress relaxation by dislocation generation, requiring either very thin epitaxial structures or strained dislocation blocking layers to keep high densities of dislocations from affecting the active region. Post-bonding regrowth does present additional challenges such as requiring the bond to withstand vacuum conditions and high growth temperatures, but this has been effectively

handled by careful selection of bonding conditions and the inclusion of outgassing channels to allow evolved gases to escape from the bond interface and prevent delamination of the film [121], [122].

This post-bond regrowth technique, in various forms, has been attempted on InP-based templates with promising results, first by researchers at NTT [123], [124], who keep total film thicknesses below thermal critical thickness, and at UCSB [125] and HPE [126], who show that low defect densities can be maintained even in films with thicknesses several times beyond critical thickness. In this chapter, we explore the feasibility of this technique for GaAs-based templates. Growing a functional epitaxial structure below thermal critical thickness is challenging when using GaAs as the thermal expansion mismatch of GaAs (α=5.7 ppm/K) with silicon is 60% larger than InP (α=4.6 ppm/K) with silicon (α=2.6 ppm/K). Here, we focus on reducing threading dislocation (TD) densities (TDDs) that arise due to thermal mismatch by using a simplified GaAs-based regrowth structure and inserting strained dislocation trapping layers. We explain where and how threading dislocations originate in these structures and conclude with a brief discussion on implementation schemes for quantum well- or quantum dot-based device structures.

II. Experimental Details

To prepare a GaAs-based film for bonding, we grow a 400 nm $Al_{0.80}Ga_{0.20}As$ etch-stop layer on a GaAs wafer, followed by a 200 nm n-doped GaAs-based template layer, containing a two-period AlGaAs superlattice (7.5 nm n-$Al_{0.20}Ga_{0.80}As$/7.5 nm n-GaAs) grown 17.5 nm from the surface to minimize surface roughness for bonding and potentially to getter impurities and point defects originating from the bond interface. The GaAs wafer is bonded onto a pre-patterned silicon-on-insulator (SOI) substrate by direct wafer bonding at 200 °C described in

Ref. [126]. The substrate is removed by mechanical polishing and selective wet etching. Finally, the etch-stop layer is removed by a second selective wet etch in dilute HF and the sample is quickly loaded into a Veeco Gen III molecular beam epitaxy (MBE) chamber to minimize surface oxidation.

Before growth, the thin surface oxide is thermally desorbed in the MBE chamber at 595 °C for about 15 min, and the GaAs-based regrowth is performed at 580 °C, cooling to 500 °C to grow InGaAs layers. At the end of growth, samples are cooled at 10 °C/min to room temperature. TDDs were measured on a Thermo Fisher Apreo S scanning electron microscope (SEM) using electron channeling contrast imaging (ECCI) by tilting to the intersection of the 400 and 220 channeling conditions. Cross-sectional foils were prepared using an FEI Helios Nanolab 600 Dualbeam focused ion beam (FIB) microscope and imaged with a Thermo Fisher Talos microscope in scanning transmission electron microscopy (STEM) mode with a bright field detector.

III. Dislocation-Filter-Free Structures

As these GaAs template structures are bonded to the SOI substrate before growth, the lattice mismatch between GaAs and silicon is of no consequence for TD formation. However, since bonding and growth occur at very different temperatures, thermal expansion mismatch strain is a concern. We illustrate how the thermal strain in the GaAs film evolves over time in Figure 6.1a. When the template is bonded at 200 °C, it is nominally unstrained, but as it is cooled to room temperature, it becomes tensile strained due to thermal expansion mismatch. When heating the sample up to growth temperature, the strain state reverses above 200 °C as thermal compressive strain develops and should rise to 0.12% at the growth temperature of 580 °C assuming negligible strain relaxation through substrate bending. With this strain, the

Matthews-Blakeslee critical thickness for misfit dislocation (MD) formation from pre-existing threading dislocations (TDs) [127] is 120 nm, but this is not a concern for the 200 nm bonded film. As the starting TDD is very low—likely below 10^4 cm^{-2} after bonding but prior to growth—any significant relaxation requires the nucleation or multiplication of new dislocations, which is a kinetically-limited process, and the TDD escalates only when films are grown 4–7× beyond the critical thickness. We examine a film with a minimal regrowth thickness of 30 nm (just enough to smooth the surface after oxide desorption) and find just a single TD over a 10000 μm^2 area examined by ECCI, roughly suggesting a TDD around 10^4 cm^{-2}, comparable to the pre-growth template TDD and in line with expectations.

As we move further beyond this thermal critical thickness necessary for many practical device structures, the TDD begins to increase rapidly. As shown in Figure 6.1b, 500 nm of regrowth, for a total GaAs layer thickness of 700 nm, results in a TDD of about 3×10^5 cm^{-2}. Thicker regrowths raise TDDs exponentially with typical 2.2 μm films developing a high TDDs of around $6–8 \times 10^6$ cm^{-2}, which may significantly limit the operation of certain classes of devices and diminishes the merits of bonding. These elevated TDDs forming due to thermal expansion mismatch may also explain performance degradations that other researchers have observed in similar regrowth scenarios, for example in the case of solar cells grown on virtual GaAs substrates transfer-printed to silicon and sapphire [128], [129].

Returning to Figure 6.1a, we plot several strain evolution profiles to illustrate why TDDs increase and how this might be avoided. (i) In the simplest edge case, effectively no dislocations nucleate and the film does not relax at all during growth. This outcome is only

achieved for very thin structures grown not far beyond critical thickness, such as with the 30 nm regrowth structure mentioned previously. (ii) In the opposite edge case, all the thermal compressive strain is relaxed during growth by pre-existing TD motion or nucleation. Unfortunately, this initial compressive strain relief gives rise to a second potential source of TD nucleation as now tensile stress builds in the GaAs during post-growth cooldown, again due to thermal expansion mismatch with the substrate. For this second wave of TD nucleation to be an important source, nearly all the initial compressive stress must be relaxed during growth; otherwise, tensile strain will not begin building to levels high enough for dislocation nucleation until very low temperatures (200-300 °C) where dislocation nucleation

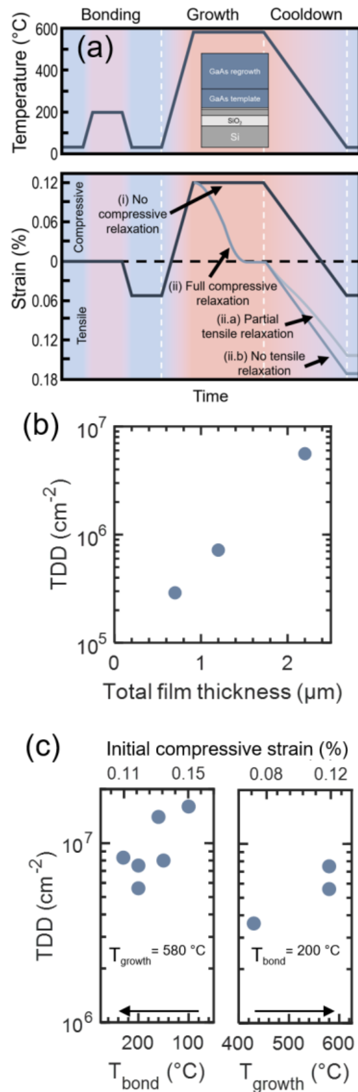

Figure 6.1. Dislocation evolution in homoepitaxial GaAs regrowths. (a) A sketch of the temperature and strain evolution during bonding, growth, and cooldown. Strain fluctuates due to thermal expansion mismatch once the template is bonded to the substrate. Several dislocation-mediated strain relaxation pathways are drawn for the boundary cases of and (i) no relaxation and (ii) full relaxation during growth and for (ii.a) partial and (ii.b) no relaxation during cooldown. (b) Threading dislocation densities (TDDs) rise exponentially with regrowth film thickness. (c) Dependence of TDD on bonding temperature for fixed growth temperature of 580 °C (left) and dependence on growth temperature at fixed bonding temperature of 200 °C (right). Across the series of 2.2 μm GaAs films, both techniques reduce final TDD, but the effect is limited. All strain values are calculated based on the thermal expansion mismatch. After [209].

rates and glide velocities [103] become vanishingly slow. Branching off this path during the cooldown phase, we point out the two boundary cases: (ii.a) a partial relaxation path where existing dislocations or new dislocations are nucleated to relax the film and (ii.b) a no relaxation path despite the building tensile strain. We do not draw a full relaxation path during cooldown because this is infeasible given the restricted dislocation nucleation and glide. We will revisit the mechanism details behind these various paths in Section V.

One potential method to reduce dislocation densities, given that dislocations nucleate in response to thermal stress, is to reduce the initial compressive thermal strain. We can do this by either lowering the growth temperature or raising the template bonding temperature. While both methods reduce initial compressive strain equally, lowering the growth temperature also lowers the thermal-expansion-induced tensile stress that builds up during cooldown, so we will look at their effects separately. From Figure 6.1c, the bonding temperature series of 2.2 μm thick GaAs films does indeed show lower TDDs with reduced thermal strain, but the effect is modest. A similar trend is seen by lowering the growth temperature. We note that extrapolating the exponential trends in Figure 6.1c back to zero initial compressive strain would only predict a TDD of around 1×10^6 cm^{-2}, far higher than pre-growth template levels, suggesting that initial compressive stress alone does not explain the TDD dependence of the films. Further, the effects of either modification examined so far are too modest to be practically useful and cannot be extended further as there are limits to how high the bonding temperature or how low the growth temperature can be pushed without encountering issues with growth defects and bond integrity.

IV. Strained Dislocation Trapping Layers

We now explore the potential for strained dislocation trapping layers to shield specific sections of the film from thermal-expansion-induced dislocations. Irrespective of the sign of strain (compressive or tensile), a common mechanism for TD formation involves the nucleation of dislocation half loops from a free surface, non-epitaxial interface, or defect and its subsequent growth through the film to relieve strain. Under modest strain conditions, these half loop dislocations can be blocked by an oppositely strained epitaxial layer, which the dislocations cannot propagate through because doing so would increase the strain in that layer, which is energetically unfavorable. This manifests as a repulsive force felt by half loop dislocations as they approach the layer, resulting in misfit dislocations forming at the interface of the trapping layer [77], [80]. The exact location where these misfit dislocations form gives clues to the nucleation location and stress state during nucleation. With our available MBE growth sources, we can only grow compressive-strained InGaAs layers, which are only effective at blocking dislocations nucleated during cooldown under tensile strain.

We grow two additional 2.2 μm films, one with a pair of 5 nm $In_{0.15}Ga_{0.85}As$ trapping layers spaced 25 nm apart and grown 100 nm above the regrowth interface and another similar to the first but with an additional pair of trapping layers 200 nm from the surface. Pairing the trapping layers in these structures allows us to later use cross sectional STEM to determine whether MDs originate from above or below each set of trapping layers. Compared to the GaAs-only regrowth with a TDD of 7.5×10^6 cm^{-2} (Figure 6.2a-b) (measured from 114 counted TDs), the structure with bottom-only trapping layers (Figure 6.2c) shows an impressive 8× reduction in surface TDD (9.5×10^5 cm^{-2}, 57 TDs counted) (Figure 6.2d) as measured by ECCI. Inserting the additional upper pair of trapping layers (Figure 6.2e) cuts the surface TDD by more than

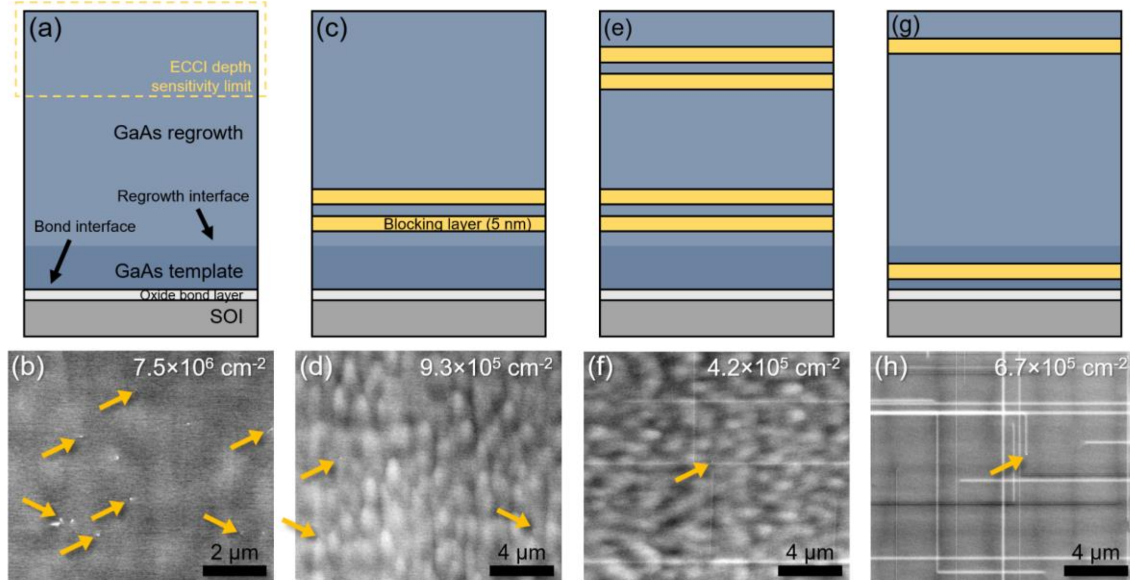

Figure 6.2. Trapping layers to reduce threading dislocation densities. (a) Schematic of a simple 2 µm GaAs regrowth structure (2.2 µm total thickness) with no trapping layers that gives a surface threading dislocation density (TDD) measured by ECCI in (b) of 7.5×10^{6} cm^{-2}. (c) Adding two trapping layers 100 nm above the regrowth interface reduces the TDD to (d) 9.5×10^{5} cm^{-2}. (e) Two additional trapping layers near the top of the structure yield a further two-fold reduction in TDD down to (f) 4.2×10^{5} cm^{-2} with a MDD of 0.13 um^{-1} at the upper trapping layer. (g) Moving the lower trapping layer below the regrowth interface gives a similar TDD as the previous structure of (h) 6.7×10^{5} cm^{-2}, however, the MDD present at the upper trapping layer increases about 10× to 1.4 um^{-1}. The upper trapping layer is spaced 100 nm from the surface in this structure, to improve MD sharpness. After [209].

half again, down to 4.2×10^{5} cm^{-2} (58 TDs counted) (Figure 6.2f), for a total reduction of about 18×. Subsequent growths with similar structures, particularly that presented Figure 6.3 with a single upper and lower trapping layer, have shown TDDs as low as 2.7×10^{5} cm^{-2} (48 TDs counted), a TDD reduction of up to 30× compared to a typical unfiltered regrowth structure. Figure 6.4 shows larger area ECCI images from the structures in Figure 6.2.

Already, this indicates that the majority of TDs observed in the filter-free structures are nucleated during cooldown under tensile stress, not during growth under compressive stress since InGaAs compressively strained trapping layers are ineffective under the latter conditions. This observation strongly indicates that significant tensile stress builds early during cooldown when temperature is sufficiently high for dislocation nucleation and glide. Without

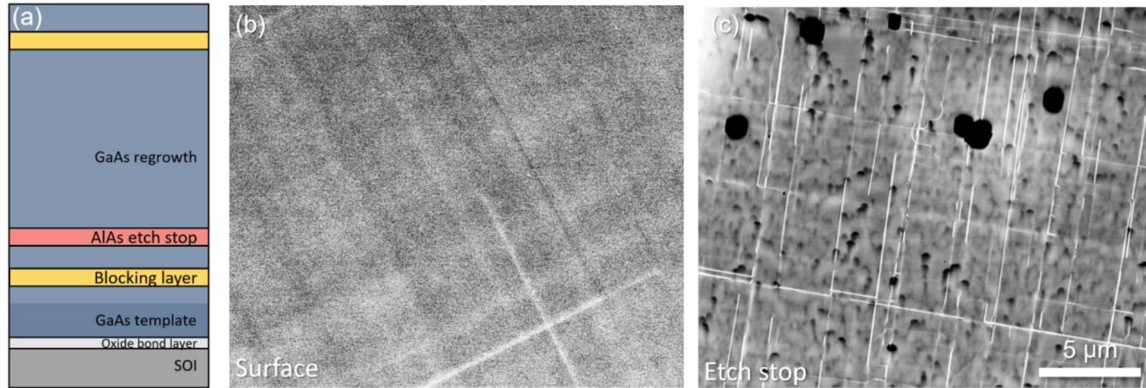

Figure 6.3. (a) Filter structure with an AlAs etch-stop layer to enable for ECCI at the lower trapping layer. (b) ECCI of surface of the structure in (a) showing MDs and a low density of TDs (none visible in area shown). Over 17,000 μm^2 of area imaged, we counted 48 TDs for a TDD of 2.7×10^5 cm^{-2}. (c) ECCI taken after etching the top of the structure down to the etch stop layer showing an array of sharp MDs and a secondary connected set of fainter MDs, which we believe lie at the trapping layer and the regrowth interface, respectively. Misfit dislocation density at the trapping layer is about 6x higher here that in (b). TDD also appears to be higher however, roughness and inconsistent etch pits introduced by the etching precludes an accurate estimate of TDD.

compressive stress relaxation, tensile stress only begins to build below the bonding temperature (200 °C) (see (i) no compressive relaxation pathway in Figure 6.1a), so clearly, most of the initial compressive stress must be relaxed by the end of growth to explain our results, similar to (ii) the full compressive relaxation pathway in Figure 6.1a. The compressive stress relief during growth also must be relaxed extremely efficiently with minimal nucleation of dislocations to realize these large reductions in TDD. To completely relax an initial thermal compressive strain of 0.12% with a TDD of only 2–4×10^5 cm^{-2}, the average glide distance for a TD should be about 3–6 mm, which is plausible considering the temperature, growth time, expected dislocation glide velocities [103], lack of dislocation obstacles, and availability of TD sinks at the edges of the film and at vertical outgassing channels. We also note that because most dislocations are generated in tension during cooldown, a template hypothetically bonded at the growth temperature (for zero compressive strain at start of growth) would still generate

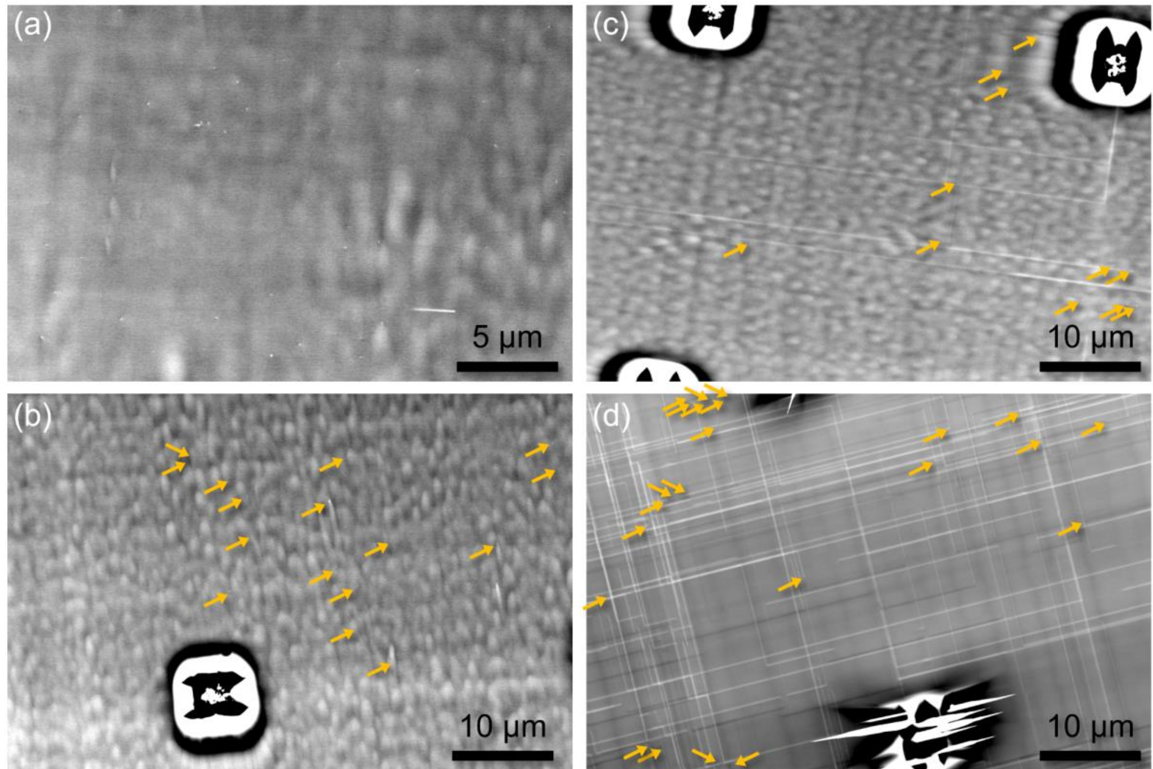

Figure 6.4. Larger area ECCI images of the structures from Figure 6.2. (a) GaAs-only regrowth, (b) two lower trapping layers, (c) two lower and upper trapping layers, and (d) one upper trapping layer with an additional trapping layer in the template. Threading dislocations (TDs) are marked with yellow arrows in all images except for (a) due to the larger density and lower magnification making them easier to see unaided. Note that these represent only a fraction of the total area images, so dislocation density measurements from these images alone can be somewhat inaccurate. The 5-10 μm squares visible in some images are the surface exiting vertical outgassing channels (VOCs) necessary for bond integrity when heating and under vacuum. TDs within 1 μm of these are not counted, in part due to the difficulty seeing dislocations through the rapidly changing background contrast but also because TDs near VOCs are not a concern from a device perspective since the material cannot be used anyway.

many TDD during cooldown, which may explain the weak dependence of TDD on bonding temperature seen in Figure 6.1c.

In a third trapping layer structure (Figure 6.2g), we place the lower trapping layer below the regrowth interface (i.e., inside the GaAs template) to help distinguish between dislocations nucleated at the bond interface and the regrowth interface. With this alteration, dislocations nucleated during cooldown at the regrowth interface but not the bond interface can rise to the

upper trapping layer where they are visible to ECCI. We note that we no longer pair the trapping layers here since, from a dislocation filtering perspective, this is unnecessary: pairing the layers is only intended to aid later STEM analysis, and a single compressively strained trapping layer is sufficient to stop the upward propagation of dislocation loops. In this structure, we measure a surface TDD of 6.7×10^5 cm^{-2} (32 TDs counted) (Figure 6.2h), which is intermediate to the previous two structures, but more importantly there is a strikingly high density of misfit dislocations (1.4 μm^{-1}), which must lie at the upper trapping layer based on the limited 100-200 nm depth sensitive of ECCI. Looking back at Figure 6.2f, there are also several MDs visible but at about a 10× lower density. This indicates that many—perhaps most—dislocations nucleate at the regrowth interface, specifically during cooldown under tensile strain since dislocations nucleated under compressive strain will not be blocked by a compressive strained layer as mentioned before. While it seems likely dislocations also nucleate from the bond interface, we do not have direct evidence to conclude this. We note that most MDs in Figure 6.2h end with fading contrast indicating that the TDs at each end point downward, which we do not include in our TDD count. We will describe how these MDs might be forming shortly.

We verify the low surface TDDs from the structure in Figure 6.2e using plan-view (PV) STEM as it can be challenging to spot all dislocations using ECCI at very low TDDs. Rather than preparing a foil from a random site, we deposited fiducial markers in several locations and imaged those regions in ECCI and then selected a site for PV foil extraction that contained one TD (white arrow) visible to ECCI as well as two MDs (blue arrows), as seen in Figure 6.5a. In Figure 6.5b STEM imaging of the PV foil, which contains only the upper two trapping layers, confirms the presence of the TD and MDs seen by ECCI, but there is one additional TD

indicated by the black arrow. However, by tilting the foil 7° into the (220) diffraction condition, TDs can exhibit point contrast (see the white dot at the end in the inset) where the TDs intersect the foil surface, and since this foil is imaged from the bottom (electron beam traveling in the upward growth direction), the point contrast of this TD indicates it exists only below the trapping layers. This is further supported by the longer projected length of these TD segments since the foil contains more material below the trapping layers than above. The expected dislocation configuration is depicted schematically in Figure 6.5c. The single surface TD found in the 20 µm × 13 µm PV foil equates to a TDD of 4×10^5 cm^{-2}, which while carrying little statistical meaning, particularly given the non-random site selection,

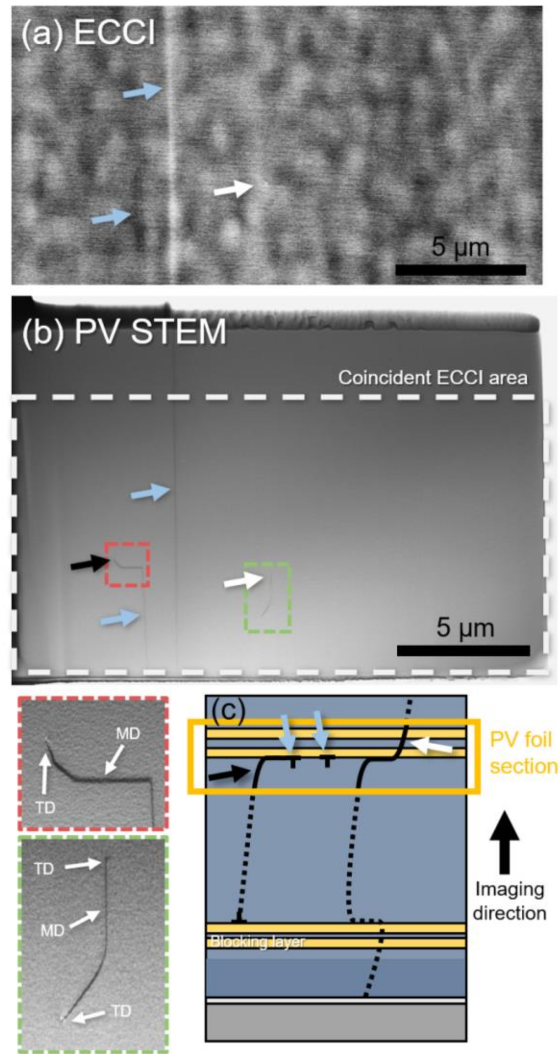

Figure 6.5. (a) ECCI of a region from the structure in Fig 2e showing a single threading dislocation (white arrow) and two misfit dislocations (blue arrows). (b) A plan-view STEM image covering the same region shows the same features from the ECCI image but with an additional threading dislocation (black arrow), which is not visible in ECCI because it exists only below the lower trapping layer as depicted in the schematic in (c). The insets for (b) show enlarged views of the two TDs to better show the point contrast for each. Some misfit dislocation growth is apparent between the ECCI image and the PV-STEM image due to the heavy excitation of the region during imaging and foil preparation. In the schematic in (c), the dislocations observed in (a) and (b) are shown with solid lines, and one possible version of their extended structures are represented by dotted lines. After [209].

does happen to closely match our large scale ECCI measurement of TDD of 4.2×10^5 cm^{-2}. Based on these analyses, we conclude that our ECCI measurements do not systematically miss significant numbers of surface exiting TDs.

Cross sectional STEM, shown in Figure 6.6a and 6.6b, also from the structure from Figure 6.2e largely confirms the expected position and origin of misfit dislocations in these structures. In order to sample both orthogonal sets of [110] and [$\bar{1}$10] MDs, we prepare [100]-oriented cross sections (rotated 45° from the more typical ⟨110⟩-type cleave-plane-parallel orientation, see Figure 6.6a inset), which makes all MDs appear as short horizontal line segments passing through the foil thickness. From STEM it is clear that the large majority of dislocation loops are contained below the lower trapping

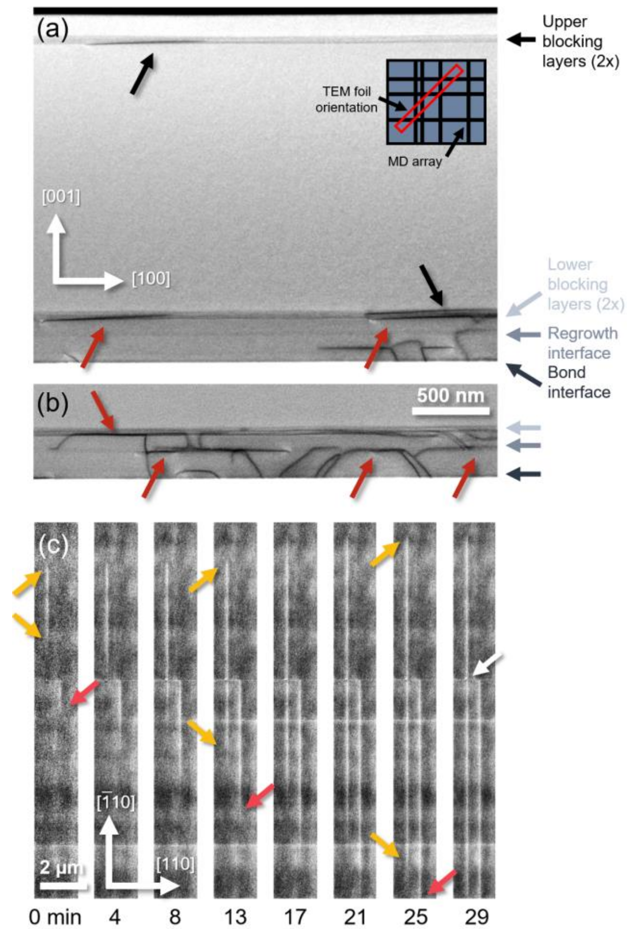

Figure 6.6. (a) Bright-field STEM of a [100]-oriented cross section of the trapping layer structure from Figure 6.2e. (b) Additional section of the lower trapping layer region showing more examples of captured MDs. Most misfit dislocations form at the lowermost trapping layer or regrowth interface (red arrows). A smaller number of misfit dislocations (black arrows) form at the inner two trapping layers. In total we observe 34 MD segments below the lower trapping layer, 2 above the lower set, 5 below the upper set, and 0 above the upper set. (c) Time-lapse sequence of plan-view ECCI of misfit dislocations growing just below the upper trapping layer. The yellow and red arrows follow the ends of two different growing MD segments. The white arrow points out a separate TD, unrelated to either MD. The structure imaged is similar to Figure 6.2e but with a single upper trapping layer spaced just 100 nm from the surface for improved MD sharpness and a single lower trapping layer. The frame period is 250 s while scanning with a beam current of 3.2 nA over a 1140 μm^2 area at 30 kV. After [209].

layers with MDs forming at either the lowermost trapping layer or the regrowth interface (red arrows). These dislocations must nucleate either at the bond or regrowth interface during cooldown under tensile stress, as predicted earlier. The MDs held at the regrowth interface are likely pinned there by residual oxide or contaminants. This is further supported by Figure 6.3c where ECCI taken just above the lower filter layer shows MD segments of individual dislocations transitioning between two heights, apparently due to periodic pinning at the regrowth interface. From the STEM images in Figure 6.6a and 6.6b, there is also a much smaller number of MDs lying on the inner surfaces of either trapping layer (black arrows), i.e. above the lower trapping layers or below the upper layers, whose origin we will describe shortly. The upper set of these is what we observe in ECCI in Figure 6.2f. There are no observable MDs lying above the upper set of trapping layers indicating half-loop nucleation from the surface is not a significant dislocation source, at least during cooldown, which is unsurprising given the smooth growth surface and moderate stress conditions [130].

The ECCI time-lapse sequence in Figure 6.6c provides further evidence that these misfit dislocations form under thermal tensile strain. During imaging at room temperature, regardless of any stress relaxation occurring during growth, the GaAs film must be tensile strained (see Figure 6.1a). Normally, dislocations in brittle semiconductors are frozen at room temperature, but under electron-beam irradiation, electron-hole pairs are generated and recombine, supplying energy to locally reanimate dislocation glide—a phenomenon known as recombination-enhanced dislocation glide (REDG) [57], [62], [131]. The time-lapse sequence shows new and pre-existing dislocations forming and growing by this process on the underside of the upper trapping layer in a structure similar to that in Figure 6.2e. Two observations prove that these misfit dislocations form in response to tensile stress during cooldown rather than

compressive lattice mismatch of the InGaAs layer during growth. First, the MDs continue to expand at room temperature, and although expansion alone does not preclude the initial MDs from forming by InGaAs relaxation, this would be energetically unfavored since the trapping layer is grown below critical thickness, whereas tensile stress relaxation of the GaAs is energetically favored. Second, we see that both ends of the MDs gradually fade, showing no indication of the sharp point contrast that is characteristic of surface-terminating TDs, one of which is marked by a white arrow in Figure 6.6c. The fading contrast indicates that the two TD ends of the MD point downward, a configuration that is inconsistent with relaxation of the InGaAs layer during growth. This MD configuration further hints at the possible mechanism behind how these upper trapping layers reduce surface TDD. Given the lack of dislocation nucleation sources between the upper and lower trapping layer in this structure, this MD may have formed as a result of an impeded dislocation multiplication process, e.g. Frank-Read source or spiral source [132], which in the absence of the upper trapping layer would rise to the surface and form two new TDs.

V.Dislocation Formation and Trapping Layer Mechanisms

We now summarize the formation mechanism for dislocations in these structures and the action of trapping layers to control them based on the evidence shown so far. We suggest referring back to Figure 6.1a to track the changing strain state during growth and cooldown. During growth of the filter-free GaAs structure (Figure 6.7a), the film begins compressively stressed, but as growth proceeds a small population of dislocations (black lines), on the order of $1–5\times10^5$ cm^{-2} (inferred from the remaining surface TDD after inserting trapping layers) are nucleated from the bond and regrowth interfaces and relax compressive stress. By the end of growth of a thick layer (>1 μm), most compressive stress is relaxed, and as the film cools after

growth (Figure 6.7b), the strain state reverses to tensile. Existing dislocations (black lines) are inefficient in relaxing this building tensile strain, in part because they may need to change their line direction, which can be a slow process, but also because their density is low and the temperature is now much lower than during growth. Therefore, stress builds to levels sufficient to nucleate new dislocations (red lines) with the opposite Burgers vector. These dislocations, however, also suffer from low glide velocities due to the low temperature and inherent differences between dislocations nucleated in tension and compression [133], so they too relieve little stress, allowing dislocations to continue to nucleate, ultimately resulting in a large increase in TDD.

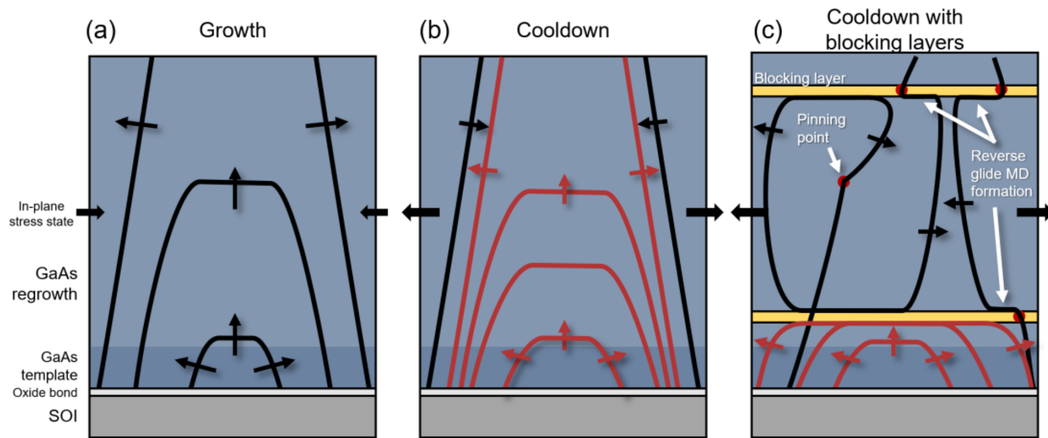

Figure 6.7. Dislocation nucleation process. (a) During growth the compressive strained GaAs film nucleates dislocation loops which expand to the surface to form two independent threading dislocations. Most compressive stress is relaxed during this process by a modest density of dislocations. (b) During cooldown, tensile stress develops and causes opposite signed dislocations (red lines) to nucleate. These glide slowly and do not relax much stress so many dislocations are able to nucleate. (c) Introducing a lower compressive stressed trapping layer blocks the propagation of dislocation loops nucleated from the bond and regrowth interfaces during cooldown in tension, thus reducing the TDD throughout most of the film. A second upper trapping layer inhibits dislocation multiplication, such as the spiral source depicted here, and slightly reduces surface TDD. This also causes MDs to form at the upper trapping layer, visible to ECCI. A second upper MD formation mechanism caused simply by reverse glide of TDs is also depicted. This plays no role in TDD reduction but does relieve some tensile strain. After [209].

Inserting an InGaAs trapping layer near the bottom of the structure, as shown in Figure 6.7c, blocks the passage of dislocations nucleated in tension due to the strain reversal at the interface. It is fortunate that there is such a large asymmetry between the number of dislocations nucleated during growth (in compression) and cooldown (in tension). This disparity may be attributed to different temperatures giving different dislocation glide velocities [103], different partial dislocation configurations in tension and compression [133], and different dislocation nucleation rates [134]. While the most significant TDD reduction is provided by the lower trapping layer, whose mechanism is straightforward, the additional TDD reduction from the upper trapping layer is less obvious. This trapping layer appears to reduce TDDs by inhibiting dislocation multiplication processes, which we depict in Figure 6.7c where a partial spiral source is impeded by the upper trapping layer. Without it, the upper MD segment of the spiral source could exit at the surface to form two new TD segments. This mechanism accounts for the modest 2× TDD reduction (Figure 6.2c-6.2f), the similar densities of MDs seen by STEM on the inner faces of the upper and lower trapping layers (Figure 6.6a, black arrows), and the dislocation configuration seen by ECCI (Figure 6.6c) where a MD connects to two sinking TD segments as depicted in Figure 6.7c. A superficially similar MD configuration can form if a preexisting straight TD reverse glides during cooldown in the GaAs region below the upper trapping layer [135], but this does not yield any reduction in TDD. This configuration has been observed but is much rarer since the surface TDD is low and not all TDs are mobile.

We may now better understand the results of the thickness series of GaAs regrowth films discussed in Figure 6.1b, where TDD drops exponentially with decreased regrowth thicknesses. This trend can most plausibly be explained by differing amounts of compressive

stress relaxation during growth. Thinner films should relieve less compressive stress during growth simply because growth time is shorter, giving less opportunity for dislocation nucleation and glide, and because dislocation interactions are more difficult to overcome in thinner films. This alone, however, cannot account for the trend since most dislocations nucleate in tension during cooldown. Instead, the larger residual compressive stress in the thinner films at the end of growth delays the buildup of tensile strain to lower temperatures, and since dislocation nucleation rates vary exponentially with temperature at a given stress, the final TDD should drop exponentially as film thickness decreases.

VI. Alternative Filter Designs and Device Considerations

One potential alternative to these trapping layers for reducing TDDs is to reduce the post-growth cooling rate below the 10 °C/min rate used for all growths so far in order to gradually relax tensile stress using existing dislocations or a small population of additional dislocations. This seems reasonable since we estimate, based on the MD density measured at the upper trapping layer in the structure in Figure 6.2h, that only 16% of the maximum possible tensile strain is relieved during cooldown. We find, however, that reduced cooling rates are entirely ineffective at reducing TDDs: when we lower the cooling rate of a 2.2 μm GaAs film by 100× to 0.1 °C/min, the resulting TDD of 8.9×10^{6} cm^{-2} is certainly no improvement over a standard-cooled film ($7\text{-}8\times10^{6}$ cm^{-2}). The unexpected slight increase in TDD may stem from the ineffective tensile strain relief in these structures, where the slower cooling rate simply provides more time for dislocations to nucleate.

The filtering efficacy might be further improved by inserting a tensile strained trapping layer such as GaAsP to block dislocations nucleated under compression during growth. This could effectively allow thick structures to follow the "no relaxation" pathway illustrated in

Figure 6.1a, similar to how very thin template growths maintain very low TDDs. If compressive stress relaxation is sufficiently reduced or eliminated during growth, then tensile stress will not be able to build to sufficient levels early enough during cooldown when temperature remains high enough to sustain significant dislocation nucleation. Under these conditions, compressive strained trapping layers may not be necessary. However, we could not test this hypothesis as the MBE growth chamber used here lacks a phosphorous source. Despite the hypothetical promises of a tensile-strained trapping layer approach, it could instead be the case that compressive stress would relax by routes that circumvent the trapping layers, such as Frank-Read sources or surface half-loop nucleation.

We note that the purpose of the strained layers used in this study is different from those used in buffer layers of lattice-mismatched heteroepitaxial growth, which generally employ alternating tensile and compressive strained layers to induce back and forth glide of TDs to encourage fusion and annihilation reactions to lower TDD [18], [136]. And while others have incorporated strained defect trapping layers (often strained layer superlattices) near the bond interface of conventional heterogeneous integrated structures [137], [138], only a single tensile and/or compressive stressed layer should be needed to block passage of dislocations. With this post-bonding regrowth technique, we insert an additional defect trapping layer higher in the structure to inhibit dislocation multiplication processes by a mechanism previously detailed by Beanland et al. for strained layer superlattices [80]. An additional tensile stressed layer could also inhibit dislocation multiplication during growth, but it is unclear how significant this process is in these structures.

When applying these filter layers to real device structures, some modifications to the designs investigated here are necessary. These structures are designed to minimize TDD at the

surface, but for a device, the TDD through the active region should be minimized. The only modification needed to achieve this would be to place the trapping layers a short distance above and below the active region. The lower trapping layer performs as before, holding back dislocations nucleated from the bond and regrowth interfaces. On the upper side, dislocation multiplication and reverse glide now occur in thick GaAs-based layers above the upper trapping layer, which now serves to prevent these processes from laying down MD segments directly on top of the active region. We describe this reverse-glide MD formation process and a similar mitigation method in detail in a previous work [135]. Indeed, these trapping layer filters should pair well with typical quantum dot- or quantum well-based active regions, particularly because these active region layers are comparable in composition and strain state to the trapping layers used here. Some optimization of trapping layer composition will also be appropriate to minimize electrical barriers while maintaining highly effective dislocation trapping performance, and the active region must be carefully designed to avoid crossing conventional critical thickness and generating additional dislocations, particularly considering the additional thermal compressive strain present at the start of growth.

VII. Conclusions

We have demonstrated a filtering technique that uses thin single InGaAs trapping layers to reduce threading dislocation densities by up to 30× in regrown films on GaAs templates bonded to SOI, grown well beyond critical thickness. Although the films begin growth compressively strained due to thermal expansion mismatch with the substrate, we show that most dislocations actually nucleate under tensile stress during post-growth cooldown. The trapping layers work primarily by preventing the expansion of dislocations nucleated at the bond and regrowth interfaces. This leaves much of the film with very low defect densities,

suitable for highly defect sensitive devices such as lasers. Further reductions are attainable by inhibiting dislocation multiplication with a second trapping layer, which we demonstrate near the surface but could also be used near the active region of a device. These results highlight the importance of stress concentrators at the interior lower layers that enable dislocation nucleation at stress levels too low for typical half-loop nucleation from a smooth surface.

7. Structural and Luminescent Impacts of Dislocations

I. Introduction

Understanding how dislocations affect the properties of optoelectronic devices like lasers and photodetectors is central to direct epitaxial heterogeneous integration of active devices for silicon photonics. There is ample and growing understanding of the structure-property relationships of dislocation-related electronic states and nonradiative recombination of charge carriers in semiconductors like Ge [139], GaAs [140], and GaN [141], [142], but there is a growing realization that the impact of dislocations goes beyond this static and often idealized picture. Dislocations may affect a heterostructure device even before device operation by altering the local composition or growth rates during synthesis, exemplified by prior work on dislocation-induced phase separation in alloys [143], [144] and roughening surfaces [145], [146]. Dislocations continue to modify device behavior long after fabrication by diffusing or transporting dopants and other impurities during device operation [147], [148] or, more dramatically, by damaging devices via recombination-enhanced dislocation motion where dislocations inject point defects and subsequently increase in length over time via dislocation climb [97], [149]–[151].

Understanding these broader impacts of dislocations will further the development of self-assembled epitaxial InAs quantum dot (QD) lasers on silicon [152]–[155]. There is also a wide range of other metamorphically grown III-V structures such as multijunction solar cells[156] and various photodetectors [157], lasers [158], and single-photon sources [159], often based on InAs QDs [160] and InSb QDs [161], all of which can benefit from a detailed representation of dislocation behavior and their local environment.

For InAs QDs on silicon specifically, one important consideration is the direct impact of dislocations on QD formation since their growth window is narrow—and hence more sensitive—to perturbations than conventional III-V quantum well (QW) heterostructures. This is especially important when considering growth and design changes needed to realize reliable and viable integration schemes. For example, cracking during cooldown is a frequent problem with thick III-V growth on silicon, particularly when dislocation densities are very low; to address this, future lasers may employ thinner buffer and cladding layers [162]. Additionally, in looking to leverage the full benefits of direct epitaxial growth, future schemes are exploring alternatives to planar laser growth, such as growing lasers in recessed pockets surrounded by a waveguide-containing oxide layer to enable direct edge coupling of the laser [163], [164]. Changes such as these reposition the QDs relative to defect-heavy filter layers and may result in unintended consequences on QD formation and optical properties. Additional issues, such as incomplete characterization of non-radiative recombination of charge carriers at dislocations in QD systems and the sizeable thermal strain due to the silicon substrate, which continues to drive recombination-enhanced dislocation motion during operation [165], must also be examined.

In this chapter, we use a combination of microanalysis techniques on a model shallow (near-surface) layer of InAs QDs on silicon to show that dislocations not only reduce excess carrier lifetimes and emission intensities at room temperature, but they also introduce non-trivial crosshatch- and hillock-induced compositional shifts that locally alter the QD energy levels and intensity. Properly accounting for these effects in laser design and growth can yield improved laser performance and reliability.

II. Sample Details and Experimental Methods

The InAs QD model structure investigated here was previously reported in a multi-modal characterization study [165]. Briefly, we use molecular beam epitaxy (MBE) to synthesize the structure depicted in Figure 7.1a with an active layer consisting of a single shallow InAs QD layer embedded in a 7 nm $In_{0.15}Ga_{0.85}As$ quantum well and capped by a 100 nm thick GaAs layer. The QD layer is not intentionally doped. To ensure epilayers free of anti-phase domains, we employ a thin metalorganic chemical vapor deposition (MOCVD)-grown GaP-on-Si template from NAsP III-V GmbH in which anti-phase domains are made to self-terminate. The lattice mismatch is managed with a low temperature GaAs nucleation layer followed by high temperature GaAs growth. Dislocation densities are reduced using two defect-filter structures—a 200 nm thick continuous InGaAs layer and a 10-period strained-layer superlattice of 10nm/10nm $In_{0.1}Ga_{0.9}As$/GaAs (Figure 7.5e for a cross-sectional scanning

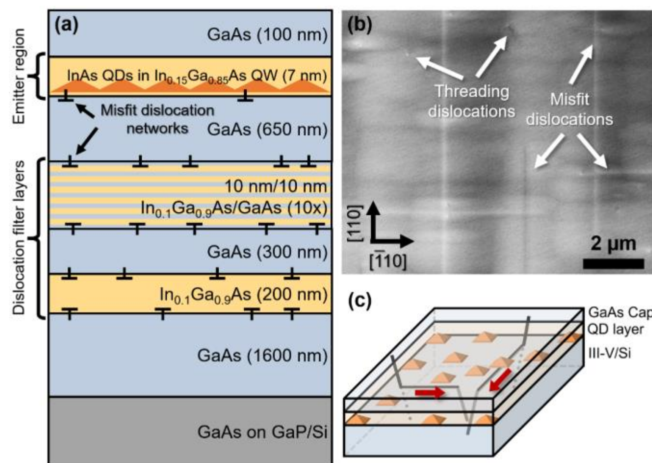

Figure 7.1. (a) Structure of sample characterized in this study. (b) Electron-channeling contrast imaging (ECCI) from the sample surface showing a moderate density of threading dislocations and misfit dislocations located just below the QD layer. (c) Illustration of the misfit dislocation formation process in which thermal expansion misfit stress generated during cooldown propels free threading dislocations below the QD layer to glide. The TD segment is pinned through the QD layer and cannot follow the lower thread segment, so a misfit dislocation forms here. After [210].

transmission electron microscopy (STEM) image). The threading dislocation density in the sample is 7×10^{6} cm^{-2}, and the InAs QD density is approximately 5×10^{10} cm^{-2}. We also label the locations of misfit dislocation networks in Figure 7.1a, which will be relevant for later analysis. The growth conditions (temperature, V/III ratio, growth rate) of the various layers have been described previously [165].

Optical characterization on the nanoscale was performed by cathodoluminescence spectroscopy (CL). The CL measurements were carried out in an Attolight Allalin 4027 Chronos dedicated CL scanning electron microscope (SEM). CL hyperspectral maps were recorded with an Andor Kymera 328i spectrometer with a focal length of 328 mm, a 150-lines-per-mm grating blazed at 1250 nm, and an Andor 512 px InGaAs diode array camera. Time-resolved CL measurements were performed by triggering the electron gun with the third harmonic of a Nd:YAG laser (355 nm) with a frequency of 80.6 MHz and a pulse width of 7 ps. All CL time decay curves were recorded with a time-correlated single photon counting (TCSPC) setup resulting in a time resolution of about 100 ps. All CL measurements were performed at room temperature with an acceleration voltage of 6 kV (interaction region is ~75 nm radius sphere tangential to sample surface) and a beam current of 30 nA for continuous wave measurements and between 15 pA and 90 pA for pulsed measurements.

Atom probe tips were created using an FEI Helios Dualbeam Nanolab 600 focused ion beam (FIB) microscope using standard 30 kV annular milling steps and a 2 kV broad-area polish to form the final tip shape. Tips were evaporated using a Cameca 3000X HR Local Electrode Atom Probe (LEAP) at 40 K with laser pulsing at a 532 nm wavelength, a 200 kHz repetition rate, and a laser pulse energy of 0.20 nJ. TEM foils were prepared using the FEI

Helios Dualbeam FIB and imaged using a ThermoFisher Talos in STEM mode using a bright field detector with a collection angle of 17 mrad.

Electron channeling contrast imaging (ECCI) was performed on a ThermoFisher Apreo S SEM using a three-beam g=040 and g=220 channeling condition. Figure 7.1b shows a plan-view ECCI image of the structure showing numerous long segments of misfit dislocations along with threading dislocations, which together form the subjects of our study. We have previously determined that these misfit dislocations form just below the 7 nm InGaAs QW/GaAs [165]. The origins of these misfit dislocations, which appear in layers grown nominally below the critical thickness for dislocation glide, is also important to contextualize our results. Briefly, these misfit dislocations form not during growth, but after growth as the sample cools due to a combination of: (1) residual tensile strain in the III-V layers due to thermal expansion mismatch with silicon and (2) local pinning of the threading dislocation segment by the InAs QDs [135]. The formation process is illustrated in Figure 7.1c where only unpinned threading dislocation segments glide below the QD layer to form misfit dislocations. We have identified these misfit dislocations as being primarily responsible for degradation in early generations of GaAs-based lasers on silicon and, more recently, in InAs quantum dot lasers on silicon where their effects can now be largely mitigated using strained indium-containing trapping layers [154].

III. Recombination Dynamics at Dislocations

We use time-resolved CL using a pulsed primary electron beam to probe the effect of dislocations on carrier recombination at room temperature. Our results show the misfit dislocations lying close to the InAs QD layers (Figure 7.1c) are potent nonradiative recombination sites. Figure 7.2a-d shows CL intensity decay traces as a function of increasing

probe current collected at a dislocation-free region and a region with misfit dislocations. The signal is spectrally filtered to separately track the CL intensity decay of the GS (Figure 7.2a-b) and ES (Figure 7.2c-d) luminescence at 1250 nm and 1167 nm, respectively, with a 2 nm bandwidth, hence we directly probe only the occupation of dots emitting in these narrow ranges and indirectly probe most remaining dots via their carrier exchange with the wetting layer, due to fast carrier equilibration at room temperature. The insets in these figures show that the recombination lifetime in both regions, obtained by fitting to a single-exponential decay, are in the 0.2–0.3 ns range and do not vary much with probe current. Upon initial inspection, we

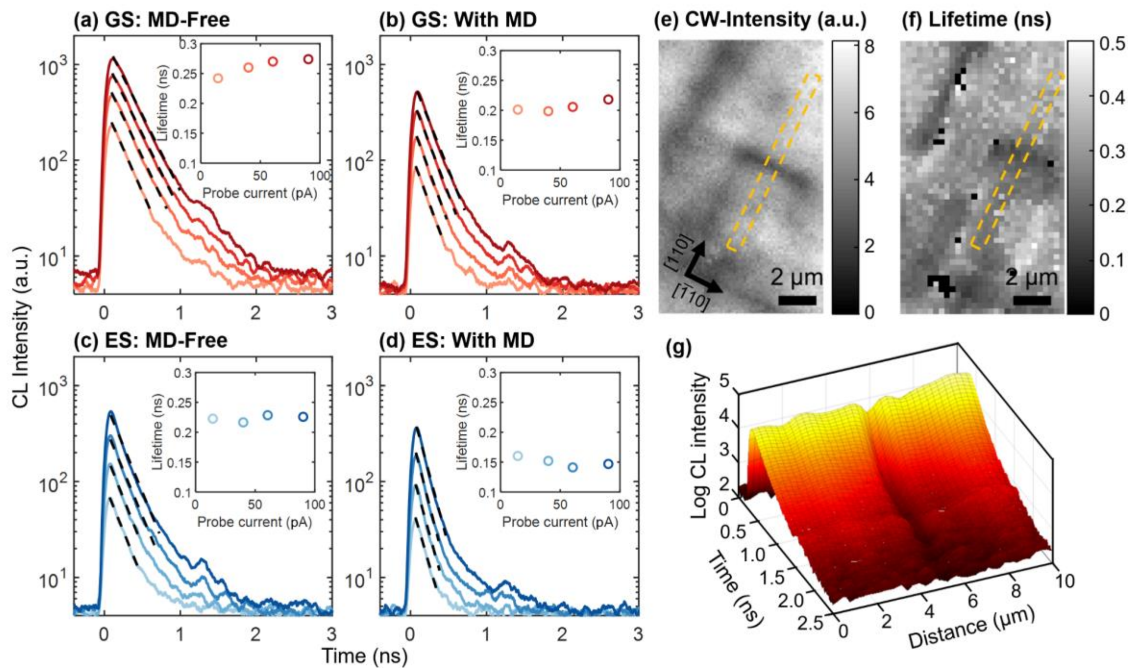

Figure 7.2. (a-d) Cathodoluminescence intensity decay traces at room temperature as a function of probe current from 15–90 pA for the ground state (a) near to and (b) away from misfit dislocations, and the excited state (c) near to and (d) away from misfit dislocations. The insets show the 1/e lifetimes for each decay trace. (e) Continuous wave cathodoluminescence intensity and (f) 1/e decay lifetime of the same region obtained using a pulsed electron source. The one-to-one correspondence between these two regions demonstrates that nonradiative recombination via dislocation-related traps limits spontaneous emission. (g) Time-position trace of cathodoluminescence intensity across a misfit dislocation (located at 5 μm) taken from the yellow dashed rectangle marked in (e) and (f). A constant width region of reduced intensity corresponding to the misfit dislocation indicates minimal lateral diffusion in the InAs QD system within the experiment window. After [210].

find the expected outcome that carriers recombine faster near the misfit dislocation, noting a 20% shorter GS recombination lifetime at the lowest probe current. The ES luminescence decays about 30% faster at the misfit dislocation. Figure 7.2e and 7.2f show a steady steady-state-excitation CL luminescence map (GS) and a corresponding pulsed-excitation carrier lifetime map obtained from each site. Comparing the two, we see a clear correlation between the CL intensity and luminescence lifetimes, typical of defect-limited recombination.

Figure 7.2g follows the TRCL decay along a trace that is orthogonal to a misfit dislocation (or group of misfit dislocations) at the center of the distance axis. When carriers are injected directly over the dislocations, nonradiative recombination reduces carrier concentration even at the shortest resolvable time scales (~100 ps, estimated from the signal rise-time), leading to a lowered initial peak intensity at t≈0 s. We may assume that minimal carrier diffusion takes place within this time, so the roughly 1 μm lateral extent of reduced intensity is the convolution of the defect size and the cross section probed by the electron beam. Carriers injected further away from the misfit dislocation should eventually diffuse towards this defect, leading to a widening of the reduced intensity valley with time. Yet, we find that the lateral extent of reduced intensity remains constant even on the longer time scale of 1–2 ns as the luminescence decays, visualized as a trench of apparent constant width in Figure 7.2g. Using this information, we obtain an upper bound for the diffusivity of carriers in this system using $L_D = \sqrt{D\tau}$, estimating an ambipolar diffusivity D of less than 40 cm^2/s for the measured recombination lifetime $\tau = 0.25$ ns in dislocation-free regions (Figure 2a). This corresponds to a diffusion length, L_D, of less than 1 μm, which is shorter than reported values for quantum-well systems in GaAs and reinforces a key mechanism behind the dislocation tolerance of InAs

QDs [166], [167]. At this time, we are unable to resolve the properties of isolated threading dislocations, but their impact appears minimal compared to misfit dislocations.

Bimberg et al. use PL to measure a spontaneous recombination lifetime, τ_r, in the GS of InAs QDs of 1.8 ns, which is independent of injection over a pulse excitation range of 0.1–100 kW/cm^2 at 77 K and only weakly temperature dependent [168]. Fiore et al measure an effective lifetime of 1.8 ns from a single InAs QD layer in an $In_{0.15}Ga_{0.85}As$ quantum well using PL at room temperature at very low excitation of 9 W/cm^2 [169]. The recombination lifetimes measured in this study, even away from dislocations, are significantly shorter; however, we cannot say conclusively whether this is a result of elevated point defect densities or excess surface recombination due to the lack of AlGaAs barriers to contain carriers that thermally excite out of the QW. Even so, it appears that the effect is modest since we observe strong and comparable contrast at dislocations in both the CL intensity and lifetime maps, which would be washed out in the presence of heavy sample-wide recombination. Regardless, potential negative impacts of point defects may be addressed through alterations to growth or additional annealing steps.

Under the constraints of dominant non-radiative recombination, the internal quantum efficiency of spontaneous emission is $\eta = \frac{\tau_{nr}}{\tau_r+\tau_{nr}} \approx \frac{\tau_{nr}}{\tau_r}$, and the recombination lifetime is $\tau = \frac{\tau_{nr}\tau_r}{\tau_{nr}+\tau_r} \approx \tau_{nr}$. Hence, the steady state luminescence of the GS is proportional to the recombination lifetime τ. This is indeed borne out in our experiments where the steady-state GS luminescence peak near misfit dislocations is darker by about 25% (see Section IV), comparable to the reduction in lifetime. We see a similar trend for the ES. These results emphasize how strongly nearby dislocations impact recombination lifetimes in QD systems despite their three-dimensional carrier confinement.

In addition to the faster decay at dislocations, there are some features present across the system that are worth noting. Figure 7.2c-d show a consistently faster decay of the ES intensity compared to the GS both near to and away from dislocations. Dissimilar decay behavior of the ES and GS arise when their occupancy is not in steady state equilibrium with each other and is expected at low temperatures [170], [171]. Nevertheless, previous work has shown that the ES and GS start to mirror each other at temperatures above 120 K (for a 60 meV GS-ES energy separation) as the states come into equilibrium with each other [170]. Although our QDs have a slightly larger ES-GS energy separation (about 70 meV), finding dissimilar decay at room temperature is unexpected. Osborne et al. report an anomalous situation in strong electrically pumped InAs dots-in-a-well structure at room temperature where they see the ESs between dots in quasi-equilibrium and the same for the GSs, but unexpectedly, within each dot the ES and GS are not in equilibrium [172]. That is, the ES and GS have different quasi-Fermi energy separations under bias even at room temperature. More work is needed to understand if a similar situation arises in our system that could lead to dissimilar ES and GS decay even at room temperature.

We also note that the GS and ES intensity decay are also slightly non-exponential both near to and away from dislocations as the intensity reduces. Several groups have reported biexponential decay (i.e., a fast and a slow component) of the ES luminescence at cryogenic temperatures [171], [173]. In our room-temperature case, it is likely that the origin of non-exponential behavior lies in nonradiative recombination in a disordered system. If dot sizes are inhomogeneous, the dots with deeper confinement lose carriers to traps at a slower rate than shallow dots, once again hinting that global equilibrium is not achieved even at room temperature in these high excitation conditions. We cannot be more definitive about this since

our probe directly follows the carrier concentration only over a small range of QD sizes (set by the instrument spectral bandwidth of 2 nm) but still probes other QD sizes indirectly through carrier thermalization and recapture.

IV. In-Situ View of Recombination-Enhanced Dislocation Glide

The process of nonradiative recombination at dislocations in InAs QDs so far assumes a fixed dislocation structure. However, this is not true in practice. Mismatch in the thermal expansion coefficient of the III-V layers and Si leads to growing tensile strain during cooldown after growth, causing the multi-micron-thick III-V layers to exceed the critical thickness for dislocation glide. While threading dislocations in the epilayers do glide to a certain extent and result in the misfit dislocations characterized earlier, they effectively freeze once temperatures drop below 300 °C, typically leaving a residual strain of about 0.15% at room temperature.

It is now well known that nonradiative carrier recombination at the dislocation core can revive glide even at room temperature via aptly termed recombination-enhanced dislocation glide [44], [57], [62]. Figure 7.3a shows a time-lapse sequence of panchromatic cathodoluminescence

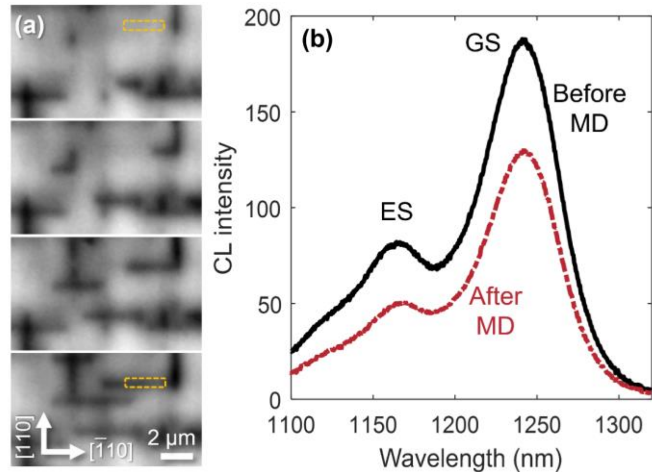

Figure 7.3. (a) Time-lapse images of recombination-enhanced dislocation glide induced by the scanning electron beam and residual strain in the III-V layer due to thermal expansion mismatch with the silicon substrate. The growing misfit dislocation contrast is captured using panchromatic cathodo-luminescence (CL) mapping. The time-lapse was generated from a 6 kV 30 nA scanning electron beam rastered over a 256 um^2 area. Each frame in the figure is separated by 30 minutes of scan time. (b) The integrated CL spectra from the yellow dashed rectangle in (a) capture the impact of a misfit dislocation growing. After [210].

(CL) images collected in plan-view, primarily imaging luminescence from the QDs. The sequence of images shows the lengthening of certain misfit dislocation segments along $\langle 110 \rangle$ directions after repeated scans. The primary electron beam generates electron-hole pairs that recombine nonradiatively at dislocations and, under the right circumstances, lengthen misfit dislocations by recombination-enhanced dislocation glide. We also see significantly more extension of misfit dislocations along the $[\bar{1}10]$ direction over the $[110]$. In undoped GaAs, α-type dislocation glide is much faster than β- and screw-type dislocations [174]. Thus, we are likely primarily seeing reverse-glide of α-type threading dislocations [175].

We probe the impact of the newly grown misfit dislocation in the region marked using the yellow-dotted box (Figure 7.3a) on QD luminescence in situ. Figure 7.3b shows luminescence spectra collected over this boxed region before and after the single misfit dislocation grows under it. We measure about a 25% decrease in GS peak luminescence and a 40% decrease in ES luminescence. This difference is reasonable as the lower steady-state carrier concentration near the dislocation implies relatively fewer ES states are filled over GS states. While the newly grown defect reduces the local emission intensity, interestingly, there is no accompanying shift in the luminescence spectrum due to the strong and local strain field of the dislocation. We think this is a consequence of the large interaction volume of the electron beam compared to the extent of the strain field: the dislocation strain field locally affects only a small number of QDs whereas carrier generation, diffusion, and nonradiative recombination affect a much large number of QDs.

V. Impact of Remote Misfit Dislocations on Quantum Dot Formation

In surveying a wider area of the sample, we find large spatial inhomogeneities in QD emission wavelength and intensity that are distinct from the more local nonradiative effects of

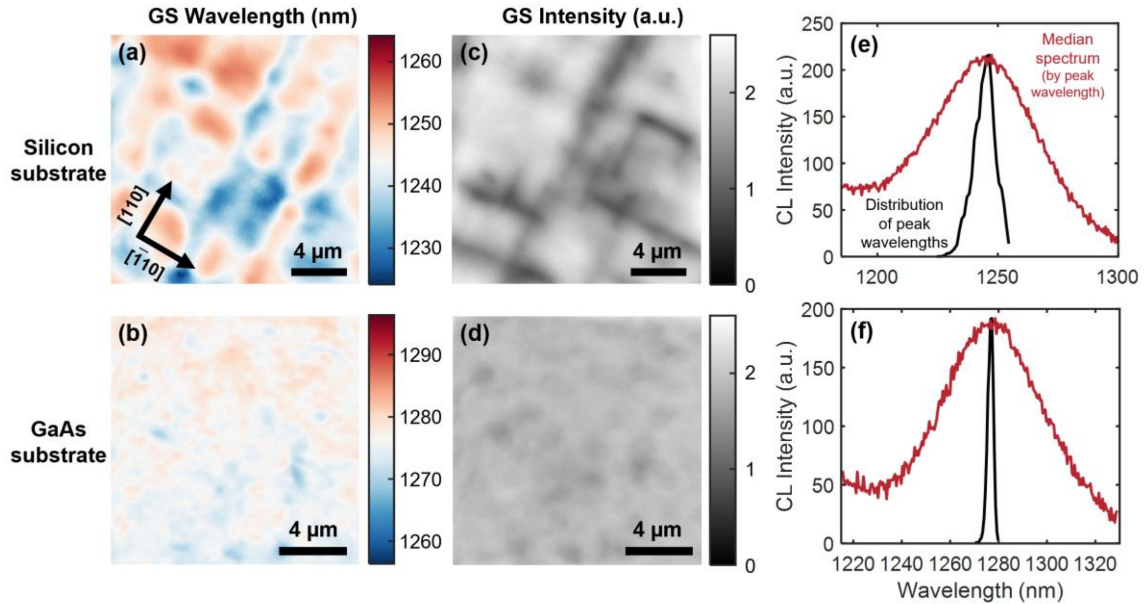

Figure 7.4. (a-b) Peak emission wavelength of the ground state for InAs QDs grown (a) on silicon and (b) on GaAs collected using steady-state cathodoluminescence hyperspectral imaging. (c-d) Total emission intensity (Gaussian fit) from the ground state (c) on silicon and (d) on GaAs. In addition to sharply reduced intensity at misfit dislocations, a crosshatching in emission intensity and emission wavelength occurs with a reduced intensity in blue-shifted regions. (e) Comparison of a typical pixel spectrum (determined as spectrum with the median GS peak wavelength) (red) to the distribution of peak wavelengths for all spectra in the CL map (black). (f) This same comparison for the sample on GaAs. Comparing (e) and (f), the GaAs sample clearly has a smaller distribution of peak wavelengths; however, both are small compared to the FWHM of the typical spectrum, so overall broadening due to the larger distribution on silicon is muted. After [210].

dislocations described thus far. Our observation is a potentially important consequence of growth on silicon as the uniformity of emission is key for high gain and reflection insensitivity [176]. Figure 7.4a shows a map of the peak GS emission wavelength, respectively, from this sample, exhibiting wide, blue-shifted wavelength bands in a crosshatch-like pattern aligned to the ⟨110⟩ directions. The bands are spaced much wider than the beam interaction cross-section (100-200 nm diameter) convolved with the carrier diffusion radius (1 μm), which points to a long-range effect rather than the typical inhomogeneous broadening from dot-to-dot variation. Each pixel in the map probes luminescence from several hundred QDs (hence already inhomogeneously broadened). A similar sample grown on a GaAs substrate does not exhibit

these wide bands of wavelength variation (Figure 7.4b), confirming their origin in growth on silicon. Along these blue-shifted bands, the GS emission intensity is also moderately reduced by 10-15% (Figure 7.4c). We reiterate that these features are not to be confused with the much more prominent dark regions stemming from the local misfit dislocation network, since, as is clear here and as shown previously in Figure 7.3b, these local misfit dislocations are not associated with a wavelength shift. For the sample on GaAs (Figure 7.4d), the GS emission intensity is much more uniform, as expected. The corresponding maps for the excited state are shown in Figure 7.5 and show comparable features to the ground state but with a clearer correspondence between blue-shifted bands and reduced emission.

We hypothesize that these darkened, blue-shifted bands arise due to the influence of the misfit dislocation network at the filters layers located 650 nm below the QDs. Via their long-range strain fields, networks of misfit dislocations are known to alter growth rates [145], [177], generate compositional variations in III-V alloy metamorphic layers, and introduce fluctuating surface step densities [178] all with a crosshatch-like pattern reflecting the structure of the misfit network. Thus, it seems likely that the surface topography variations induced by the misfit network lead to altered QD nucleation and growth dynamics, resulting in the luminescence pattern we observe here. It is also

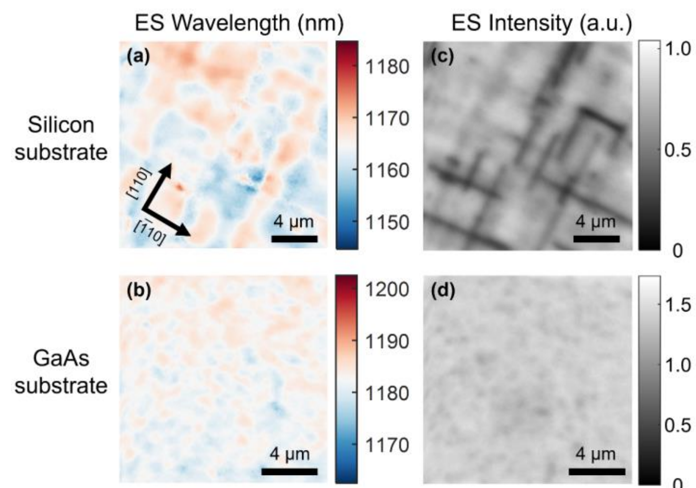

Figure 7.5. (a-b) Excited-state peak-emission wavelength cathodoluminescence map for the sample (a) on silicon and (b) on GaAs. (c-d) Corresponding excited-state cathodoluminescence intensity maps for the sample (a) on silicon and (b) on GaAs.

likely that the strain field plays a direct role during QD growth by encouraging QD growth in relative tensile stressed areas. Previous works are inconclusive on which effect is dominant, with some suggesting both mechanisms play a role [179], [180] and others suggesting it is primarily the strain-field effect alone [181]. Alternatively, the influence of the misfit dislocations may be more indirect and instead act by altering the thickness and composition of the InGaAs QW, which is known to strongly affect QD morphology and luminescence [182], [183]. However, the directional effect is not immediately clear. While increased indium content is known to red shift QD emission largely through reduced indium outdiffusion, Seravalli *et al.* demonstrate the opposite effect for QDs on metamorphic InGaAs buffers with variable strain relaxation.[184] They also show a strong impact of InGaAs underlayer composition on QD nucleation with higher indium content reducing nucleation critical thickness most likely through a mechanism described by Cullis *et al*, which details strain-driven surface enrichment of indium during InGaAs growth [185]. A similar effect could explain the correspondence between blue shifted emission regions and thicker, higher indium content QWs (shown later with APT). These regions should nucleate dots faster than elsewhere resulting in a higher density of smaller, blue-shifted QDs, possibly enhanced by local strain conditions disfavoring high indium incorporation.

One might expect that these significant spatial variations in GS emission would be easily detected by routine, spatially unresolved photoluminescence (PL) experiments as a broadened emission peak, but this is not necessarily the case. We examine the magnitude of this effect in Figure 7.4e where we compare the GS emission spectrum of a typical pixel to the distribution of all spectra peak wavelengths, weighted by peak intensity. Convolving these two approximately Gaussian distributions gives an approximation of the FWHM when sampling a

large area, as is done for typical PL measurements. Despite the significant distribution of peak wavelengths, averaging the spectra from the entire CL map only broadens the FWHM by 1.0 meV or about 2% compared to a typical single pixel FWHM of 44.3 meV. This can be understood by recalling that when convolving two Gaussians, the FWHMs combine as the root of the sum of the squares, so the broadening effect of the relatively tight distribution of peak wavelengths is greatly suppressed. Comparing to the sample grown on GaAs (Figure 7.4f), where these spatial variations are absent, the broadening is negligible with a FWHM of 38.5 meV for both the median pixel and the entire image. While the broadening is certainly larger for the sample on silicon, it is still too small to distinguish from typical sample-to-sample variation. Therefore, spectral measurements made by photoluminescence (PL), a commonly relied upon tool for assessing growth quality, will in many cases be ineffective at detecting this non-uniform crosshatched emission. Further, the associated intensity reduction can also be obscured because PL intensities are generally not comparable between samples and particularly between different substrate types due to differences in reflection at the interface. However, micro-PL mapping with a sufficiently small spot size should be capable of detecting these local wavelength and intensity variations.

Solutions to reduce crosshatch nonuniformity require either reducing adatom diffusivity [144] both during buffer layer growth and QD growth (by increasing the V/III ratio, for example) or increasing the spacing between the misfit dislocation network and the active layer [143]. During growth of our single-QD-layer sample, the nearest misfit dislocation network lies 650 nm below the QDs at the defect filter layer as shown in Figure 7.7e (remember that the other sparser misfit dislocation network just below the QDs only forms later during cooldown). Fortunately, the nearest misfit dislocation network in a typical QD laser during

growth is often about twice as distant due to a thick lower AlGaAs cladding. Indeed, we see no crosshatch-like spatial variations (Figure 7.6) in a CL map of the active layer from a laser bar. This confirms our hypothesis of long-range strain fields from the buffer as the underlying cause behind crosshatched emission wavelength. Even so, future laser designs, intended to better couple the optical mode from the III-V gain region into silicon and to reduce the likelihood of film cracking call for much thinner buffers and cladding layers [162], [163], [186]. If such lasers are directly grown on silicon, the misfit dislocation network may be close enough to the active region to result in undesirable luminescence broadening.

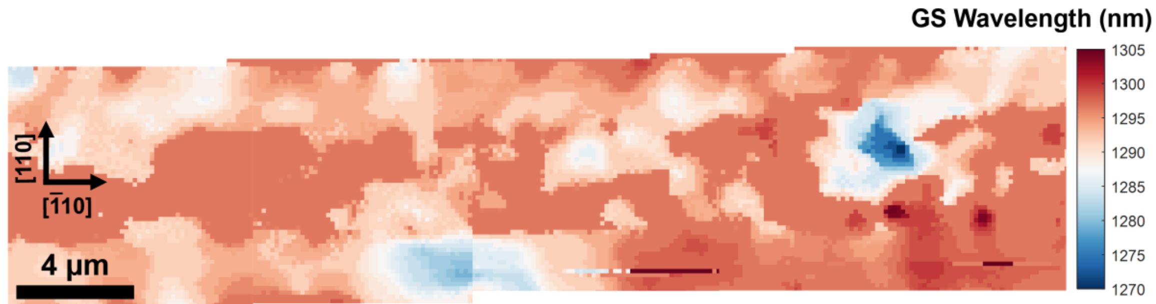

Figure 7.6. Stitched cathodoluminescence map from a five-layer QD laser grown on silicon after milling away upper cladding using a focused ion beam microscope. The spacing between the active region and uppermost defect filter layer (which hosts a misfit dislocation network) is much larger here than in the single QD structure in the main text. Consequently, the effects of extended misfit dislocation strain fields are weaker, so no distinct crosshatch pattern is visible. Even so, there are wide variations in peak emission wavelength and several strongly blue shifted regions, possibly due to hillocks formed by sessile threading dislocation clusters.

VI. Growth Modification Near Threading Dislocations

We have seen that the distant misfit dislocation network influences QD growth itself by altering the dot morphology and potentially composition. Yet, the influence of these remote misfit dislocations must be small compared to threading dislocations continuously intersecting the growth surface at a point that may not change much over time. This allows growth impacts to accumulate, in some cases forming growth mounds or hillocks due to locally accelerated

growth at spiral step edges. We locate a cluster of threading dislocations shown in Figure 7.7a using ECCI and deposit a fiducial marker to co-locate this site for CL imaging and TEM and APT extraction. Some threading dislocations appear at the center of hillocks, demonstrating their potential impact on surface morphology. Figure 7.7b shows significantly dimmer and blue-shifted emission from the hillock center compared to a region away from the hillock, with no clear GS or ES peaks identified in the former. Figure 7.7c shows that the region near the hillock with strongly blue-shifted QD emission wavelength overlaps almost exactly with the region of reduced intensity in Figure 7.7d. This correspondence likely arises as carriers more easily thermalize out of the GS of the shallower blue-shifted QDs to recombine nonradiatively at the cluster of adjacent threading dislocations. Still, we note that it is primarily the hillock and not the threading

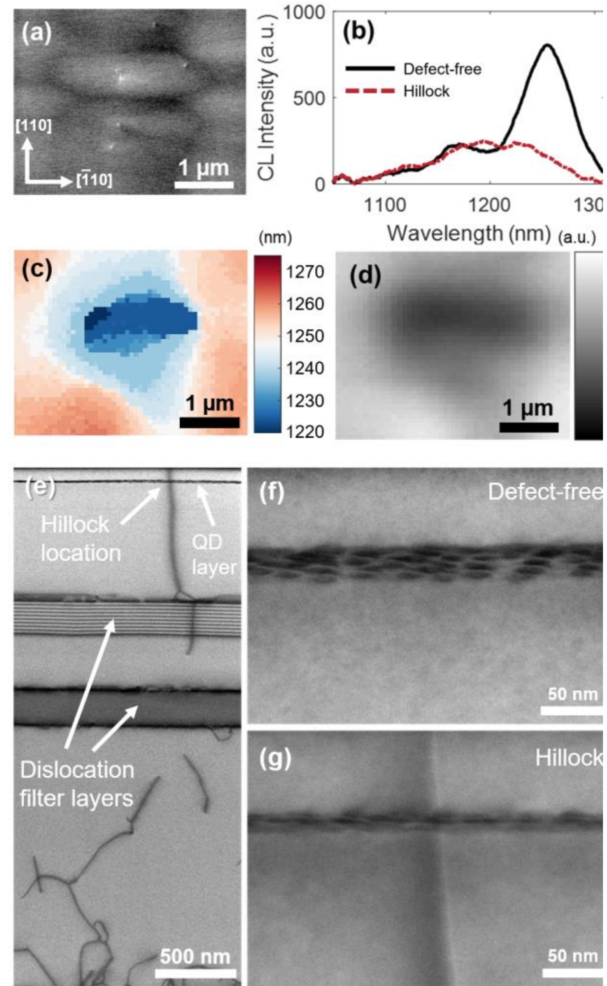

Figure 7.7. (a) Electron contrast channeling image (ECCI) of a cluster of threading dislocations forming a hillock. (b) Emission spectra from the center and away from the hillock. (c) Peak emission wavelength and (d) peak emission intensity surrounding the hillock region shown in (a). (e) Cross-sectional scanning transmission electron microscopy (STEM) of a region containing a hillock capturing a threading dislocation and a perceived local widening of the active region. High magnification view at (f) a defect-free region showing a low-angle side view of individual InAs QDs due to manual tilting of the foil and (g) the hillock containing a threading dislocation for the same foil tilt, but here, the QDs are viewed edge-on due to compensating tilt of the growth plane surrounding the hillock. After [210].

dislocations themselves that induce these changes: individual threading dislocations not associated with hillocks elsewhere in the film do not show such blue-shifted emission. In this sample, hillocks cover slightly less than 5% of the total surface, which is comparable to typical laser structures, so they are not a primary source of degraded performance. Even so, strategies to reduce their incidence should be considered such as reducing threading dislocation densities or designing buffer structures and growth sequences that minimize the number of stationary threading dislocations.

Hillocks arise due to the spiraling nature of surface steps at threading dislocations that have a screw-component to their Burgers vector. The increased density of step edges surrounding the hillock provides additional nucleation sites for QDs, which may result in a greater number of smaller (in volume), and hence bluer-emitting, QDs. We see tentative evidence for this in cross-sectional STEM of a region containing a threading dislocation with a hillock shown in Figure 7.7e. When tilted away from the zone axis, the growth plane containing the QDs at the defect-free region is viewed at an angle in projection (Figure 7.7f). When viewing the hillock region in this same tilt condition, the QD growth plane is viewed edge on (Figure 7.7g), indicating this growth plane is inclined relative to the zone axis, since this narrow slice of QDs are grown along the side of a hillock. It is also worth considering why hillocks do not feature prominently in conventional III-V lattice-mismatched (metamorphic) growth but do so in our samples. Typically, threading dislocations glide rapidly to relieve strain during growth and tend not to stay in one place long enough to yield a hillock. We speculate that a combination of near on-axis (001) substrate (limiting the density of contending steps) and sessile threading dislocations that arise at the GaAs/Si interface or by dislocation reactions result in hillocks.

To probe the structural and compositional changes caused by these hillocks in more detail, we extract tips for laser-pulsed APT from the TD-impacted hillock region and from a nominally TD-free region next to it. Note that the shallow 100 nm depth of our QDs that enables CL imaging (and ECCI), dramatically reduces the likelihood of capturing a QD in the APT tip since the conical tip diameter is very small near the top. Indeed, we see from the top-down views in Figure 7.8a that neither tip has regions of high indium concentration as would be expected from a QD, indicating that both tips probe only the InGaAs QW that encases the QDs. Nevertheless, the fluctuations are essentially consistent with those of a random alloy of InGaAs, as shown in Figure 7.9 and no evidence for phase separation or clustering is seen. On the other hand,

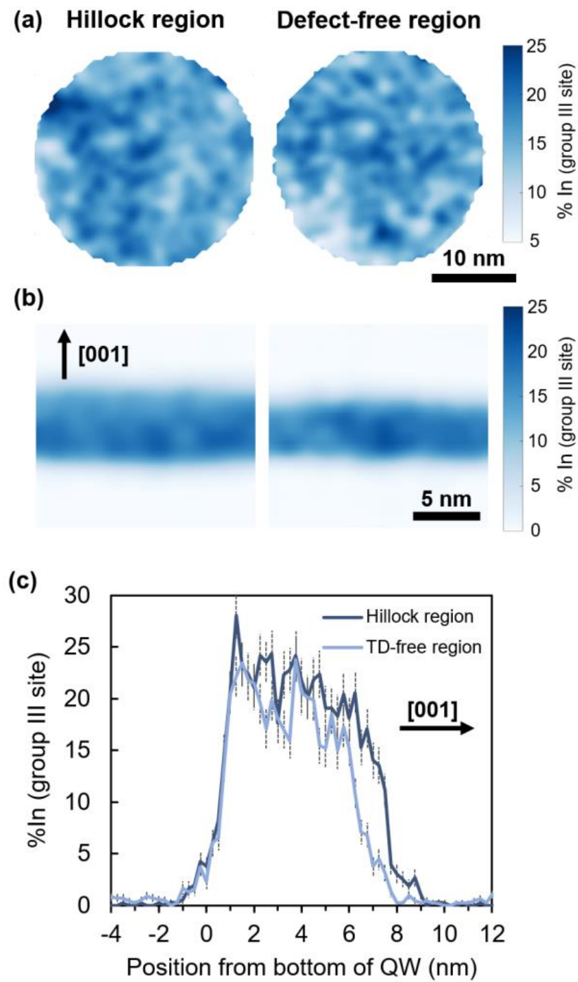

Figure 7.8. (a) Top view and (b) side view of the lateral indium composition in the nominally $In_{0.15}Ga_{0.85}As$ quantum well that surrounds the InAs quantum dots at a threading dislocation containing hillock, similar to that in Figure 7.7 (left) and at a neighboring threading dislocation (TD)-free region (right). Data collected using site-selective laser atom probe tomography informed by cathodoluminescence and electron channeling contrast imaging. No quantum dots were captured in the analysis due to the limited cross-sectional area of the APT tip possible from the 100 nm shallow structure. (c) Vertical composition trace through the quantum well showing a region of tapered but similar composition profiles for the two sites, but increased thickness for the defective region. Error bars representing one standard deviation are indicated by the dotted lines. After [210].

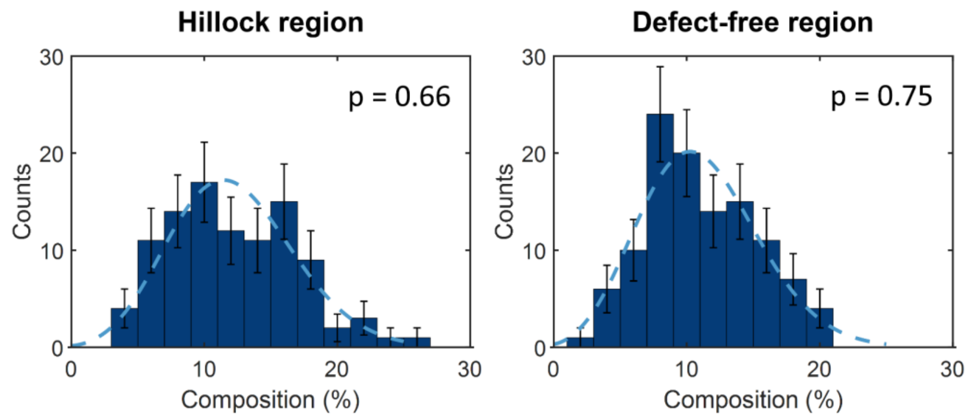

Figure 7.9. Compositional frequency distribution measured from the bottom 2 nm of the QW analyzed in the two atom probe tomography specimens, which roughly aligns with the expected location of any QDs and the wetting layer. The dashed curve is a binomial fit representing the expected compositional distribution for a random alloy. The p-values estimate the probability that the observed distributions represent a random alloy, therefore, both alloys appear to be randomly distributed with no indication of a quantum dot or partial quantum dot present in either. The bin size for composition measurements is 50 atoms.

the cross-sectional indium profiles of each tip in Figure 7.8b reveal that the QW in the defective region is significantly thicker than in the TD-free region. Collapsing these down to one-dimensional vertical profiles of indium composition, averaged laterally over the center of the tip, we see in Figure 7.8c that the QW in the hillock is about 8-9 nm thick with a tapering indium profile, contrasted with a 7 nm thick QW with a slightly lower indium composition seen in the tip from the TD-free region. Some of this taper, along with indium concentrations elevated above the expected 15% nominal value, may be explained by the dissolved InAs wetting layer (consistent with other APT [187], [188] and STEM [189] studies) that lies 2 nm above the base of the QW. However, the additional thickness of the QW is an effect of the hillock.

Reiterating that the hillock regions contain a higher density of surface steps, if the availability of steps limits the incorporation of adatoms, any asymmetry between the diffusivity of indium and gallium may lead to preferential incorporation of indium in such hillocks. The

vertical profile for the hillock region does show slightly enhanced indium incorporation, although this increased composition and growth rate could also be accounted for by strain due to the dislocation, as discussed in Section V. Without direct access to the composition or shape of the InAs QDs, we may only infer how the altered QW affects the emission spectra. In addition to easier thermalization from smaller blue-shifted QDs, a locally thicker QW may have a ground state closer in energy to the QDs and enhance carrier thermalization out of the dots. Additionally, local variations in QW composition may affect QD formation to blue-shift luminescence, as described in Section V. Taken together, these analyses demonstrate the serious impact both distant misfit dislocations and local threading dislocations can have in altering the growth of QDs and their surrounding structures, ultimately broadening their size distribution (and hence their emission spectrum) and further aggravating nonradiative recombination. Therefore, these effects must be closely considered when tuning device design to optimize performance and reliability.

Finally, we note that many of the previously observed effects are also relevant for other lattice mismatched epitaxial devices. While quantum dot devices may be of particular concern due to their highly sensitive growth conditions, other active region types can also be impacted. General factors that increase the likelihood of observable impacts are (1) a short distance between the mismatched interface with the misfit dislocation array and the active region (perhaps <1 μm), (2) a modest density of misfit dislocations at the mismatched interface so strain fields are sufficiently widely spaced to induce cross-hatch [177], and (3) growth of intermediate multi-component alloys with lattice mismatched components (e.g. InGaAs but not AlGaAs). Alternatively, other schemes of defect reduction that do not create misfit

dislocation networks, such as aspect ratio trapping (ART) or confined epitaxial lateral overgrowth (CELO), offer routes to avoid these issues entirely [190].

VII. Conclusions

With the wide-ranging potential of heterogeneously integrated material systems by direct growth, it is important to understand the microscale effect of dislocations on the final devices. We have quantified how dislocations affect spontaneous-emission luminescence in InAs QDs on silicon by facilitating defect-assisted recombination using time-resolved cathodoluminescence spectroscopy on a model InAs QD structure on silicon. We find a significantly reduced recombination lifetime for both the ground and excited states at misfit dislocations despite the three-dimensional carrier confinement of QDs. Yet, the impact of dislocations goes much beyond simple nonradiative recombination. Using hyperspectral CL imaging and atom probe tomography, we find alterations in QD and QW growth that form pockets of blue-shifted emission arising from long range misfit dislocation strain fields and short-range threading dislocation spiral growth. Both yield reduced emission homogeneity that increases susceptibility to carrier losses. This chapter shows how new characterization tools may enable a more complete understanding of the impact of dislocations on devices. InAs quantum dots, currently yielding the most reliable lasers, are now part of a series of III-V devices being synthesized on silicon spanning the visible to the mid-infrared. Indeed, these second-order dislocation impacts are relevant for most schemes involving lattice mismatched epitaxy where material uniformity is essential, both QD and non-QD based, such as for lasers, photodetectors, light-emitting diodes, single photon sources, and solar cells.

8. Gradual Degradation in InAs QD Lasers on GaAs and Si

I. Introduction

Semiconductor laser device degradation due to crystalline defects can be categorized as rapid or gradual, depending on how quickly they fail. QD materials are resistant [29] to the rapid degradation from dislocations on the 10^0–10^2 h timescales commonly observed for similar quantum well devices [20] due to the stronger lateral carrier confinement [28] and in-plane fluctuating strain fields of QDs [100]. We have found that grown-in dislocations gradually degrade unoptimized QD devices on a 10^3–10^4 h timescale at room temperature [29], and much faster at elevated temperatures of 60–80 °C [95], [191]. This failure mode has been by lessened by reducing threading dislocation density [18], [30] and later largely eliminated by introducing MD trapping layers around the active region [95], [191]. At present, there is a need to understand gradual degradation at 80 °C on the 10^5–10^6 h timescale for commercial viability. This failure mode is inherently a slow and subtle process involving evolving distributions of point defects, which themselves are difficult to directly study and identify. Researchers have previously identified a signature of this type of gradual degradation in earlier generations of quantum well and double heterostructure GaAs and AlGaAs-based devices on native substrates (i.e. not due to rapid degradation from pre-existing dislocations). They have specifically noted the appearance of small dislocation loops, believed to form due to clustering of point defects [43], [192]–[195].

In this chapter, we examine three types of InAs QD lasers epitaxially grown on silicon and GaAs substrates after extended constant current aging, using electroluminescence (EL) imaging and scanning transmission electron microscopy (STEM) to determine the source of gradual degradation. EL dimming is largely uniform along the laser ridge with no enhanced

dimming at the facets. We observe dislocation loops in the active region of aged lasers only, which we believe form from point defects generated by non-radiative-recombination-enhanced processes during aging. Based on these findings, we propose design and growth changes that may reduce gradual degradation in these devices towards a goal of 10^6 h lifetime at 80 °C.

II. Laser Aging Trends and Optical Characterization

Aging Behavior

The three types of QD lasers aged and analyzed in this work are lasers on silicon without MD trapping layers (no-TL laser), on silicon with trapping layers (TL laser), and on GaAs with no trapping layers (GaAs laser). Growth and fabrication details are described previously [95]. Figure 8.1a is a schematic of the general laser structure with the trapping layers included. The lasers on silicon (TD density = 7×10^6 cm^{-2}) were aged at 80 ºC at approximately double their initial threshold current with L-I-V measurements taken periodically at 35 ºC and 80 ºC. The GaAs laser was aged at 80 ºC and 3× initial threshold current, giving an aging current density intermediate to the two lasers on silicon. L-I data for the GaAs laser was only collected at 35 ºC, so for a fair comparison, in Figure 8.1b-8.1d, we present a sequence of 35 ºC L-I curves collected every 50 h over the course of aging (see Figure 8.2 for 80 ºC aging data for devices on silicon). Each selected device is a representative high performing device from a subset of all aged lasers, with between 4 and 11 devices tested for each group.

Unsurprisingly, the no-TL laser (Figure 8.1b) performs worst. It doubles its 80 ºC threshold current after just 2,700 h and fails to lase entirely at 80 ºC after 5,700 h (see Figure 8.2 for 80 °C L-I data). On the other hand, trapping layers significantly improve device lifetimes on silicon (Figure 8.1c) since they displace MDs that form on either side of the active region to

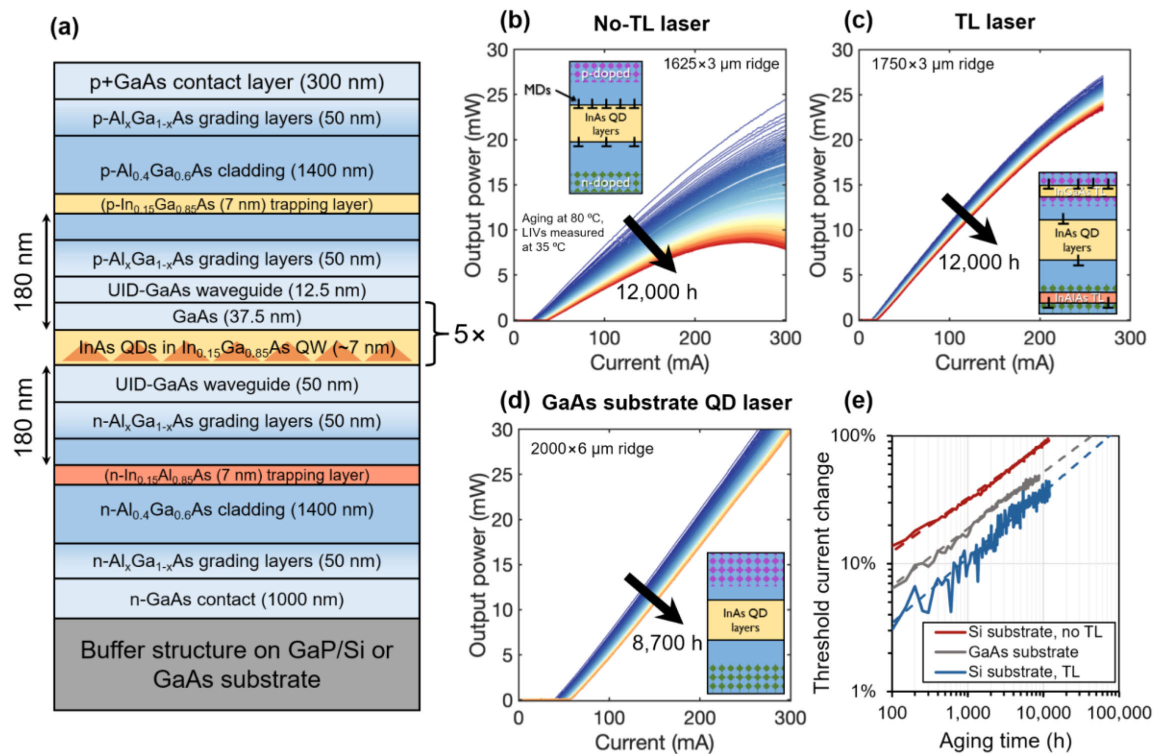

Figure 8.1. (a) Schematic of laser structure with trapping layers. (b-d) Light output vs. current (L-I) measurements over the course of aging for the three lasers: (b) on silicon without trapping layers (12,000 h), (c) on silicon with trapping layers (12,000 h), and (d) on GaAs substrate (8,700 h). (e) Laser degradation rates measured by increase in threshold current. Extrapolated lifetimes (100% increase in threshold current) are indicated with the dashed lines.

the doped cladding layers, demonstrated previously [95], [191], [196]. Nevertheless, both the TL laser (Figure 8.1c) and GaAs substrate laser (Figure 8.1d) undergo significant degradation with extrapolated lifetimes of 75,000 h and 45,000 h, respectively, shown in Figure 8.1e. This degradation occurs despite them having far fewer (TL) or no (GaAs) grown-in MDs in the active region. We cannot yet claim that TL lasers on silicon are as reliable as GaAs substrate lasers due to the different laser structures and aging conditions employed.

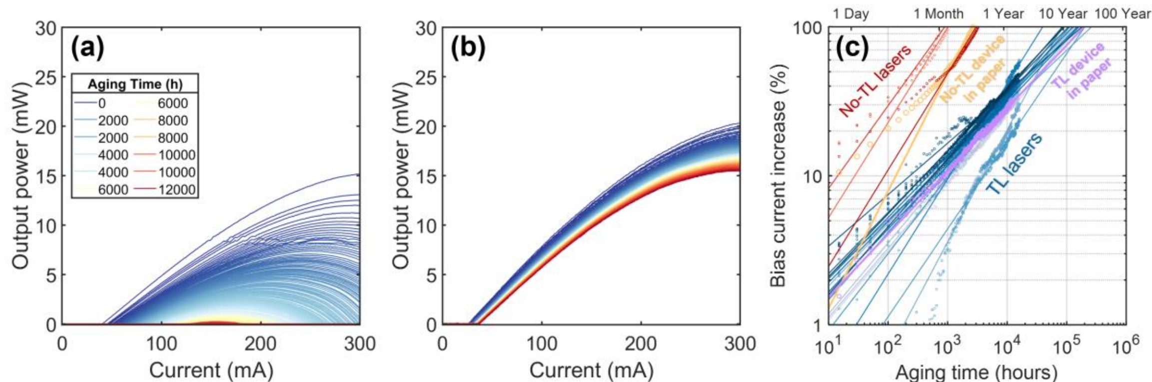

Figure 8.2. 80 °C light output (single-facet) vs. current (L-I) data for (a) no-TL and (b) TL laser on silicon. (c) Plot of the increase in bias current required for 2 mW of output power (single-facet) for all no-TL and TL lasers from their 80 °C L-I measurements. The devices selected for characterization in the main text are indicated with separate colors. All TL lasers perform substantially better than even the highest performing no-TL lasers. Devices on GaAs are excluded from these plots because, though they were also aged at 80 °C, L-I measurements were only taken at 35 °C.

Electroluminescence

To determine the source of this degradation, the lasers were unmounted and their back surfaces cleaned to enable backside EL imaging. Figure 8.3a-d shows EL from the aged no-TL and TL lasers and comparable unaged lasers imaged using an InGaAs camera (Hamamatsu). Both the aged and unaged devices show significant variation in intensity along their lengths primarily due to fabrication inhomogeneities and MDs near the active region (non-trapped) that are unrelated to aging. Both aged devices are much dimmer, however, with double the pump current required to produce comparably bright images. This is summarized in Figure 8.3e where the equalized EL intensities averaged along the ridges are plotted, adjusting for different pump currents by assuming a linear relation with EL intensity. We caution against comparing intensities between the TL and no-TL sets, however, since differing substrate thickness and backside roughness changes the relative intensities.

Higher magnification EL insets in Figure 8.3a-d (solid boxes) show similar densities of dark line defects for both aged and unaged devices, but their contrast is stronger in the aged devices, indicating localized degradation at these defects. We note, though, that even regions unaffected by these defects are still significantly dimmer (after accounting for the higher pump current), i.e., the laser is also deteriorating homogenously. By comparing TL and GaAs laser aging behavior, it is this homogenous dimming component that appears to contribute more to degradation than the line defects, at least for the TL laser. The aged no-TL laser curiously appears only to have a slightly higher density of dark line defects than the aged TL laser, though with darker contrast due to the harsher aging condition. This may be misleading given the

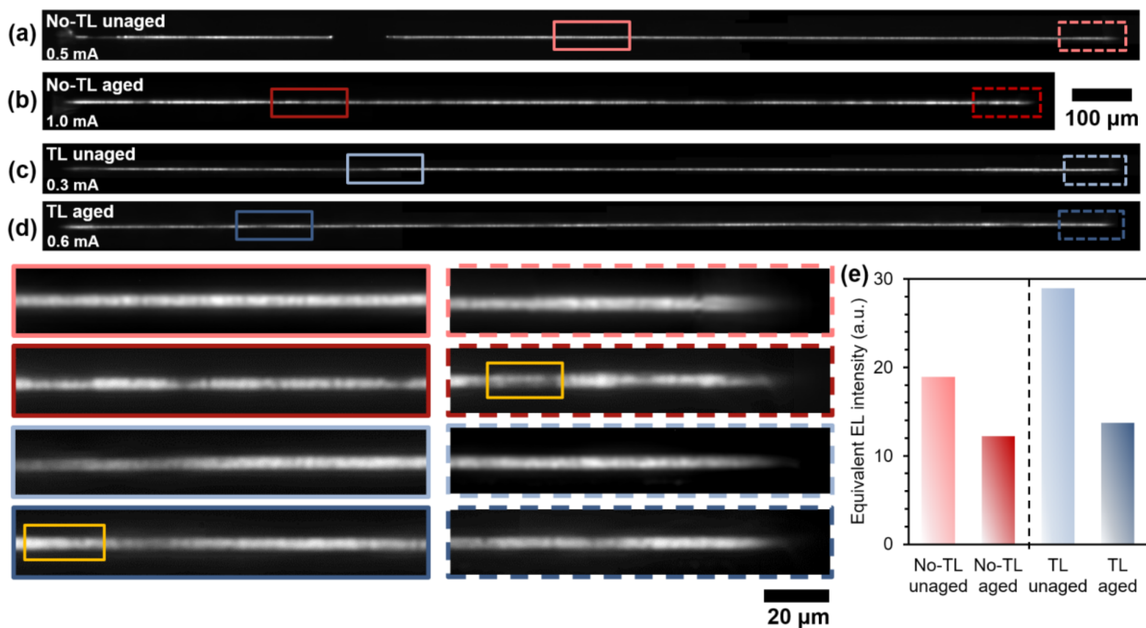

Figure 8.3. (a) Electroluminescence (EL) imaging of an unaged no-TL laser comparable in initial performance to the aged no-TL laser shown in (b). The long dark section in (a) is due to partially detached contact metal. The unaged and aged TL lasers are shown in (c) and (d), respectively. Pump current is adjusted to produce comparable brightness for each device. Magnified inset images along the ridge (solid boxes) show no notable change in density of dark line defects, but they do appear darker after aging. Degradation at the facet (dashed boxes) is negligible. Yellow solid boxes mark the regions extracted for TEM analysis. (e) Equivalent EL intensity, i.e. adjusted for pump current, averaged along each laser shows strong dimming of the aged devices. The dark segment in (a) is excluded from the averaging.

limited resolution of EL and the small 3 μm ridge width, which makes distinguishing dark line defects from dark spot defects difficult. Facet degradation appears negligible as evidenced by the magnified facet EL images in Figure 8.3a-d (dashed box inset) with similar contrast profiles. No EL was collected from the aged GaAs laser due to a short circuit forming during post-aging processing, but an unaged neighboring device shows no dark line defects (i.e., no grown-in dislocations), so degradation is expected to be uniform.

III. Microstructural Characterization

Plan-view foils were extracted from the aged lasers using standard focused ion beam techniques and imaged by STEM at 200 kV (ThermoFisher Scientific, Talos), shown in Figure 8.4a-c. The extracted locations for the TL and no-TL lasers are marked with yellow boxes in Figure 8.3b and 8.3d magnified insets. Serpentine MD segments result from previously straight dislocation segment undergoing recombination-enhanced dislocation climb by interaction with point defects [100]. The extent of the meander away from the original position is directly related to the number of point defects involved, a point we will return to. The correspondence between the MDs in Figure 8.4 and EL dark lines in Figure 8.3 is not exact as there are many more MDs than dark lines. This can be explained by recognizing that the p-modulation doping of the active region shifts the depletion region toward the n side, which will reduce non-radiative recombination and hence EL contrast of MDs on the p side. MDs on the n side may also be more potent non-radiative recombination centers due to their core chemistry [197], [198]. For example, there is good correspondence between the dark horizontal line in EL that occupies most of the yellow box in Figure 8.3b (no-TL inset) and the heavily climbed MD in Figure 8.4a (yellow arrow), which is determined to be on the n side through tilt sequence imaging. While all MDs in the no-TL laser experience climb, only a small fraction of them do

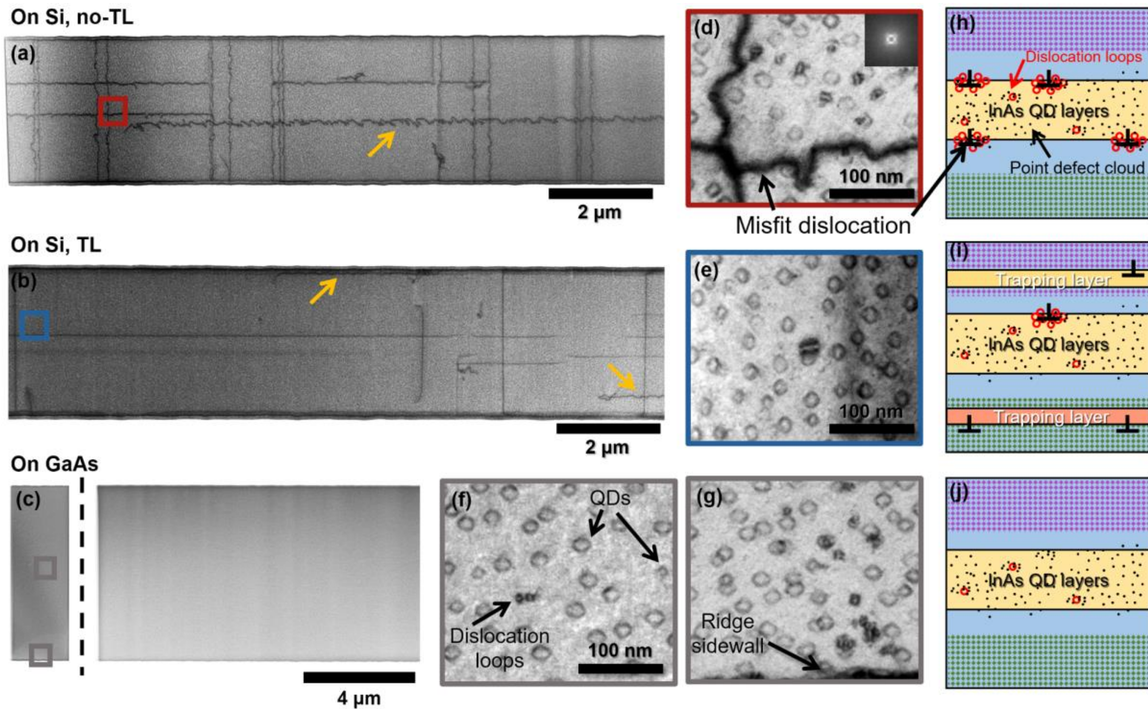

Figure 8.4. Plan-view scanning transmission electron microscopy (STEM) of the three aged lasers. (a) Section of the no-TL laser containing all 5 QD layers. (b) Section of the TL laser containing all QD layers and both TLs. Climbed dislocations, which have escaped the TLs, are marked with yellow arrows. (c) Section of the GaAs laser containing all QD layers (right) and a thinned section with adjusted contrast (left). After thinning, many dislocation loops are visible near the climbed MDs in the (d) no-TL laser, while the (e) TL laser and (f) GaAs lasers contain typically sparser dislocation loop populations. (g) An elevated loop density near the ridge sidewall. (h-j) Schematics of dislocation loops and the invisible point defects in the (h) no TL, (i) TL, and (j) GaAs laser. All images are collected in the [001] zone axis condition.

so in the TL laser (Figure 8.4b, yellow arrows). No MDs or TDs were observed in the GaAs laser (Figure 8.4c), as expected. In summary, MD climb is responsible for the degradation of the no-TL sample. However, the climb of pre-existing dislocations does not explain the gradual degradation observed in the TL laser nor, trivially, for the GaAs laser.

We look for clearer signatures of degradation in the microstructure by thinning each foil further, such that only 1-3 QD layers nearest the p-doped side remain. In Figure 8.4d, we find a large population of dislocation loops in the no-TL laser ranging in size from 5 to 20 nm that cluster around certain regions of climbed MDs (up to 150 nm from the dislocation). The local

dislocation loop density is approximately 10^{10} cm^{-2} near this dislocation. But looking widely, the correspondence between loop clusters and significantly climbed MD sections is tenuous. Loops are, however, about twice as common around heavily climbed MDs on the n-side of the laser compared to the moderately climbed p-side MDs. The TL and GaAs lasers, despite the partial or complete absence of dislocations near the active region, still contain dislocation loops, shown in Figure 8.4e and Figure 8.4f and 8.4g, respectively, with a density on the order of 10^8–10^9 cm^{-2} integrated over the active region thickness. The arrangement of MDs, dislocation loops and expected point defects for each device is shown schematically in Figure 8.4h-j.

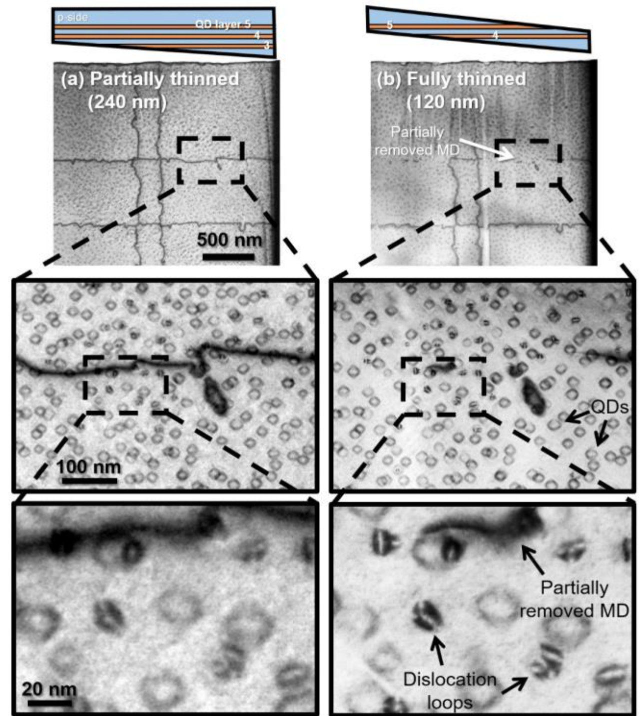

Figure 8.5. (a) [001]-zone plan-view BF STEM of the partially thinned sample from the no-TL laser. Magnified insets show a dislocation loop cluster near a climbed MD. The inset diagram above is a side profile showing approximately which of the five QD layers remain in the thinned sample. (b) The same sample thinned further to partially remove the MD on the p side of the laser, but not the QDs themselves. Notably, the dislocation loops that form near this MD all remain behind indicating the loops are centered not around the MD but around the QDs themselves.

In the GaAs laser, dislocation loops are especially common within 50 nm of the edge of the deeply etched ridge. Figure 8.4g shows an exceptional case of this where a heightened loop density extends over 300 nm from the sidewall, but the reason for this is not clear as the sidewall does not appear visibly different from other locations. This preferential loop formation

near the sidewalls is not so apparent in the lasers on silicon due to an improved etching and passivation process. The loops in the GaAs laser are also notably smaller than in either laser on silicon, possibly a consequence of the shorter aging time.

We established that dislocation loops are closely associated with climbed MDs. These untrapped MDs lie just above the upper QD layer or just below the lower layer, but their associated loops preferentially form near the QD layer, rather that forming uniformly above and below the MD. This is demonstrated in Figure 8.5. After thinning the no-TL sample just enough to begin removing the upper climbed MD, all loops near to that MD remain behind, indicating they sit lower in the sample. QDs might act as nucleation sites for loop formation, but while some loops appear to form directly over a QD, many others lie in the matrix in-between. We can additionally determine approximately where the loops lie in the vertical plane relative to the climbed MDs by imaging the no-TL sample across a range of tilt angles. Shown in Figure 8.6, all loops associated with climbed MDs remain near the plane of the MD. This may be because recombination enhanced diffusion [199] is favored laterally through the QW where carrier concentrations are highest. We have also observed loops unassociated with MDs that are distributed throughout the active region.

The dislocation loops have a similar appearance and orientation across all three aged samples and likely have a common structure. To determine their Burgers vector, we image the no-TL sample for its high loop density in several diffraction conditions to identify loop invisibility conditions. Dislocation loops in GaAs-based materials have either $\frac{a}{2}\langle 110\rangle$ or $\frac{a}{3}\langle 111\rangle$ family of Burgers vectors, so we limit our search to these. Imaging with typical two-beam conditions (**g**=220 or **g**=400) gives strong quantum-dot contrast often with a similar appearance to dislocation loops, making invisibility determination difficult. To combat this,

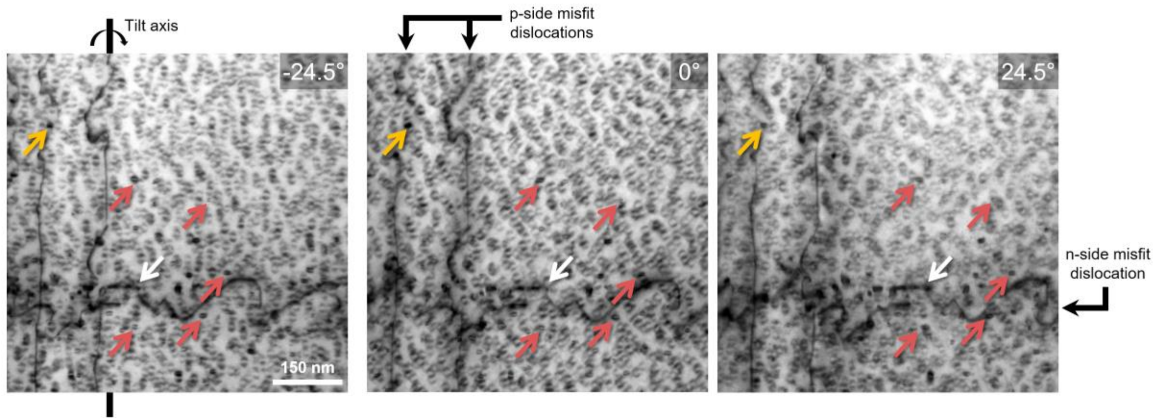

Figure 8.6. A tilt series of BF STEM images in the higher-order $3g_{220}$ diffraction condition. The images are aligned to keep the vertical p-side misfit dislocations stationary. The heavily climbed horizontal misfit dislocation appears to translate rightward relative to the stationary vertical misfits, marked by the white arrow, indicating it is on the n side of the active region. The background contrast is heavily influenced by the 5 QD layers. Dislocation loops are still visible despite this, marked by their sharp, elongated double-lobed dark contrast whereas the QD contrast is fainter, less sharp, and more circular. The large majority of dislocation loops in this location are approximately in the plane of the horizontal n-side misfit, shown by the several loops marked by red arrows that move in step with the horizontal misfit. There is only one clear dislocation loop on the p side, marked by the yellow arrow. Elsewhere, dislocation loops have also been observed at intermediate QD layers, but these are likely unassociated with misfit dislocation climb, similar to the loops observed in the TL and GaAs lasers.

we image using higher-order diffraction vectors [200], $3\mathbf{g}_{220}$ ($\mathbf{g}$=660) and $2\mathbf{g}_{400}$ ($\mathbf{g}$=800), which provide reasonably clear images of dislocation loops even through all five QD layers. Figure 8.7 presents a systematic sweep over higher-order $\mathbf{g}_{220}$ diffraction vectors, demonstrating how the $3\mathbf{g}_{220}$ optimally isolates loop contrast from QD contrast without reducing total contrast too severely. In Figure 8.8, two dislocation loops are tracked across four diffraction conditions with a red and a yellow arrow. The translucent arrows in Figure 8.7a and 8.7b indicate the loop is invisible. Both loops are visible in the two $2\mathbf{g}_{400}$ conditions (Figure 8.7c-d). Based on predicted invisibility (see Table S1), this strongly suggests a Burgers vectors of $\frac{a}{3}\langle 111\rangle$ type, i.e. a Frank dislocation loop. This assignment is reasonable since the loop diameter is still small and the well-known unfaulting reaction to form a perfect $\frac{a}{2}\langle 110\rangle$ loop is still not energetically favorable [201].

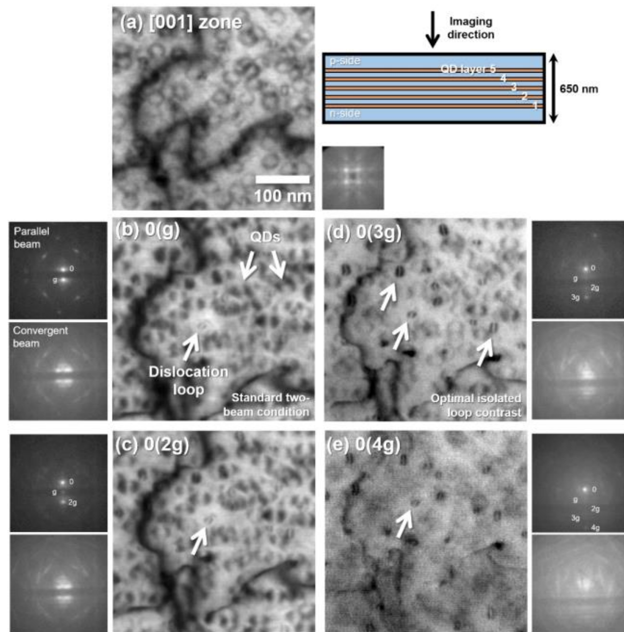

Figure 8.7. Comparison of BF STEM diffraction conditions on dislocation loop visibility and contrast. (a) On-zone imaging gives balanced contrast with dislocation loops only faintly visible amid the 5 QD layers. (b) Tilting to a standard g=220 two-beam condition produces strong misfit-dislocation contrast and double-lobed QD contrast, making dislocation loops very difficult to see with their weaker contrast and smaller size. (c) Strongly exciting $2g_{220}$ slightly reduces QD contrast making dislocation loops more visible. (d) This trend continues for $3g_{220}$ where now dislocation loop contrast is relatively stronger than QD contrast. (e) In the $4g_{220}$ condition total contrast becomes very weak, though contrast separation is still further enhanced. This higher-order diffraction vector imaging technique is somewhat analogous to weak-beam dark field imaging in TEM, but STEM allows imaging through much thicker samples with less background contrast variation. For optimal contrast isolation, it is necessary to avoid exciting nearby diffraction conditions as much as possible since these strengthen QD contrast. Using the diffracted signal intensity for imaging gives comparable contrast isolation but with a much weaker signal.

IV. Dislocation Loop Formation and Possible Mitigations

Frank dislocations loops have been seen in degraded GaAs-based LEDs and lasers. Ueda et al. [194], [202], [203] use an inside-outside TEM contrast method and characterize these loops as having an interstitial character, i.e., they contain an additional set of {111} planes of both Ga and As atoms, preserving lattice polarity. Frank dislocation loops form by the coalescence of point defects. The Burgers vector $\frac{a}{3}\langle 111\rangle$ is normal to the plane of the loop, and the loop grows laterally by climb, attaching atoms to the boundary of the additional plane. Ueda specifically notes such interstitial dislocation loops form not only randomly in the bulk of the device, but also in large

numbers near climbed segments of pre-existing dislocations, similar to our observation for the no-TL sample and in previous work [100]. While it is tempting to suggest that the dislocation loops must be a consequence of excess point defects generated from the climb of the pre-existing dislocations that precipitate out, it is noteworthy that pre-existing straight segments of dislocations (such as threading or misfit type with 60° character) in GaAs devices also climb by attaching atoms to the core. Thus, Ueda clearly sees a common driving force behind dislocation climb in GaAs, irrespective of whether the dislocation is in the form of a loop or a straight segment. We had previously suggested that the cluster of dislocation loops could be vacancy type in QD lasers due to excess vacancy generation following atom attachment to the MDs in the no-TL laser [100], however seeing them also in the TL and GaAs samples leads us to conclude similarly to Ueda et al. that they are likely of interstitial character in all samples. The dislocation loops in our samples are presently too small for unambiguous assignment via inside-outside contrast, particularly amid competing QD strain contrast. This does leave open the question of why dislocation loops cluster near climbing MDs in the no-TL sample.

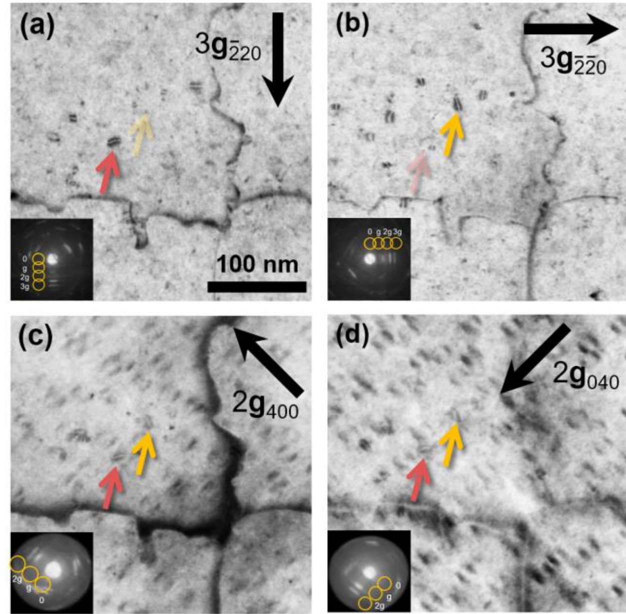

Figure 8.8. Invisibility conditions for dislocation loops. (a) $3\mathbf{g}_{220}$ and (b) $3\mathbf{g}_{2\bar{2}0}$ images highlight two loops with alternating invisibility. In each, the translucent arrow indicates an invisible loop. In the (c) $2\mathbf{g}_{400}$ and (d) $2\mathbf{g}_{040}$ images, both loops are visible (dark arrows).

Regardless of the exact nature of the point defects emitted or absorbed that form the loops, we find a net imbalance of point defects at dislocations of the no-TL sample. A conservative

estimate of the local point defect density involved in dislocation climb in the vicinity of a climbed MD is 3×10^{19} cm^{-3}. We can assess this from the area swept by the MD as it climbs and then assume that point defects necessary to accommodate this climb laterally diffuse a radius of 500 nm to or from the dislocation core but remain confined near the QW nearest to the MD. The density of point defects is greater if the diffusion length is shorter. The minimum point defect density needed to form the dislocation loops near the misfit dislocations observed here is on the order of 10^{18} cm^{-2}, assuming a local loop density of 10^{10} cm^{-2}, a 5-10 nm average loop diameter, and a similar diffusion behavior as before. Thus, it appears that most of the point defects stay dissolved in the bulk and the visible dislocation loops are simply the tip of the iceberg in terms of nonradiative defects present. Experiments using deep-level transient spectroscopy (DLTS) indeed see an increase in electrical activity of point defects upon aging quantum well lasers, suggesting that point defects are generated during the experiment [194]; however, there has not yet been a conclusive assignment to which defect is increasing in number.

To improve reliability, we suggest several strategies for future devices. First, changing the fabrication design from a deep-etch ridge to a shallow-etch ridge, where the active region remains unetched near the mesa, will improve initial performance by reducing non-radiative recombination at the sidewalls and removing crystal damage and the free surface, which can act as potent sources of point defects, as Figure 8.3g demonstrates. Second, since reducing the starting point defect density may be critical to long lifetimes, modifications to growth and to post-growth processing should be investigated, including post-growth annealing and potentially altering group-V/III flux ratios when growing QDs and the surrounding layers. Finally, dark line defects are not entirely absent from the TL laser and further performance

benefits should be available by optimizing trapping layer design to further reduce the small fraction of misfits that escape the trapping layer and get into the active region [94], [191].

V. Conclusions

We have shown that gradual degradation in InAs quantum dot lasers is accompanied by the formation of dislocation loops, similar to what has previously been observed in conventional lasers with GaAs and AlGaAs double heterostructures and quantum wells. While the loops themselves are likely nonradiative recombination centers, we believe the wider elevated background of point defects is the primary source of degradation. This degradation may be reduced by altering growth parameters and post-growth thermal processing, modifying laser fabrication design, and improving trapping layer performance. Further progress, however, requires a more fundamental understanding of these degradation mechanisms, requiring techniques such as DLTS to pinpoint the evolving point defect species. This is expanded upon in the following chapter.

9. Summary and Future Directions

I. Summary of Findings

This thesis explores the continued development of reliable InAs quantum dot lasers for silicon photonics by investigating the root causes of degradation and implementing solutions where possible. The first experiments discussed in Chapter 3 involved studying the dynamics of dislocations in simplified model structures of a portion of a laser. This was a natural extension of previous work with comparable structures by Callahan, Haidet, et al. [57], which demonstrated the recombination-enhanced glide of dislocations under residual thermal tensile stress. The initial motivation for conducting this follow-on experiment with CL rather than ECCI was to probe the optical effects of dislocations and determine whether their non-radiative impacts are affected by their motion, e.g. a Cottrell atmosphere of non-radiative defect clusters surrounding a threading dislocation might be left behind after the dislocation glides away, or whether their non-radiative strength influences glide velocity, since more non-radiative recombination might further lower the energy barrier to dislocation glide. These, however, were largely null results. The main finding was the strong dependence of dislocation glide velocity on indium alloying content, summarized in Figure 9.1. The mechanism behind this

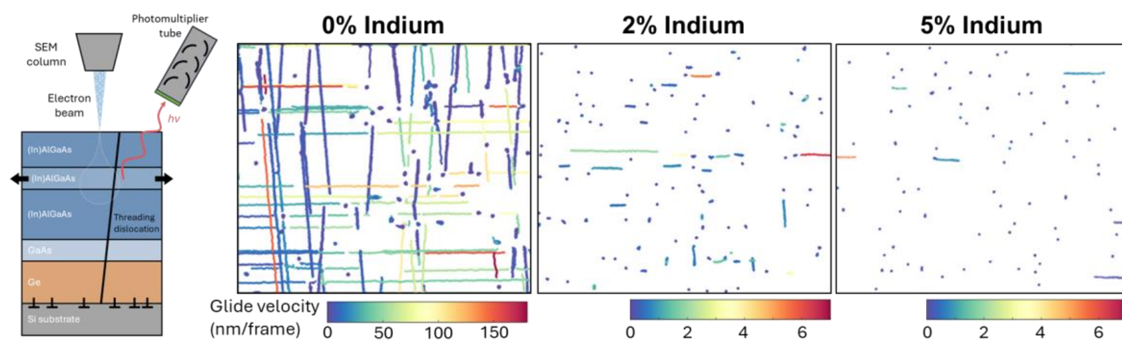

Figure 9.1. Indium alloying reduces dislocation glide velocities and reduces the total fraction of mobile dislocations.

effect was determined to be alloy hardening where the larger indium atoms (compared to the similarly sized aluminum or gallium atoms) slow dislocation kink migration. Many fewer dislocations also glide in the indium alloyed structures, which is attributed larger scale random indium composition fluctuations which generate a variable lateral strain field that cannot be overcome by the weak thermal tensile stress.

The issue with misfit dislocations forming in the active region of QD lasers, detailed in Chapter 4, had been known for some time at this point, see [29] and [76], and was attributed to the strained active region being grown above critical thickness. However, Matthews-Blakeslee [127] critical thickness calculations do not predict that relaxation via existing threading dislocations should be energetically unfavorable. Even more conclusively, these misfit dislocations were still appearing in simplified model structures with only a single QD layer investigated by CL by Selvidge et al. [28]. This pointed to an alternative misfit dislocation formation mechanism, which in light the previously discussed results on indium pinning, suggested that it was the threading dislocation segment in the neighboring GaAs and AlGaAs layers that was relaxing. After relaxing the initial compressive stress relative to the silicon substrate, these layers are nominally unstressed, so it must be the tensile stress that develops during cooldown that drives to misfit dislocation formation. This possibility was posited by Selvidge, et al. at the time, but the theory was not yet fully developed and other mechanisms were still under consideration. As this understanding developed, laser structures alloyed throughout with indium were attempted, but growth quality was poor and threading dislocation densities were high. The remedy instead was to insert thin strained layers of similar composition and thickness to the InGaAs QW encasing the QDs to extend the pinning effect

in the active region to these remote layers and inhibit all threading dislocation glide in between. This effectively displaces the formation of misfit dislocation to the outer sides of the trapping layers. This significantly boosts the performance of lasers with trapping layers, as summarized in Figure 9.2.

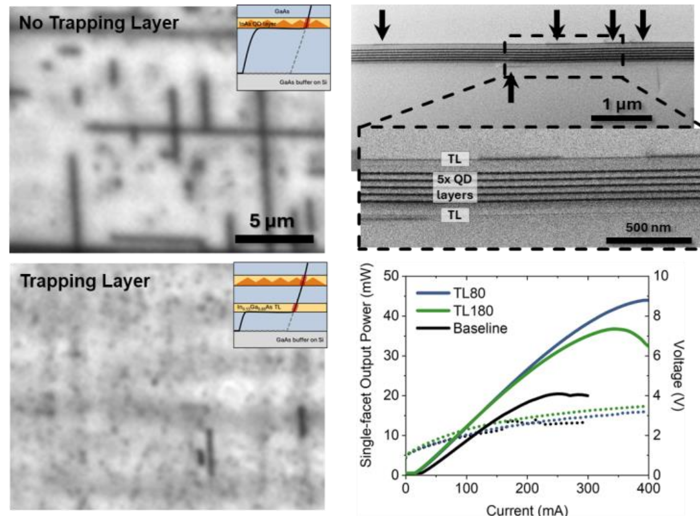

Figure 9.2. Summary of reduced misfit densities in model structures and lasers using trapping layers and the resulting improved laser performance.

Reliability of lasers with trapping layers was investigated in a follow-up study, discussed in Chapter 5. A total of 14 devices were aged with and without trapping layers at 60 °C. Degradation of the trapping layer devices during aging is approximately 10× slower, in terms of extrapolated lifetimes, when comparing the best laser without trapping layers and a typical laser with trapping layers. Plan-view STEM reveals that misfit dislocations held at the trapping layers show no signs of climb unlike those lying directly above and below the active region. Dislocation climb and the evolution of point defect populations are primarily responsible for degradation and failure of InAs QD lasers and for similar quantum well lasers grown on silicon. Comparing two trapping layer locations, it appears that spacing them farther from the active region improves reliability even though initial performance is generally worse and a smaller fraction of misfit dislocation is trapped. This could be due to misfit dislocations in the TL80 laser lying too close to the edge of the doped layers and hence capturing small numbers of carriers during aging and climbing slowly. A firm conclusion is difficult though, given the

small number of devices aged and because these laser fabrication runs had issues with voids forming in the upper cladding layers that would sometimes extend down through the active region. The severity of these voids varies between devices and likely also varies between the laser groups. Assessing the overall severity of voids in a fabrication run is challenging though since examining the cleaved facets only provides a view at one point along each of the lasers. A second study by Shang, et al. examines laser reliability at 80 °C for a much larger set of 38 total devices with trapping layers inserted only 180 nm from the active region. These devices incorporated a low threading dislocation density buffer structure which led to cracking for some of the devices during cooldown as there were too few dislocations available to help relieve strain. Still, these are the highest reliability devices we have tested to date, with extrapolated lifetimes consistently in the range of 10 to 20 years, as shown in Figure 9.3.

The basic concept of using a strained layer to block the passage of misfit dislocations was also applied to an alternative type of heterogeneous integration scheme, investigated in Chapter

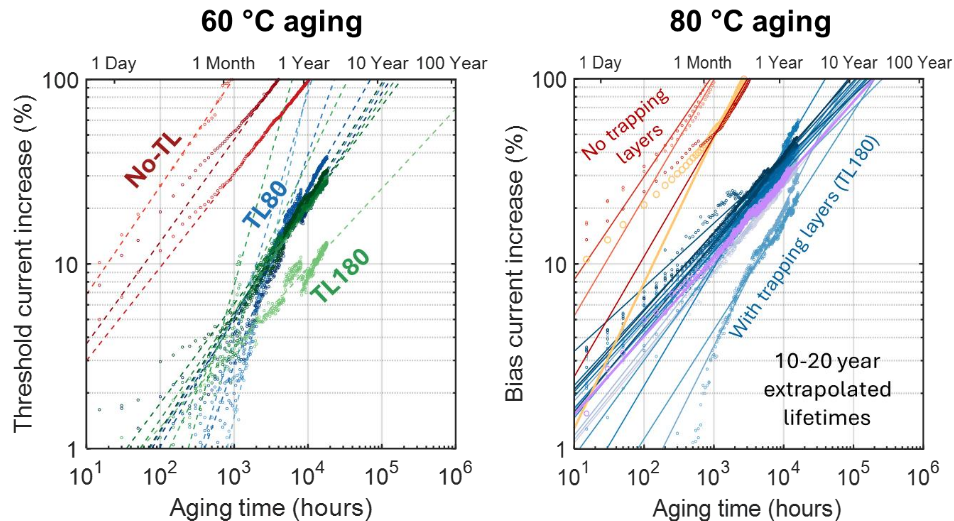

Figure 9.3. Comparison of aging behavior after approximately 16,000 h at 60 °C and after 14,000 h at 80 °C for lasers with and without trapping layers. The exceptional extrapolated lifetime for the single 60 °C TL180 device is an artifact of slower initial degradation. 80 °C aging bias current increase is measured as the current required to maintain 2 mW of output power. The lasers are still aged at a fixed constant current.

6. In this scheme, a thin template of homoepitaxial GaAs is bonded to silicon or SOI before removing the GaAs substrate. A laser structure can then be grown on top of this nominally defect free template. However, the bonded film is compressively stressed at growth temperature due to thermal strain and tends to relax, forming significant densities of threading dislocations in the process. Inserting strained trapping layers reduce these defect densities reaching the surface or the active region of a hypothetical device by 10-20×. Even better performance might be achievable using a combination of compressive and tensile strained trapping layers, but such tensile strained layers are not possible with the source materials available on the MBE growth chambers, both lacking a phosphorous source.

The further impacts of dislocation on the QD luminescence and growth morphology were explored in Chapter 7. Time-resolved CL measurements reveal relatively short recombination lifetimes for the QDs in the same model structure studied in Chapter 3. While not conclusive, this may be a result of sub-optimal growth parameters yielding elevated densities of point defects. Spectrally resolved CL measurements show how QD emission wavelength varies in a cross-hatch pattern similar to that seen in ECCI due to underlying misfit dislocation arrays. This pattern is not observed in a laser, which is attributed to the larger distance between the dislocation filter layers and the QD layers. Even so, thinner cladding layers have recently been introduced to reduce the likelihood of cracking during post-growth cooldown, so this exacerbated inhomogeneity may be translated to these thinner laser structures. Finally, hillocks containing clusters of threading dislocations are shown to strongly blue shift QD emission in their vicinity in addition to the expected reduced luminescence. This may be due to the surface morphology of the hillock, where the increased density of surface steps provides more

nucleation sites for QDs, which then locally form with a higher density and an overall smaller size.

Finally, trapping layers do not entirely solve the issue with limited reliability of InAs QD lasers on silicon. Even QD lasers on native GaAs have challenges with degradation on comparable time scales. The source of this gradual degradation was explored in Chapter 8. Backside electroluminescence imaging shows that lasers with and without trapping layers degrade across their entire device length, with no regions of concentrated such as at the facets. Plan-view TEM reveals the presence of dislocation loops in high densities surrounding climbed misfit dislocations, as has been observed before [29], [100], but also in lower densities away from occasional climbed misfit dislocation in trapping layer lasers and lasers on GaAs. These form from the coalescence of point defects in the lattice which are likely being generated through recombination enhanced mechanisms in an altered energetic landscape due to elevated electron and hole densities. It is not clear if these generation processes can be impeded, but it is clear that accelerated degradation occurs surrounding existing non-radiative defects such as misfit dislocations. Therefore, minimizing initial sources of non-radiative recombination—dislocations and initial point defects alike—should be effective in slowing these degradation

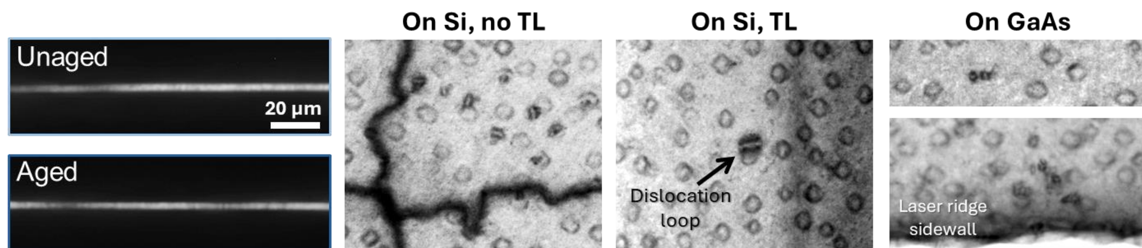

Figure 9.4. Electroluminescence in an unaged and a separate aged laser without trapping layers and plan-view STEM of the three laser types all with some density of dislocation loops after aging.

pathways. This may be accomplished by exploring post-growth annealing schemes and optimizing the design of trapping layers and will be discussed further in the following sections.

II. Further Addressing Point-Defect Degradation

As discussed briefly in Chapter 8, discovering and addressing the source of point defects and their multiplication mechanism is an important remaining challenge to high reliability InAs QD lasers. This is an exceptionally difficult task and has been a known issue with GaAs-based lasers for decades. Point defects cannot be studied directly by microscopy techniques such as TEM, which can only see symptoms of their presence in dislocation loops and possibly in slight contrast variations arising from point defect clusters. Cathodoluminescence (CL) and electron-beam-induced current (EBIC) allow more direct observation of the optical and electrical effects of point defects but are not widely used and have much lower spatial resolution than TEM. Electrical measurements such as deep-level transient spectroscopy (DLTS) is perhaps the most effective method to study point defects since it can help identify a signature associated with a point defect, which can sometimes be matched with a known defect in literature, but it can also track the concentration of defects in the device over time. This was done 40 years ago by Kondo et al. [194] for an AlGaAs double-heterostructure LED over the course of 7000 h of aging, shown in Figure 9.5. More recently, Zenari et al. have demonstrated the presence of a hole trap common to both devices on GaAs and on silicon [204], but the

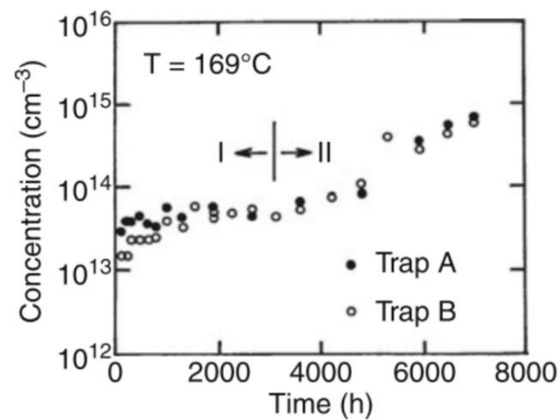

Figure 9.5. Deep-level transient spectroscopy (DLTS) measuring trap state concentrations in an AlGaAs LED during aging. After [194].

evolution of this defect state has not been studied after aging the device. It is tentatively ascribed to a native point defect or an oxygen complex. This points to potential growth-related alterations in reducing the grown-in density of native point defects. Still the trap density in GaAs was below 10^{13} cm^{-3}, so attaining even lower starting densities may be difficult. Buffolo et al. [205] associate the square-root dependence of threshold current change on time with a diffusion-related process, which should have a similar dependence. They identify the dopant beryllium as a plausible source of this degradation and suggest swapping beryllium for a less mobile dopant such as carbon in the active region. This is currently being investigated by collaborators.

If beryllium doping turns out not to be a primary issue, and instead native point defects generated during growth are the culprit, then infinite life GaAs-based devices may be unattainable. However, reliability lifetimes on silicon are already good enough that moderate improvements may be enough for commercially relevant products to be realized. For example, researchers at Hisilicon [196] have demonstrated impressive reliability results for InAs QD lasers on silicon with trapping layers, very similar those discussed in this thesis. They achieve minimal degradation in threshold current (<10%) and output power (<5%) over 3000 h aging at 85 °C and 4 kA cm^{-2}. This is less degradation

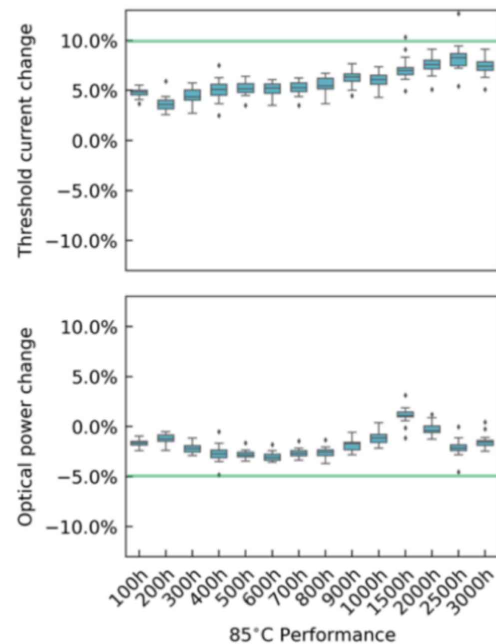

Figure 9.6. Laser degradation while aging at 85 °C and 100 mA (4 kA/cm^2) . After [196].

under significantly harsher aging conditions that we have so far demonstrated (typically 80 °C at 1-2 kA cm^{-2}), indicating that further improvements in reliability are achievable. Notably, TDD is several times higher than in our devices, but this may be compensated for by the shallow etch device fabrication and potentially improved trapping layer performance, though details are not given. Experiments are underway to investigate the effect of shallow etch geometry on QD laser reliability. Improved trapping layer performance is discussed in the following section.

Testing grown in point defect densities is challenging, but relative PL intensity can be a useful indicator of non-radiative recombination strength in the active region. For otherwise identical samples, different annealing treatments may reveal a process that raises PL intensity. Anneals are common practice for other types of devices to boost performance, but QDs are difficult since excessively high temperatures will begin to dissolve the dots into the matrix. Finally, other more fundamental change to the growth parameters and design of the QD active region may be worth investigating. Point defect formation should have some dependence on group V-III ratios during growth, so adjusting this, while compensating to maintain QD quality, could yield benefits. This may be exceptionally challenging, however, since QD growth recipes are finely tuned and altering one parameter cannot always be compensated with other parameters. Another design change to consider is to nucleate QDs on GaAs rather than InGaAs, however, achieving PL near 1.3 μm is challenging. Indeed, this is overall an exceptionally difficult problem to study. Given the limited utility of PL as an indicator of material quality, true confirmation of improvements requires fabricating and aging comparable lasers, all of which results in long experiment cycles times with many potentially confounding factors and roadblocks along the way. A slightly more feasible route may be to fabricate

simplified structures specifically for testing via DLTS to measure initial defect concentrations and concentrations after aging and then validating the new design with laser reliability testing.

III. Optimization of Trapping Layers

As detailed in Chapters 4 and 5, current trapping layer (TL) designs do not successfully hold all misfit dislocations (MDs) away from the active region. A significant fraction form at the adjacent active layer where they enhance non-radiative recombination and accelerate degradation through dislocation climb. Most all TLs implemented so far have had the same thickness and composition (7 nm of $In_{0.15}Ga_{0.15}As$ or $In_{0.15}Al_{0.15}As$). Only spacing from the active region has been tested. In the model structure the TL (InGaAs) is spaced 100 nm from the active QD layer and traps about 95% of all MDs. In laser reliability studies, TLs have been placed 80 and 180 nm from the active region on both sides and trap about 99% and 91% of all MDs, respectively, although these have larger error bars since this was measured by PV-STEM examination of a relatively small area (~80 μm^2). There is still a clear correlation between TL effectiveness and distance to the active layer. It is not yet clear, however, why TLs fail to trap some MDs. We suggest four possible mechanisms: (1) the space between the active region and TL exceeds thermal critical thickness and relaxes, (2) temperature cycling when growing the layers between the TL and active region causes glide of threading dislocation, (3) compressive lattice mismatch stress is relaxed during growth of the active region, and (4) threading dislocation pinning is not completely effective and allows some glide through the TL.

This first mechanism, depicted in Figure 9.7a, can already be excluded based on prior work [104]. We calculate the critical thickness for relaxation of the intermediate spacer layer based on the excess stress experienced by the dislocation from all sources, including residual lattice mismatch strain, thermal strain, and dislocation line tension. The maximum possible tensile

stress developed when cooling from growth temperature (580 °C) to room temperature is approximately 0.18%. At 300°C, near to where dislocation glide begins

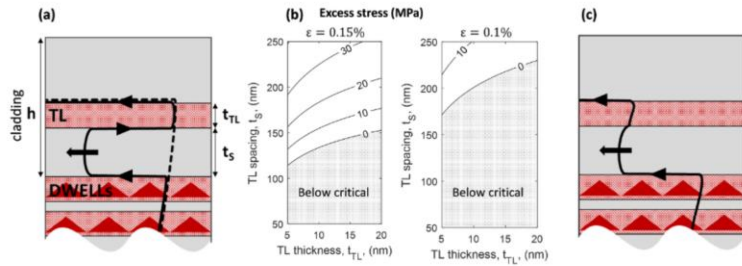

Figure 9.7. (a) Sketch of dislocation configuration at the end of growth (dotted line) and after cooling and relaxation (solid line). (b) Calculated critical thickness for relaxation by this mechanism for 0.15% and 0.10% strain. (d) Experimentally observed partial trapping dislocation configuration. After [104].

to freeze, tensile stress is at most 0.09%, assuming zero residual tensile or compressive stress at the end of growth. From Figure 9.7b, this clearly excludes this mechanism for a TL spacing of 80 nm but leaves open the possibility for the 180 nm structure. However, we have not experimentally observed the predicted dislocation structure suggested by Figure 9.7a. We instead observe a staircase-like structure, depicted in Figure 9.7c, (see in Figure 5.1b and Figure 4.3i).

The second proposed mechanism (relaxation during thermal cycling) is implausible for reasons similar to the first. In this case, the temperature change between the TL and intermediate (Al)GaAs layer growth is at most 80 °C and can only provide a up to 0.025% thermal strain in addition to some small residual strain from prior partial relaxation. The sign of this residual strain is not obvious, but it may be tensile due to how the metamorphic buffer structure is grown (relaxed InGaAs to GaAs), but since the buffer structure is cooled to room temperature before growing the laser, partial thermal stress relaxation may change this. Figure 9.8 demonstrates that to obtain the experimentally observed staircase dislocation structure (lower right diagram), TDs must relax compressive stress between the TL growth and the active region. Tensile stress relaxation at this stage would yield a configuration indicated by

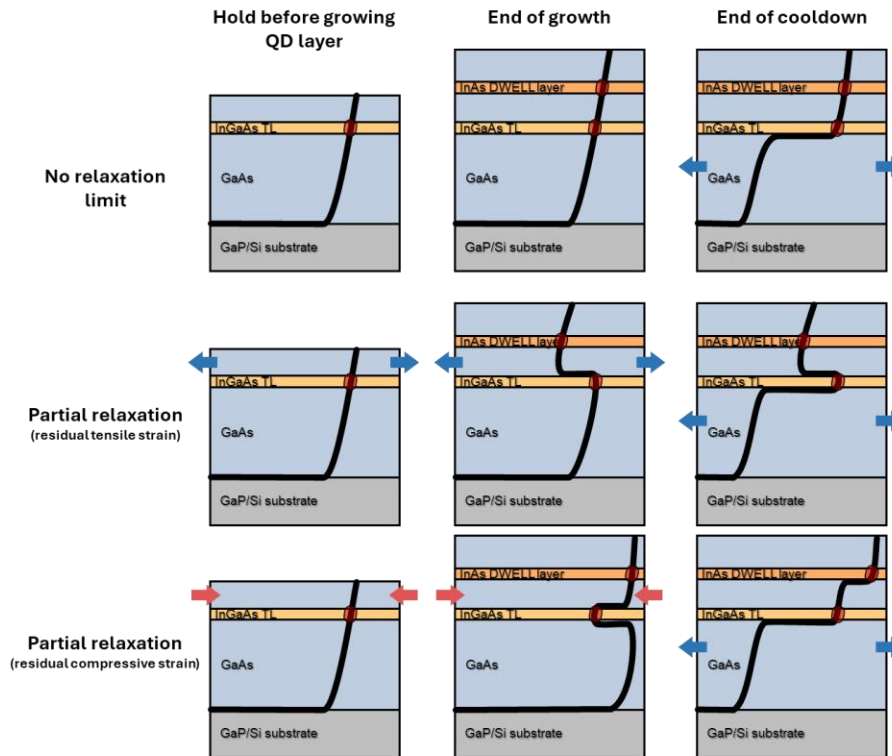

Figure 9.8 Thermal strain relaxation during growth between TLs and active layers. (Top) Limit of no relaxation; MDs form only at TLs. (Middle) Assuming relaxation of tensile stress after TL is grown but before dislocation is pinned by QD layer growth. (Bottom) Assuming relaxation of compressive stress. Only this last case would correctly produce dislocation configurations similar to those observed experimentally.

the middle right diagram of Figure 9.8, which we do not observe. It is difficult to imagine how a significant level of compressive stress could exist at this stage. Even assuming maximum thermal compressive stress (unlikely) and adding on extra residual compressive stress (also unlikely), critical thickness is still at least 300 nm, much larger than any tested conditions and unable to explain the partial TL failure in TL80 lasers. Lastly, we have grown a QW laser structure with no thermal cycling between growth of the first lower TL and final upper TL, and this structure still contained many untrapped MDs on the lower side of the active region.

The third mechanism (relaxation of compressive lattice mismatch stress during growth) is highly unlikely in QD structures since they are designed to be below critical thickness, but even if not, the in-plane stress from QDs strongly inhibits relaxation by threading dislocation

glide [32]. QDs themselves can be grown above critical thickness and nucleate new dislocations, but we see no evidence for this. QW structures, however, are susceptible to relaxation, particularly since structures which are stable against relaxation by nucleation of new dislocations (such as when growing on defect-free native substrates) can still be susceptible to partial relaxation by existing threading dislocations (when growing on lattice mismatched substrates). This case will be returned to shortly.

The final suggested mechanism, incomplete pinning of threading dislocations by the TLs, appears to be the most plausible, barring other unidentified mechanisms. Evidence in favor of this is that it will always produce staircase dislocation configurations, assuming the pinning failure occurs under tensile strain during cooldown. It is difficult to prove however, since the strength of pinning is hard to measure and seems to be different for different dislocations. In the first study from Chapter 3, with 5% indium alloying most dislocations are halted, but a small number do still glide slowly (Figure 3.4). The number of gliding dislocations is too low in the 5% indium alloyed sample to yield the untrapped misfit densities observed (after accounting for differing TDDs and probable glide distances), but the 2% indium alloyed appears more compatible. The trapping layers have 7.5× the indium content of this sample, but TLs are only thin layers and are subject to line tension from trapped MDs and bowed TDs, so the two cases are difficult to compare directly. By this mechanism the improvement in pinning with smaller TL spacing would be due to the reduced excess stress from reduced TD bowing between the TL and the active region. This TD bowing effect is depicted in Figure 9.7c. If the TD pinning mechanism is indeed random fluctuations in indium alloy composition (Figure 4.5), then raising the indium composition and reducing thickness (to stay below critical thickness) would be a good compromise to enhance the pinning effect.

In addition to adjusting the spacing, composition, and thickness of the TLs, the number of TLs is also a useful parameter to consider. Aging data from the TL80 laser in Chapter 5 may indicate the trapped MDs are too close to the edge of the doped layer and are slowly capturing carriers and climbing. A second TL would extend the pinning effect further and hold all MDs at the outermost TLs. This has just begun to be explored very recently with the growth of two QW laser structures with two TLs on each side of the active region. Cross sectional STEM of these structures is shown in Figure 9.9. The number of misfit dislocations counted at each of the layers is summarized in Table 9.1. Interestingly, TL effectiveness is best for the QW laser with just two total TLs (one on each side). Additionally, the two lasers with 4 total TLs have an exceptionally high density of untrapped MDs on the lower side. The reason for this may be that the three QWs of the active region (6.5 nm $In_{0.20}Ga_{0.80}As$ separated by 8 nm GaAs) could be relaxing during growth, as suggested by the third mechanism earlier. While this structure is not stressed enough to nucleate new dislocations, it is likely thick enough to partially relax by glide of existing threading dislocations. For the average 35.5 nm structure comprising three QWs and two spacers, the Matthews-Blakeslee [127] critical thickness, which describes the point at which it is energetically favoarable for an existing TD to glide and form a

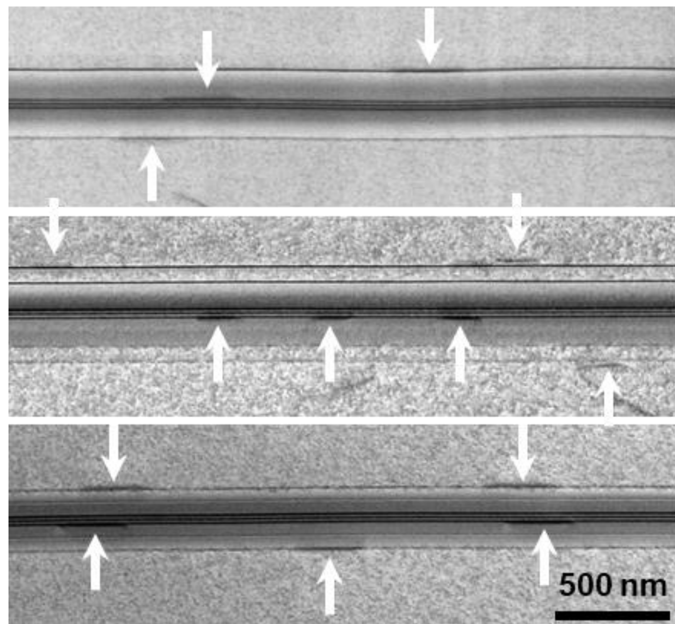

Figure 9.9. [100]-zone cross sectional STEM of three QW lasers on silicon with different trapping layer configurations. The correspond to the three lasers detailed in Table 9.1.

Table 9.1. Comparison of TL performance three QW laser structures with different TL configurations. Overall TL performance is worse with the extra TLs but the lack of MDs at the top QW is promising (see text for details).

Layer	2 TLs at 120 nm	4 TLs at 110 nm and 60 nm	4 TLs at 50 nm and 50 nm
Sample length (μm)	21.0	13.8	20.4
Number of MDs at…			
Top TL(s)	7	13	7
Top QW	3	0	0
Bottom QW	1	9	7
Bottom TL(s)	9	7	6
TL effectiveness (%)	80	69	70

MD, is 38 nm, assuming that MDs form both above and below the active region and that strain relaxation occurs solely within the active region. If, however, we modify the energetics to only require one misfit dislocation at the bottom (rather than an additional at the top), the critical thickness is reduced to just 16 nm, which would be exceeded while growing just the second QW layer. It might be that the extra compressive stress from the TLs encourages relaxation by TD glide, and this effect is amplified when growing two TLs on the lower side. These additional untrapped MDs only appear on the lower side of the active region in this case because relaxation occurs while the QWs are being grown, so only a lower side MD is formed. The additional local stress from that MD is not enough to form an opposite sign MD on the upper side for a reasonable overgrowth thickness, particularly after the upper TLs are grown. The lack of untrapped MDs on the upper side in both structures with 4 TLs is a promising sign that extra closely spaced TLs are effective in preventing untrapped MD formation. A continuation of this initial study is ongoing.

Additional structures can include a QW laser with a single active layer (rather than three) or a QD laser whose active region cannot reasonably relax by threading dislocation glide.

Additional model structures should also be grown for more robust statistical measurements of the effectiveness of multiple TLs. MD sharpness declines rapidly below 200 nm depth by ECCI, so a plausible structure would be a QD layer at 50 nm depth with two additional TLs each spaced 50 nm below the previous layer. Also, to test the effect of TL composition, a similar structure with a single TL spaced at 100 nm (similar to the original model structure) but with a higher indium content of 25% and a reduced thickness of 4 nm, to avoid relaxation.

Looking forward, one method being pursued to couple light from QD lasers on silicon into waveguides in the silicon is to grow the lasers in recessed pockets. For sufficiently narrow pockets stress is partially relaxed due to expansion at the free surface and in the perpendicular direction through the Poisson effect. This has been demonstrated to reduce total MD density formed near the active region due to the reduced tensile stress that builds up during cooldown [198]. This may also reduce unpinning of TDs in the TLs and improve TL effectiveness. Preliminary evidence of this is shown in Figure 9.10. This structure has >98% TL effectiveness. Zero MDs are observed next to the QD layers, while 16 and 30 were observed

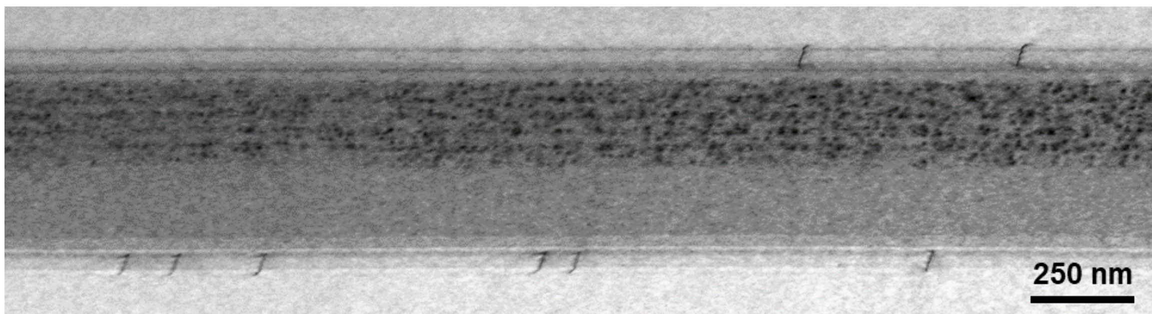

Figure 9.10. Tilted cross sectional STEM (**g** = 220) of a QD laser grown in a 50 μm pocket. Misfit dislocations are visible at the upper and lower TL but not in the QDs themselves. There are 5 total QD layers, but they are not individually distinct due to the tilt angle. The lower TL is positioned further from the active region (280 nm) than intended due to a growth error.

at the upper and lower TLs, respectively, along the 25 μm length of the foil. This high effectiveness is believed to be due to the reduced stress from in-pocket growth, and perhaps

additional stress relaxation from the moderately high TDD, rather than the distant lower TL placement, which cannot be explained by any of the four previously proposed mechanisms.

IV. Feasibility of a Reliable QW Laser on Silicon with Trapping Layers

Given the incredible success of TLs in improving reliability of QD lasers on silicon, it is natural to wonder if similar benefits can be bestowed upon QW lasers. Such lasers could open up a much wider range of materials and wavelengths beyond those compatible with self-organized QDs formed via Stranski–Krastanov (SK) growth. This may be limited to InGaAs QWs with (Al)GaAs due to the unusual situation of alloy hardening only in the active region, which leads to the problem of MDs which TLs solve. There are good reasons to be doubtful, though, that a reasonably reliable QW laser on silicon is possible, even with the aid of TLs. The current record lifetime for a QW laser on silicon is about 200 h when aged at room temperature just above threshold [20]. This is achieved by lateral epitaxial overgrowth to form a relatively defect free region where the QW laser is fabricated. But clearly, there are still some small number of defects that are able to rapidly degrade the laser. TLs would certainly hold

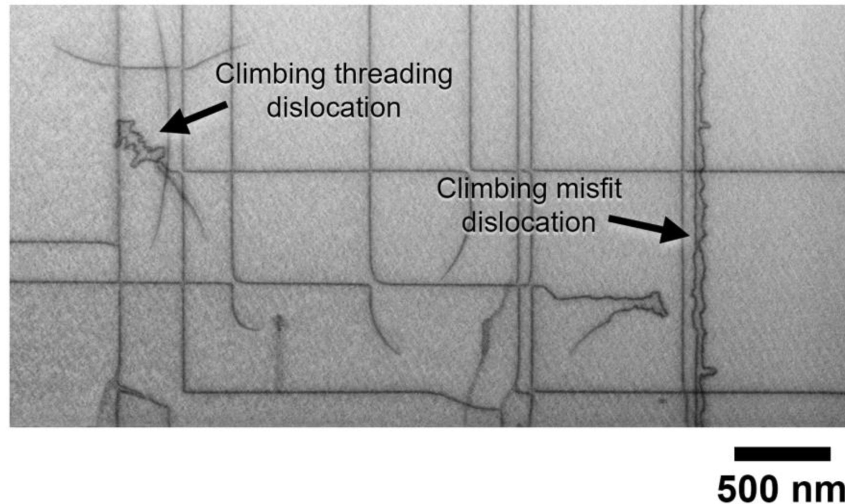

Figure 9.11. Plan-view STEM of a QW laser after 58 h aging sub-threshold at 35 C and 150 mA (2000 A cm^{-2}). A small fraction of the MDs are untrapped and show signs of climb. But the TDs also show significant climb, even after a relatively modest aging run.

MDs away from the active region, but even if they are perfectly effective, they have no effect on the TDs that will still pass through the active region. These TDs are still potent sources of non-radiative recombination and will degrade the laser through dislocation climb processes similar to misfit dislocations. QW structures lack the large lateral strain fields of QDs which help confine and limit the extent of dislocation climb, so it will proceed unimpeded until the device fails. Figure 9.11 shows the early stages of this process occurring in an aged QW laser with TLs, where both MDs and TDs are climbing and contributing to degradation.

The best performance for a QW laser on silicon with TLs aging at 20 °C at 1.2× threshold is shown in Figure 9.12a. The device stops lasing after 36 min at the stress condition and doubles its threshold after about 4 hours. This result is a small improvement on what others have achieved for similar lasers on 001 silicon for similar aging conditions (threshold doubling after 32 min), but they also achieve a 92 h lifetime for a laser on miscut Si with a lower TD density [206]. Pre- and post-aging back side EL imaging of a separate device (Figure 9.12b) reveal that degradation is broadly spread throughout the length of the laser (EL only shows a small section here). This rate of degradation can certainly be slowed with an altered active

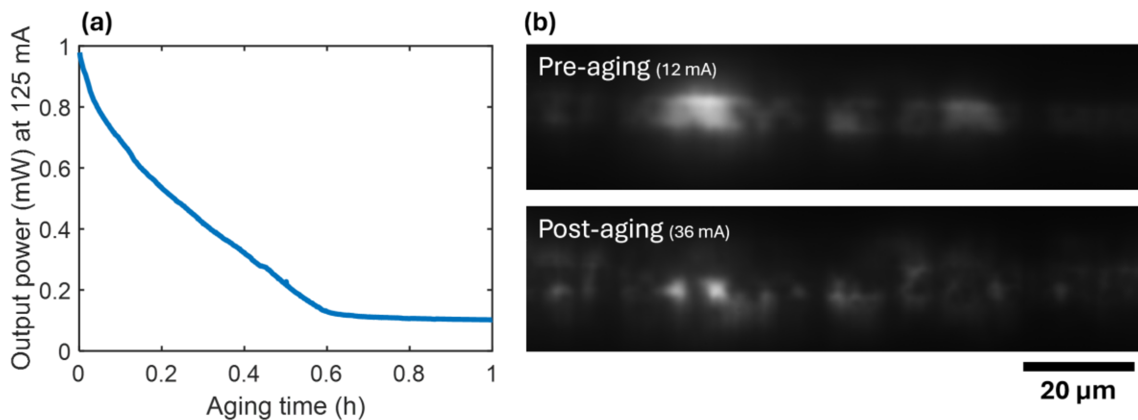

Figure 9.12. (a) Degradation of a QW laser on silicon with TLs aging at 1.2× threshold. Threshold doubles after about 4 hours. (b) Pre- and post-aging EL of a different QW laser with TLs. Note that after aging the device must be biased with 3× the current for EL imaging.

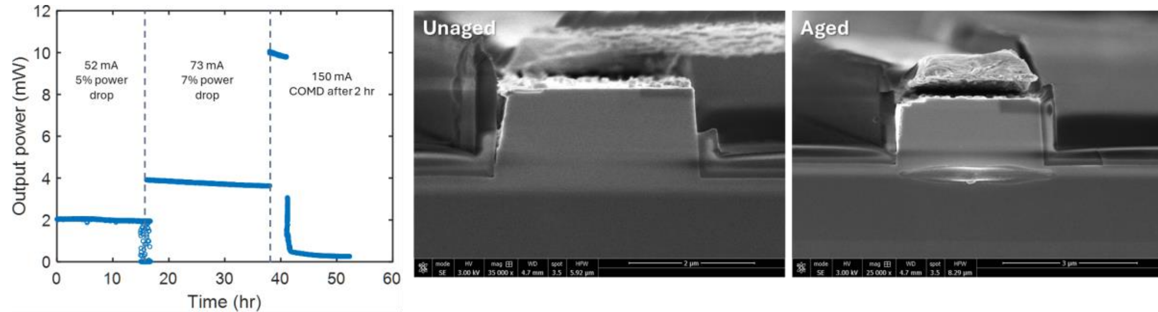

Figure 9.13. (Left) Catastrophic failure at the facet of a QW laser after gradually increasing output power. Failure occurs after 2 h at about 10 mW output power. (Right) SEM of the laser facet of an unaged and aged QW laser that has failed catastrophically at the facet.

region, perhaps with fewer QWs to minimize untrapped MDs as discussed in the previous section, but ultimately performance gains are expected to quickly be limited by degradation at TDs long before commercially relevant device lifetimes are achieved.

The QW degradation discussed so far has primarily been spread throughout the active region of the device and concentrated at dislocations, but QW lasers are also especially prone to facet failure, termed catastrophic optical mirror damage (COMD), in comparison to QD lasers. An example of facet-mediated failure in a QW laser is shown in Figure 9.13 where after aging at 10 mW at 80 °C for 2 h, the output power quickly drops to zero due to heating and melting of the facet. SEM of a QW laser with a melt-damaged facet is also shown in Figure 9.13. QW lasers are especially prone to this due their long lateral carrier diffusion lengths and lack of lateral carrier confinement. Typical InAs QDs do not perfectly confine carriers at room temperature, but there is still some

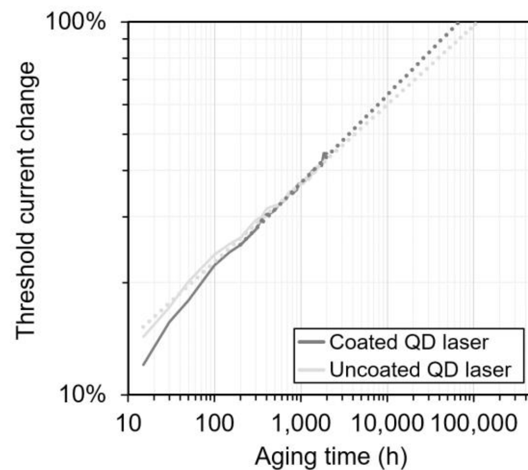

Figure 9.14. Effect of facet coating on QD laser degradation is minimal. Lasers are 5 layers of InAs QD on a GaAs substrate aging at 80 °C, 150 mA (3300 A cm^{-2}), ~7 mA single facet output power (uncoated). Plotted is the median performing device of 4-6 devices for each group.

benefit at a minimum from the reduced lateral carrier diffusion from carrier scattering at the QDs [28]. The comparative indifference of QD lasers to facet coatings, demonstrated by Figure 9.14, is striking. Degradation rates for the several coated and uncoated lasers are effectively identical. This is very different than in QW lasers, where facet coating is important to suppressing gradual aging near the facets [207], [208]. Facet coatings are also important to increasing COMD in QW lasers and typically provide a ~3x increase compared to uncoated lasers for 850nm GaAs-AlGaAs single QW lasers.

V. Conclusion

This thesis has detailed the dramatic improvements in laser reliability achieved through improved understanding of dislocation and point defect evolution. Record reliability for InAs QD lasers on silicon has been demonstrated, though it still falls 10x-100x short of strict industry requirements. Further gains due to improved understanding of point defect evolution and dislocation loop formation are attainable, but more work is needed in this area to better diagnose these gradual degradation mechanisms common to most GaAs-based devices. Looking forward, true integration with silicon, coupling light directly into waveguides, looks highly promising with recent demonstrations of lasers grown in recessed pockets with favorable reliability. Lateral stress relaxation enabled by pocket growth and the potential for removal of glissile dislocations at the pocket edges may eventually lead to higher device performance than planar growth. This will depend on improving QD uniformity across all active layers to improve gain and reduce threshold current densities. But once these hurdles are cleared, highly scalable and reliable lasers monolithically integrated for silicon photonics will be commercially viable and promise to accelerate the opening of a vast new technological frontier.

10. References

[1] T. Walther and E. S. Fry, 'Optical Communication: Its History and Recent Progress', in *Optics in Our Time*, 2016, pp. 178–198. doi: 10.1007/978-3-319-31903-2_9.

[2] N. Margalit, C. Xiang, S. M. Bowers, A. Bjorlin, R. Blum, and J. E. Bowers, 'Perspective on the future of silicon photonics and electronics', *Appl Phys Lett*, vol. 118, no. 22, p. 220501, Jun. 2021, doi: 10.1063/5.0050117.

[3] F. Kish *et al.*, 'System-on-Chip Photonic Integrated Circuits', *IEEE Journal of Selected Topics in Quantum Electronics*, vol. 24, no. 1, pp. 1–20, 2018, doi: 10.1109/JSTQE.2017.2717863.

[4] C. V. Poulton *et al.*, 'Coherent solid-state LIDAR with silicon photonic optical phased arrays', *Opt Lett*, vol. 42, no. 20, p. 4091, Oct. 2017, doi: 10.1364/ol.42.004091.

[5] X. Zhang, K. Kwon, J. Henriksson, J. Luo, and M. C. Wu, 'A large-scale microelectromechanical-systems-based silicon photonics LiDAR', *Nature*, vol. 603, no. 7900, pp. 253–258, Mar. 2022, doi: 10.1038/s41586-022-04415-8.

[6] Y. Jiang, P. T. S. DeVore, and B. Jalali, 'Analog optical computing primitives in silicon photonics', *Opt Lett*, vol. 41, no. 6, p. 1273, Mar. 2016, doi: 10.1364/ol.41.001273.

[7] N. L. Kazanskiy, M. A. Butt, and S. N. Khonina, 'Optical Computing: Status and Perspectives', *Nanomaterials*, vol. 12, no. 13. MDPI, Jul. 01, 2022. doi: 10.3390/nano12132171.

[8] J. W. Silverstone, D. Bonneau, J. L. Obrien, and M. G. Thompson, 'Silicon Quantum Photonics', *IEEE Journal of Selected Topics in Quantum Electronics*, vol. 22, no. 6, pp. 390–402, Nov. 2016, doi: 10.1109/JSTQE.2016.2573218.

[9] D. Bunandar *et al.*, 'Metropolitan Quantum Key Distribution with Silicon Photonics', *Phys Rev X*, vol. 8, no. 2, Apr. 2018, doi: 10.1103/PhysRevX.8.021009.

[10] T. Rudolph, 'Why i am optimistic about the silicon-photonic route to quantum computing', *APL Photonics*, vol. 2, no. 3, Mar. 2017, doi: 10.1063/1.4976737.

[11] T. J. Steiner *et al.*, 'Ultrabright Entangled-Photon-Pair Generation from an AlGaAs - On-Insulator Microring Resonator', *PRX Quantum*, vol. 2, no. 1, Jan. 2021, doi: 10.1103/PRXQuantum.2.010337.

[12] C. Zhang *et al.*, 'Integrated photonics beyond communications', *Appl Phys Lett*, vol. 123, no. 23, Dec. 2023, doi: 10.1063/5.0184677.

[13] B. Wang *et al.*, 'Modulation on silicon for datacom: Past, present, and future', *Progress in Electromagnetics Research*, vol. 166, no. October, pp. 119–145, 2019, doi: 10.2528/pier19102405.

[14] L. Vivien *et al.*, '42 GHz p.i.n germanium photodetector integrated in a silicon-on-insulator waveguide', *Opt Express*, vol. 17, no. 8, p. 6253, 2009.

[15] D. Liang and J. E. Bowers, ‘Recent Progress in Heterogeneous III-V-on-Silicon Photonic Integration’, *Light: Advanced Manufacturing*, vol. 2, no. 1, p. 59, 2021, doi: 10.37188/lam.2021.005.

[16] H.-C. Luan and L. C. Kimerling, ‘Cyclic Thermal Anneal for Dislocation Reduction’, US-6635110-B1, 2003

[17] D. Jung, P. G. Callahan, B. Shin, K. Mukherjee, A. C. Gossard, and J. E. Bowers, ‘Low threading dislocation density GaAs growth on on-axis GaP/Si (001)’, *J Appl Phys*, vol. 122, no. 22, 2017, doi: 10.1063/1.5001360.

[18] C. Shang *et al.*, ‘A Pathway to Thin GaAs Virtual Substrate on On-Axis Si (001) with Ultralow Threading Dislocation Density’, *Physica Status Solidi (A) Applications and Materials Science*, vol. 218, no. 3, pp. 1–9, 2021, doi: 10.1002/pssa.202000402.

[19] Z. Liu *et al.*, ‘Origin of Defect Tolerance in InAs/GaAs Quantum Dot Lasers Grown on Silicon’, *Journal of Lightwave Technology*, vol. 38, no. 2, pp. 240–248, Jan. 2020, doi: 10.1109/JLT.2019.2925598.

[20] Z. I. Kazi, P. Thilakan, T. Egawa, Umeno, Masayoshi, and T. Jimbo, ‘Realization of GaAs/AlGaAs Lasers on Si Substrates Using Epitaxial Lateral Overgrowth by Metalorganic Chemical Vapor Deposition’, *Jpn J Appl Phys*, vol. 40, p. 4903, 2001.

[21] M. Sugo, H. Mori, Y. Sakai, and Y. Itoh, ‘Stable cw operation at room temperature of a 1.5-µm wavelength multiple quantum well laser on a Si substrate’, *Appl Phys Lett*, vol. 60, no. 4, pp. 472–473, 1992, doi: 10.1063/1.106638.

[22] M. Tachikawa, T. Yamada, T. Sasaki, H. Mori, and Y. Kadota, ‘Laser-Diode-Quality InP/Si Grown by Hydride Vapor Phase Epitaxy’, *Jpn J Appl Phys*, vol. 34, pp. 657–659, 1995.

[23] T. Sasaki, H. Mori, M. Tachikawa, and T. Yamada, ‘Aging tests of InP-based laser diodes heteroepitaxially grown on Si substrates’, *J Appl Phys*, vol. 84, no. 12, pp. 6725–6728, Dec. 1998, doi: 10.1063/1.368999.

[24] S. A. Ringel, R. M. Sieg, S. M. Ting, and E. A. Fitzgerald, ‘Anti-Phase Domain-Free GaAs On Ge Substrates Grown By Molecular Beam Epitaxy for Space Solar Cell Applications’, in *IEEE 26th Photovoltaic Specialists Conference (PVSC)*, 1997.

[25] Q. Li, K. W. Ng, and K. M. Lau, ‘Growing antiphase-domain-free GaAs thin films out of highly ordered planar nanowire arrays on exact (001) silicon’, *Appl Phys Lett*, vol. 106, no. 7, Feb. 2015, doi: 10.1063/1.4913432.

[26] I. Németh, B. Kunert, W. Stolz, and K. Volz, ‘Heteroepitaxy of GaP on Si: Correlation of morphology, anti-phase-domain structure and MOVPE growth conditions’, *J Cryst Growth*, vol. 310, no. 7–9, pp. 1595–1601, Apr. 2008, doi: 10.1016/j.jcrysgro.2007.11.127.

[27] K. Volz *et al.*, ‘GaP-nucleation on exact Si (0 0 1) substrates for III/V device integration’, *J Cryst Growth*, vol. 315, no. 1, pp. 37–47, Jan. 2011, doi: 10.1016/j.jcrysgro.2010.10.036.

[28] J. Selvidge *et al.*, ‘Non-radiative recombination at dislocations in InAs quantum dots grown on silicon’, *Appl Phys Lett*, vol. 115, no. 13, 2019, doi: 10.1063/1.5113517.

[29] A. Y. Liu, R. W. Herrick, O. Ueda, P. M. Petroff, A. C. Gossard, and J. E. Bowers, 'Reliability of InAs/GaAs quantum dot lasers epitaxially grown on silicon', *IEEE Journal on Selected Topics in Quantum Electronics*, vol. 21, no. 6, Nov. 2015, doi: 10.1109/JSTQE.2015.2418226.

[30] D. Jung *et al.*, 'Impact of threading dislocation density on the lifetime of InAs quantum dot lasers on Si', *Appl Phys Lett*, vol. 112, no. 15, 2018, doi: 10.1063/1.5026147.

[31] D. Jung *et al.*, 'Highly Reliable Low-Threshold InAs Quantum Dot Lasers on On-Axis (001) Si with 87% Injection Efficiency', *ACS Photonics*, vol. 5, no. 3, pp. 1094–1100, 2018, doi: 10.1021/acsphotonics.7b01387.

[32] R. Beanland, J. P. R. David, and A. M. Sanchez, 'Quantum dots in strained layers-preventing relaxation through the precipitate hardening effect', *J Appl Phys*, vol. 104, no. 12, 2008, doi: 10.1063/1.3028270.

[33] D. C. Joy, D. E. Newbury, and D. L. Davidson, 'Electron channeling patterns in the scanning electron microscope', *J Appl Phys*, vol. 53, no. 8, pp. R81–R122, Aug. 1982, doi: 10.1063/1.331668.

[34] N. El-Masry, J. C. L. Tarn, T. P. Humphreys, N. Hamaguchi, N. H. Karam, and S. M. Bedair, 'Effectiveness of strained-layer superlattices in reducing defects in GaAs epilayers grown on silicon substrates', *Appl Phys Lett*, vol. 51, no. 20, pp. 1608–1610, 1987, doi: 10.1063/1.98570.

[35] P. Kightley, P. J. Goodhew, R. R. Bradley, and P. D. Augustus, 'A mechanism of misfit dislocation reaction for GaInAs strained layers grown onto off-axis GaAs substrates', *J Cryst Growth*, vol. 112, no. 2–3, pp. 359–367, 1991, doi: 10.1016/0022-0248(91)90311-R.

[36] B. Y. Tsaur *et al.*, 'Low-dislocation-density GaAs epilayers grown on Ge-coated Si substrates by means of lateral epitaxial overgrowth', *Appl Phys Lett*, vol. 41, no. 4, pp. 347–349, 1982, doi: 10.1063/1.93508.

[37] R. W. Herrick, 'Reliability engineering in optoelectronic devices and fiber optic transceivers', in *Reliability of Semiconductor Lasers and Optoelectronic Devices*, O. Ueda and S. J. Pearton, Eds., Springer, 2021, pp. 47–87.

[38] G. F. Burns and C. G. Fonstad, 'Monolitahic Fabrication of Strain-Free (Al,Ga)As Heterostructure Lasers on Silicon Substrates', vol. 4, no. 1, pp. 18–21, 1992.

[39] B. Monemar, 'Degradation Processes in Semiconductor Lasers', *Phys Scr*, vol. 24, no. 2, pp. 365–374, 1981, doi: 10.1088/0031-8949/24/2/002.

[40] M. E. Groenert, A. J. Pitera, R. J. Ram, and E. A. Fitzgerald, 'Improved room-temperature continuous wave GaAs/AlGaAs and InGaAs/GaAs/AlGaAs lasers fabricated on Si substrates via relaxed graded GexSi1-x buffer layers', *Journal of Vacuum Science and Technology B: Microelectronics and Nanometer Structures*, vol. 21, no. 3, pp. 1064–1069, May 2003, doi: 10.1116/1.1576397.

[41] Y. A. Osipyan, V. F. Petrenko, A. V. Zaretskiĭ, and R. W. Whitworth, 'Properties of II-VI semiconductors associated with moving dislocations', *Adv Phys*, vol. 35, no. 2, pp. 115–188, 1986, doi: 10.1080/00018738600101871.

[42] S. Koubaiti, J. J. Couderc, C. Levade, and G. Vanderschaeve, 'Photoplastic effect and Vickers microhardness in III-V and II-VI semiconductor compounds', *Materials Science and Engineering: A*, vol. 234–236, no. 1, pp. 865–868, 1997, doi: 10.1016/s0921-5093(97)00400-0.

[43] P. Petroff and R. L. Hartman, 'Rapid degradation phenomenon in heterojunction GaAlAs – GaAs lasers Rapid degradation phenomenon in heterojunction GaAIAs-GaAs lasers', *J Appl Phys*, vol. 45, no. 9, pp. 3899–3903, 1974.

[44] K. Maeda, Y. Yamashita, N. Maeda, and S. Takeuchi, 'Radiation Enhanced Dislocation Glide and Rapid Degradation', *MRS Online Proceedings Library (OPL)*, vol. 184, pp. 69–80, 1990, doi: 10.1557/proc-184-69.

[45] S. L. Yellen *et al.*, 'Reliability of GaAs-Based Semiconductor Diode Lasers: 0.6–1.1 μm', *IEEE J Quantum Electron*, vol. 29, no. 6, pp. 2058–2067, 1993, doi: 10.1109/3.234469.

[46] Y. Hasegawa, T. Egawa, T. Jimbo, and M. Umeno, 'Suppression of 〈100〉 dark-line defect growth in AlGaAs/InGaAs single quantum well lasers grown on Si substrates', *Japanese Journal of Applied Physics, Part 1: Regular Papers and Short Notes and Review Papers*, vol. 35, no. 11, pp. 5637–5641, 1996, doi: 10.1143/JJAP.35.5637.

[47] R. F. Murison, A. H. Moore, N. Holehouse, and S. R. Lee, 'Are InAlGaAs strained-layer quantum-well lasers more reliable?', *Laser Diode Technology and Applications V*, vol. 1850, no. June 1993, p. 215, 1993, doi: 10.1117/12.146908.

[48] S. M. Ting and E. A. Fitzgerald, 'Metal-organic chemical vapor deposition of single domain GaAs on Ge/GexSi1-x/Si and Ge substrates', *J Appl Phys*, vol. 87, no. 5, pp. 2618–2628, 2000, doi: 10.1063/1.372227.

[49] H. C. Luan *et al.*, 'High-quality Ge epilayers on Si with low threading-dislocation densities', *Appl Phys Lett*, vol. 75, no. 19, pp. 2909–2911, 1999, doi: 10.1063/1.125187.

[50] O. O. Olubuyide, D. T. Danielson, L. C. Kimerling, and J. L. Hoyt, 'Impact of seed layer on material quality of epitaxial germanium on silicon deposited by low pressure chemical vapor deposition', *Thin Solid Films*, vol. 508, no. 1–2, pp. 14–19, 2006, doi: 10.1016/j.tsf.2005.06.120.

[51] D. Kohen *et al.*, 'The role of AsH3 partial pressure on anti-phase boundary in GaAs-on-Ge grown by MOCVD - Application to a 200 mm GaAs virtual substrate', *J Cryst Growth*, vol. 421, pp. 58–65, 2015, doi: 10.1016/j.jcrysgro.2015.04.003.

[52] T. J. Milakovich, 'Integration of GaAsP alloys on Si for high-efficiency III-V/Si PV', Massachusetts Instutute of Technology, 2015.

[53] T. Roesener, V. Klinger, C. Weuffen, D. Lackner, and F. Dimroth, 'Determination of heteroepitaxial layer relaxation at growth temperature from room temperature X-ray reciprocal space maps', *J Cryst Growth*, vol. 368, pp. 21–28, Apr. 2013, doi: 10.1016/j.jcrysgro.2013.01.007.

[54] H. Demers *et al.*, 'Three-dimensional electron microscopy simulation with the CASINO Monte Carlo software', *Scanning*, vol. 33, no. 3, pp. 135–146, 2011, doi: 10.1002/sca.20262.

[55] J. Y. Tinevez *et al.*, 'TrackMate: An open and extensible platform for single-particle tracking', *Methods*, vol. 115, no. 2017, pp. 80–90, 2017, doi: 10.1016/j.ymeth.2016.09.016.

[56] K. Maeda and S. Takeuchi, 'Enhanced glide of dislocations in gaas single crystals by electron beam irradiation', *Jpn J Appl Phys*, vol. 20, no. 3, pp. L165–L168, 1981, doi: 10.1143/JJAP.20.L165.

[57] P. G. Callahan, B. B. Haidet, D. Jung, G. G. E. Seward, and K. Mukherjee, 'Direct observation of recombination-enhanced dislocation glide in heteroepitaxial GaAs on silicon', *Phys Rev Mater*, vol. 2, no. 8, p. 081601, 2018, doi: 10.1103/PhysRevMaterials.2.081601.

[58] A. Djemel, J. Castaing, N. Visentin, and M. Bonnet, 'Influence of thermal treatments on the electronic activity of dislocations in GaAs observed by cathodoluminescence', *Semicond Sci Technol*, vol. 5, no. 12, pp. 1221–1224, 1990, doi: 10.1088/0268-1242/5/12/013.

[59] M. Albrecht, J. L. Weyher, B. Lucznik, I. Grzegory, and S. Porowski, 'Nonradiative recombination at threading dislocations in n-type GaN: Studied by cathodoluminescence and defect selective etching', *Appl Phys Lett*, vol. 92, no. 23, 2008, doi: 10.1063/1.2928226.

[60] K. Mukherjee, C. H. Reilly, P. G. Callahan, and G. G. E. Seward, 'Recombination activity of threading dislocations in GaInP influenced by growth temperature', *J Appl Phys*, vol. 123, no. 16, p. 165701, Apr. 2018, doi: 10.1063/1.5018849.

[61] B. W. Dodson and J. Y. Tsao, 'Relaxation of strained-layer semiconductor structures via plastic flow', *Appl Phys Lett*, vol. 51, no. 17, pp. 1325–1327, 1987, doi: 10.1063/1.98667.

[62] K. Maeda, M. Sato, A. Kubo, and S. Takeuchi, 'Quantitative measurements of recombination enhanced dislocation glide in gallium arsenide', *J Appl Phys*, vol. 54, no. 1, pp. 161–168, 1983, doi: 10.1063/1.331725.

[63] K. Maeda and S. Takeuchi, 'RECOMBINATION ENHANCED MOBILITY OF DISLOCATIONS IN III-V COMPOUNDS.', in *Journal de Physique (Paris), Colloque*, 1983, pp. 375–385. doi: 10.1051/jphyscol:1983445.

[64] G. P. Watson, M. O. Thompson, D. G. Ast, A. Fischer-Colbrie, and J. Miller, 'The isolation and nucleation of misfit dislocations in strained epitaxial layers grown on patterned, ion-damaged GaAs', *J Electron Mater*, vol. 19, no. 9, pp. 957–965, 1990, doi: 10.1007/BF02652922.

[65] R. S. Goldman, K. L. Kavanagh, H. H. Wieder, S. N. Ehrlich, and R. M. Feenstra, 'Effects of GaAs substrate misorientation on strain relaxation in InxGa1-xAs films and multilayers', *J Appl Phys*, vol. 83, no. 10, pp. 5137–5149, 1998, doi: 10.1063/1.367331.

[66] A. E. Romanov, W. Pompe, G. Beltz, and J. S. Speck, 'Modeling of threading dislocation density reduction in heteroepitaxial layers: I. Geometry and Crystallography', *Phys Status Solidi B Basic Res*, vol. 198, p. 599, 1996, doi: 10.1002/1521-3951(199701)199:1<33::AID-PSSB33>3.0.CO;2-U.

[67] S. Lopatin, S. J. Pennycook, J. Narayan, and G. Duscher, 'Z-contrast imaging of dislocation cores at the GaAs/Si interface', *Appl Phys Lett*, vol. 81, no. 15, pp. 2728–2730, 2002, doi: 10.1063/1.1511808.

[68] X. Xu *et al.*, 'Distortion and segregation in a dislocation core region at atomic resolution', *Phys Rev Lett*, vol. 95, no. 14, pp. 1–4, 2005, doi: 10.1103/PhysRevLett.95.145501.

[69] V. T. Gillard, W. D. Nix, and L. B. Freund, 'Role of dislocation blocking in limiting strain relaxation in heteroepitaxial films', *J Appl Phys*, vol. 76, no. 11, pp. 7280–7287, 1994, doi: 10.1063/1.358013.

[70] B. Bonef, R. D. Shah, and K. Mukherjee, 'Fast Diffusion and Segregation along Threading Dislocations in Semiconductor Heterostructures', *Nano Lett*, vol. 19, no. 3, pp. 1428–1436, 2019, doi: 10.1021/acs.nanolett.8b03734.

[71] P. A. Kirkby, 'Dislocation Pinning in GaAs by the Deliberate Introduction of Impurities', *IEEE J Quantum Electron*, vol. 11, no. 7, pp. 562–568, 1975, doi: 10.1109/JQE.1975.1068634.

[72] F. Louchet, 'The reduction of dislocation density in GaAs by in doping: a specific interaction of in with the cores of 30° partial dislocations', *Journal de Physique*, vol. 49, no. 7, pp. 1219–1224, 1988, doi: 10.1051/jphys:019880049070121900.

[73] N. Burle-Durbec, B. Pichaud, and F. Minari, 'Interactions of in atoms with partial dislocations cores in GaAs: 0.3% In', *Philos Mag Lett*, vol. 59, no. 3, pp. 121–129, 1989, doi: 10.1080/09500838908206333.

[74] H. Ehrenreich and J. P. Hirth, 'Mechanism for dislocation density reduction in GaAs crystals by indium addition', *Appl Phys Lett*, vol. 46, no. 7, pp. 668–670, 1985, doi: 10.1063/1.95523.

[75] J. C. Mikkelsen and J. B. Boyce, 'Extended x-ray-absorption fine-structure study of Ga(1-x)In(x)As random solid solutions', *Phys Rev B*, vol. 28, no. 12, pp. 7130–7140, 1983, [Online]. Available: http://link.aps.org/doi/10.1103/PhysRevB.28.7130

[76] D. Jung *et al.*, 'Recent Advances in InAs Quantum Dot Lasers Grown on On-Axis (001) Silicon by Molecular Beam Epitaxy', *Physica Status Solidi (A) Applications and Materials Science*, vol. 216, no. 1, pp. 1–5, 2019, doi: 10.1002/pssa.201800602.

[77] T. Ward *et al.*, 'Design rules for dislocation filters', *J Appl Phys*, vol. 116, no. 6, 2014, doi: 10.1063/1.4892162.

[78] J. Knall *et al.*, 'The use of graded InGaAs layers and patterned substrates to remove threading dislocations from GaAs on Si', *J Appl Phys*, vol. 76, no. 5, pp. 2697–2702, 1994, doi: 10.1063/1.357572.

[79] A. K. Chin, A. R. Von Neida, and R. Caruso, 'Spatially Resolved Cathodoluminescence Study of Semi-Insulating GaAs Substrates', *J Electrochem Soc*, vol. 129, no. 10, pp. 2386–2388, 1982, doi: 10.1149/1.2123548.

[80] R. Beanland, D. J. Dunstan, and P. J. Goodhew, 'Plastic relaxation and relaxed buffer layers for semiconductor epitaxy', *Adv Phys*, vol. 45, no. 2, pp. 87–146, 1996, doi: 10.1080/00018739600101477.

[81] D. J. Dunstan, ‘Strain and strain relaxation in semiconductors’, *Journal of Materials Science: Materials in Electronics*, vol. 8, no. 6, pp. 337–375, 1997, doi: 10.1023/A:1018547625106.

[82] M. E. Groenert *et al.*, ‘Monolithic integration of room-temperature cw GaAs/AlGaAs lasers on Si substrates via relaxed graded GeSi buffer layers’, *J Appl Phys*, vol. 93, no. 1, pp. 362–367, 2003, doi: 10.1063/1.1525865.

[83] E. T. Hughes, R. D. Shah, and K. Mukherjee, ‘Glide of threading dislocations in (In)AlGaAs on Si induced by carrier recombination: Characteristics, mitigation, and filtering’, *J Appl Phys*, vol. 125, no. 16, 2019, doi: 10.1063/1.5088844.

[84] I. Yonenaga and K. Sumino, ‘Mechanical strength of GeSi alloy’, *J Appl Phys*, vol. 80, no. 6, pp. 3244–3247, 1996, doi: 10.1063/1.363266.

[85] I. Yonenaga, K. Sumino, G. Izawa, H. Watanabe, and J. Matsui, ‘Mechanical property and dislocation dynamics of GaAsP alloy semiconductor’, *J Mater Res*, vol. 4, no. 2, pp. 361–365, 1989, doi: 10.1557/JMR.1989.0361.

[86] E. B. Yakimov, P. S. Vergeles, A. Y. Polyakov, I. H. Lee, and S. J. Pearton, ‘Radiation enhanced basal plane dislocation glide in GaN’, *Jpn J Appl Phys*, vol. 55, no. 5, 2016, doi: 10.7567/JJAP.55.05FM03.

[87] C. J. Humphreys, ‘The scattering of fast electrons by crystals’, *Reports on Progress in Physics*, vol. 42, no. 11, pp. 1825–1887, 1979, doi: 10.1088/0034-4885/42/11/002.

[88] J. C. Norman *et al.*, ‘The Importance of p-Doping for Quantum Dot Laser on Silicon Performance’, *IEEE J Quantum Electron*, vol. 55, no. 6, Dec. 2019, doi: 10.1109/JQE.2019.2941579.

[89] Y. Kamimura, K. Edagawa, and S. Takeuchi, ‘Experimental evaluation of the Peierls stresses in a variety of crystals and their relation to the crystal structure’, *Acta Mater*, vol. 61, no. 1, pp. 294–309, 2013, doi: 10.1016/j.actamat.2012.09.059.

[90] L. B. Freund, ‘The driving force for glide of a threading dislocation in a strained epitaxial layer on a substrate’, *J. Mech. Phys. Solids*, vol. 38, no. 5, pp. 657–679, 1989, doi: 10.1063/1.351154.

[91] W. D. Nix, D. B. Noble, and J. F. Turlo, ‘Mechanisms and Kinetics of Misfit Dislocation Formation in Heteroepitaxial Thin Films’, *MRS Proceedings*, vol. 188, 1990, doi: 10.1557/proc-188-315.

[92] H. Conrad, ‘Thermally activated deformation of metals’, *Journal of Metals*, vol. 16, no. 7, pp. 582–588, 1964, doi: 10.1007/bf03378292.

[93] K. Okazaki, ‘Solid-solution hardening and softening in binary iron alloys’, *J Mater Sci*, vol. 31, no. 4, pp. 1087–1099, 1996, doi: 10.1007/BF00352911.

[94] J. Selvidge *et al.*, ‘Defect filtering for thermal expansion induced dislocations in III-V lasers on silicon’, *Appl Phys Lett*, vol. 117, no. 12, p. 122101, Sep. 2020, doi: 10.1063/5.0023378.

[95] C. Shang *et al.*, 'High-temperature reliable quantum-dot lasers on Si with misfit and threading dislocation filters', *Optica*, vol. 8, no. 5, p. 749, 2021, doi: 10.1364/optica.423360.

[96] P. Petroff and R. L. Hartman, 'Defect structure introduced during operation of heterojunction GaAs lasers', *Appl Phys Lett*, vol. 23, no. 8, pp. 469–471, 1973, doi: 10.1063/1.1654962.

[97] S. O'Hara, P. W. Hutchinson, and P. S. Dobson, 'The origin of dislocation climb during laser operation', *Appl Phys Lett*, vol. 30, no. 8, pp. 368–371, 1977, doi: 10.1063/1.89432.

[98] O. Ueda, 'On degradation studies of III-V compound semiconductor optical devices over three decades: Focusing on gradual degradation', *Jpn J Appl Phys*, vol. 49, 2010, doi: 10.1143/JJAP.49.090001.

[99] P. J. Phillips, M. J. Mills, and M. De Graef, 'Systematic row and zone axis STEM defect image simulations', *Philosophical Magazine*, vol. 91, no. 16, pp. 2081–2101, 2011, doi: 10.1080/14786435.2010.547526.

[100] K. Mukherjee *et al.*, 'Recombination-enhanced dislocation climb in InAs quantum dot lasers on silicon', *J Appl Phys*, vol. 128, no. 2, p. 025703, Jul. 2020, doi: 10.1063/1.5143606.

[101] J. C. Norman *et al.*, 'Reliablity of lasers on silicon substrates for silicon photonics', in *Reliability of Semiconductor Lasers and Optoelectronic Devices*, 2021, pp. 239–271.

[102] P. Borvin, J. Rabier, H. Garem, and P. Borvin, 'Plastic deformation of GaAs single crystals as a function of electronic doping I: Medium temperatures (150–650°C)', *Philosophical Magazine A: Physics of Condensed Matter, Structure, Defects and Mechanical Properties*, vol. 61, no. 4, pp. 619–645, 1990, doi: 10.1080/01418619008231939.

[103] S. K. Choi, M. Mihara, and T. Ninomiya, 'Dislocation velocities in GaAs', *Jpn J Appl Phys*, vol. 16, no. 5, pp. 737–745, 1977, doi: 10.1143/JJAP.16.737.

[104] K. Mukherjee *et al.*, 'Kinetically limited misfit dislocations formed during post-growth cooling in III-V lasers on silicon', *J Phys D Appl Phys*, vol. 54, no. 49, 2021, doi: 10.1088/1361-6463/ac24c9.

[105] O. Ueda, 'Degradation of I II-V Opto-Electronic Devices', *J Electrochem Soc*, vol. 135, p. 11C, 1988.

[106] H. Temkin, C. L. Zipfel, and V. G. Keramidas, 'High-temperature degradation of InGaAsp/InP light emitting diodes', *J Appl Phys*, vol. 52, no. 8, pp. 5377–5380, 1981, doi: 10.1063/1.329398.

[107] K. Ishida, T. Kamejima, Y. Matsumoto, and K. Endo, 'Lattice defect structure of degraded InGaAsP-InP double-heterostructure lasers', *Appl Phys Lett*, vol. 40, pp. 16–17, 1982.

[108] O. Ueda, I. Umebu, S. Yamakoshi, and T. Kotani, 'Nature of dark defects revealed in InGaAsP/InP double heterostructure light emitting diodes aged at room temperature', *J Appl Phys*, vol. 53, no. 4, pp. 2991–2997, 1982, doi: 10.1063/1.331039.

[109] O. Ueda, K. Wakao, A. Yamaguchi, S. Isozumi, and S. Komiya, ‘Defect structures in rapidly degraded InGaAsP/InGaP double-heterostructure lasers’, *J Appl Phys*, vol. 57, no. 5, pp. 1523–1532, 1985, doi: 10.1063/1.334466.

[110] T. Kobayashi, T. Kawakami, and Y. Furukawa, ‘Thermal Diagnosis of Dark lines in Degraded GaAs-AlGaAs Double-Heterostructure Lasers’, *Jpn J Appl Phys*, vol. 14, no. 4, pp. 508–515, 1975, doi: 10.1143/JJAP.14.508.

[111] T. Kobayashi and G. Iwane, ‘Three Dimensional Thermal Problems of Double-Hetero Structure Semiconductor Lasers’, *Jpn J Appl Phys*, vol. 16, no. 8, pp. 1403–1408, 1977, doi: 10.1143/JJAP.16.1403.

[112] M. Fukuda, K. Wakita, and G. Iwane, ‘Observation Of Dark Defects Related To Degradation In Ingaasp/Inp Dh Lasers Under Accelerated Operation’, *Jpn J Appl Phys*, vol. 20, no. 2, p. L87, 1981, doi: 10.1143/JJAP.20.L87.

[113] V. Hortelano, J. Anaya, J. Souto, J. Jiménez, J. Perinet, and F. Laruelle, ‘Defect signatures in degraded high power laser diodes’, *Microelectronics Reliability*, vol. 53, no. 9–11, pp. 1501–1505, 2013, doi: 10.1016/j.microrel.2013.07.071.

[114] C. K. Chia, M. Suryana, and M. Hopkinson, ‘Thermal runaway and optical efficiency in InAs/GaAs quantum dot lasers’, *Appl Phys Lett*, vol. 95, no. 14, 2009, doi: 10.1063/1.3245305.

[115] G. Park, O. B. Shchekin, and D. G. Deppe, ‘Temperature dependence of gain saturation in multilevel quantum dot lasers’, *IEEE J Quantum Electron*, vol. 36, no. 9, pp. 1065–1071, 2000, doi: 10.1109/3.863959.

[116] N. F. Masse, S. J. Sweeney, I. P. Marko, A. R. Adams, N. Hatori, and M. Sugawara, ‘Temperature dependence of the gain in p -doped and intrinsic 1.3 μm InAsGaAs quantum dot lasers’, *Appl Phys Lett*, vol. 89, no. 19, 2006, doi: 10.1063/1.2387114.

[117] R. Wang, C. Z. Tong, S. F. Yoon, C. Y. Liu, H. X. Zhao, and Q. Cao, ‘Temperature characteristics of gain profiles in 1.3-μm p-doped and undoped InAs/GaAs quantum-dot lasers’, *IEEE Electron Device Letters*, vol. 30, no. 12, pp. 1311–1313, 2009, doi: 10.1109/LED.2009.2033718.

[118] L. V Asryan and R. A. Suris, ‘Temperature Dependence of the Threshold Current Density of a Quantum Dot Laser’, 1998.

[119] Y. Hu, D. Liang, and R. G. Beausoleil, ‘An advanced III-V-on-silicon photonic integration platform’, *Opto-Electronic Advances*, vol. 4, no. 9. 2021. doi: 10.29026/oea.2021.200094.

[120] D. Liang, G. Roelkens, R. Baets, and J. E. Bowers, ‘Hybrid integrated platforms for silicon photonics’, *Materials*, vol. 3, no. 3, pp. 1782–1802, 2010, doi: 10.3390/ma3031782.

[121] G. Kissinger and W. Kissinger, ‘Void-free silicon-wafer-bond strengthening in the 200-400 °C range’, *Sens Actuators A Phys*, vol. 36, no. 2, pp. 149–156, 1993, doi: 10.1016/0924-4247(93)85009-5.

[122] D. Liang and J. E. Bowers, ‘Highly efficient vertical outgassing channels for low-temperature InP-to-silicon direct wafer bonding on the silicon-on-insulator substrate’,

Citation: Journal of Vacuum Science & Technology B: Microelectronics and Nanometer Structures Processing, vol. 26, p. 1560, 2008, doi: 10.1116/1.2943667.

[123] S. Matsuo *et al.*, 'Room-temperature continuous-wave operation of lateral current injection wavelength-scale embedded active-region photonic-crystal laser', *Optics Express, Vol. 20, Issue 4, pp. 3773-3780*, vol. 20, no. 4, pp. 3773–3780, Feb. 2012, doi: 10.1364/OE.20.003773.

[124] T. Fujii *et al.*, 'Development of an epitaxial growth technique using iii-v on a si platform for heterogeneous integration of membrane photonic devices on si', *Applied Sciences (Switzerland)*, vol. 11, no. 4, pp. 1–22, 2021, doi: 10.3390/app11041801.

[125] C. Zhang, D. Liang, and J. E. Bowers, 'MOCVD regrowth of InP on hybrid silicon substrates', *ECS Solid State Letters*, vol. 2, no. 11, pp. 82–86, 2013, doi: 10.1149/2.008311ssl.

[126] Y. Hu *et al.*, 'III/V-on-Si MQW lasers by using a novel photonic integration method of regrowth on a bonding template', *Light Sci Appl*, vol. 8, no. 1, pp. 2047–7538, Dec. 2019, doi: 10.1038/s41377-019-0202-6.

[127] J. W. Matthews and A. E. Blakeslee, 'Defects in epitaxial multilayers: I. Misfit dislocations', *J Cryst Growth*, vol. 27, pp. 118–125, 1974, doi: 10.1016/S0022-0248(74)80055-2.

[128] K. J. Schmieder *et al.*, 'GaAs Solar Cells Grown on Sapphire with Multi-Layer Transfer Printed Virtual Substrates', *Conference Record of the IEEE Photovoltaic Specialists Conference*, pp. 1437–1440, 2019, doi: 10.1109/PVSC40753.2019.8981258.

[129] K. J. Schmieder *et al.*, 'Low-Cost Handle Study for Photovoltaics on Transfer Printed Virtual Substrates', *Conference Record of the IEEE Photovoltaic Specialists Conference*, vol. 2020-June, pp. 0528–0531, 2020, doi: 10.1109/PVSC45281.2020.9301002.

[130] R. Hull and J. C. Bean, 'Misfit Dislocations in Lattice-Mismatched Epitaxial Films', *Critical Reviews in Solid State and Materials Sciences*, vol. 17, no. 6, pp. 507–546, 1992, doi: 10.1080/10408439208244585.

[131] J. D. Weeks, J. C. Tully, L. C. Kimerling, B. Laboratories, and M. Hill, 'Theory of recombination-enhanced defect reactions in semiconductors', *Phys Rev B*, vol. 12, no. 8, pp. 3286–3292, 1975.

[132] R. Beanland, 'Multiplication of misfit dislocations in epitaxial layers', *J Appl Phys*, vol. 72, no. 9, pp. 4031–4035, 1992, doi: 10.1063/1.352257.

[133] P. M. J. Marée, J. C. Barbour, J. F. Van Der Veen, K. L. Kavanagh, C. W. T. Bulle-Lieuwma, and M. P. A. Viegers, 'Generation of misfit dislocations in semiconductors', *J Appl Phys*, vol. 62, no. 11, pp. 4413–4420, 1987, doi: 10.1063/1.339078.

[134] M. A. Tschopp and D. L. McDowell, 'Tension-compression asymmetry in homogeneous dislocation nucleation in single crystal copper', *Appl Phys Lett*, vol. 90, no. 12, p. 121916, 2007, doi: 10.1063/1.2715137.

[135] J. Selvidge *et al.*, 'Defect filtering for thermal expansion induced dislocations in III-V lasers on silicon', *Appl Phys Lett*, vol. 117, no. 12, p. 122101, Sep. 2020, doi: 10.1063/5.0023378.

[136] N. El-Masry, J. C. L. Tarn, T. P. Humphreys, N. Hamaguchi, N. H. Karam, and S. M. Bedair, 'Effectiveness of strained-layer superlattices in reducing defects in GaAs epilayers grown on silicon substrates', *Appl Phys Lett*, vol. 51, no. 20, pp. 1608–1610, 1987, doi: 10.1063/1.98570.

[137] K. A. Black, P. Abraham, A. Karim, J. E. Bowers, and E. L. Hu, 'Improved Luminescence from InGaAsP/InP MQW Active Regions using a Wafer Fused Superlattice Barrier', *11th International Conference on Indium Phosphide and Related Materials*, no. May, pp. 357–360, 1999.

[138] D. Liang, S. Srinivasan, J. Peters, A. Fang, and J. E. Bowers, 'Demonstration of Enhanced III-V-On-Silicon Hybrid Integration by Using a Strained Superlattice as a Defect Blocking Layer', *ECS Trans*, vol. 33, no. 4, pp. 421–426, 2010, doi: 10.1149/1.3483532.

[139] E. Simoen *et al.*, 'Device-based threading dislocation assessment in germanium hetero-epitaxy', *SBMicro 2019 - 34th Symposium on Microelectronics Technology and Devices*, pp. 20–25, 2019, doi: 10.1109/SBMicro.2019.8919472.

[140] T. Wosiński, 'Evidence for the electron traps at dislocations in GaAs crystals', *J Appl Phys*, vol. 65, no. 4, pp. 1566–1570, 1989, doi: 10.1063/1.342974.

[141] N. Grandjean *et al.*, 'Growth mode induced carrier localization in InGaN/GaN quantum wells', *Philosophical Magazine*, vol. 87, no. 13, pp. 2067–2075, 2007, doi: 10.1080/14786430701271942.

[142] F. C. P. Massabuau *et al.*, 'Carrier localization in the vicinity of dislocations in InGaN', *J Appl Phys*, vol. 121, no. 1, 2017, doi: 10.1063/1.4973278.

[143] K. Mukherjee, D. A. Beaton, A. Mascarenhas, M. T. Bulsara, and E. A. Fitzgerald, 'Effects of dislocation strain on the epitaxy of lattice-mismatched AlGaInP layers', *J Cryst Growth*, vol. 392, pp. 74–80, 2014, doi: 10.1016/j.jcrysgro.2014.01.058.

[144] K. L. Schulte, H. L. Guthrey, R. M. France, and J. F. Geisz, 'Guided Optimization of Phase-Unstable III-V Compositionally Graded Buffers by Cathodoluminescence Spectrum Imaging', *IEEE J Photovolt*, vol. 10, no. 1, pp. 109–116, 2020, doi: 10.1109/JPHOTOV.2019.2951927.

[145] S. B. Samavedam and E. A. Fitzgerald, 'Novel dislocation structure and surface morphology effects in relaxed Ge/Si-Ge(graded)/Si structures', *J Appl Phys*, vol. 81, no. 7, pp. 3108–3116, 1997, doi: 10.1063/1.364345.

[146] A. M. Andrews, J. S. Speck, A. E. Romanov, M. Bobeth, and W. Pompe, 'Modeling cross-hatch surface morphology in growing mismatched layers', *J Appl Phys*, vol. 91, no. 3, pp. 1933–1943, 2002, doi: 10.1063/1.1428091.

[147] M. Tapajna *et al.*, 'Influence of threading dislocation density on early degradation in AlGaN/GaN high electron mobility transistors', *Appl Phys Lett*, vol. 99, no. 22, p. 223501, 2011, doi: 10.1063/1.3663573.

[148] T. Nakano *et al.*, 'Screw dislocation that converts p-type GaN to n-type: Microscopic study on Mg condensation and leakage current in p-n diodes', *Appl Phys Lett*, vol. 117, no. 1, p. 12105, 2020, doi: 10.1063/5.0010664.

[149] P. Petroff and R. L. Hartman, 'Rapid degradation phenomenon in heterojunction GaAlAs – GaAs lasers Rapid degradation phenomenon in heterojunction GaAIAs-GaAs lasers', vol. 3899, no. May 2015, pp. 31–36, 1982.

[150] J. J. Coleman, R. G. Waters, and D. P. Bour, 'InGaAs-GaAs strained layer lasers: physics and reliability', *Laser Diode Technology and Applications III*, vol. 1418, no. July 1991, pp. 318–327, 1991, doi: 10.1117/12.43810.

[151] J. Jiménez, 'Laser diode reliability: Crystal defects and degradation modes', *Comptes Rendus Physique*, vol. 4, no. 6. Elsevier Masson SAS, pp. 663–673, Jul. 01, 2003. doi: 10.1016/S1631-0705(03)00097-5.

[152] A. Y. Liu, R. W. Herrick, O. Ueda, P. M. Petroff, A. C. Gossard, and J. E. Bowers, 'Reliability of InAs/GaAs quantum dot lasers epitaxially grown on silicon', *IEEE Journal on Selected Topics in Quantum Electronics*, vol. 21, no. 6, Nov. 2015, doi: 10.1109/JSTQE.2015.2418226.

[153] S. Chen *et al.*, 'Electrically pumped continuous-wave III-V quantum dot lasers on silicon', *Nat Photonics*, vol. 10, no. 5, pp. 307–311, 2016, doi: 10.1038/nphoton.2016.21.

[154] J. Selvidge *et al.*, 'Reduced dislocation growth leads to long lifetime InAs quantum dot lasers on silicon at high temperatures', *Appl Phys Lett*, vol. 118, no. 19, p. 192101, May 2021, doi: 10.1063/5.0052316.

[155] J. Liu *et al.*, 'Theoretical analysis and modelling of degradation for III-V lasers on Si', *J Phys D Appl Phys*, vol. 55, no. 40, 2022, doi: 10.1088/1361-6463/ac83d3.

[156] R. M. France, F. Dimroth, T. J. Grassman, and R. R. King, 'Metamorphic epitaxy for multijunction solar cells', *MRS Bull*, vol. 41, no. 3, pp. 202–209, 2016, doi: 10.1557/mrs.2016.25.

[157] A. Ren, L. Yuan, H. Xu, J. Wu, and Z. Wang, 'Recent progress of III-V quantum dot infrared photodetectors on silicon', *J Mater Chem C Mater*, vol. 7, no. 46, pp. 14441–14453, 2019, doi: 10.1039/c9tc05738b.

[158] E. Tournié, L. Cerutti, J. B. Rodriguez, H. Liu, J. Wu, and S. Chen, 'Metamorphic III-V semiconductor lasers grown on silicon', *MRS Bull*, vol. 41, no. 3, pp. 218–223, 2016, doi: 10.1557/mrs.2016.24.

[159] L. Seravalli *et al.*, 'Single quantum dot emission at telecom wavelengths from metamorphic InAs/InGaAs nanostructures grown on GaAs substrates', *Appl Phys Lett*, vol. 98, no. 17, pp. 1–4, 2011, doi: 10.1063/1.3584132.

[160] S. L. Portalupi, M. Jetter, and P. Michler, 'InAs quantum dots grown on metamorphic buffers as non-classical light sources at telecom C-band: A review', *Semicond Sci Technol*, vol. 34, no. 5, 2019, doi: 10.1088/1361-6641/ab08b4.

[161] Q. Lu, Q. Zhuang, A. Marshall, M. Kesaria, R. Beanland, and A. Krier, 'InSb quantum dots for the mid-infrared spectral range grown on GaAs substrates using metamorphic

InAs buffer layers', *Semicond Sci Technol*, vol. 29, no. 7, 2014, doi: 10.1088/0268-1242/29/7/075011.

[162] J. Yang *et al.*, 'Thin Ge buffer layer on silicon for integration of III-V on silicon', *J Cryst Growth*, vol. 514, no. February, pp. 109–113, 2019, doi: 10.1016/j.jcrysgro.2019.02.044.

[163] C. Shang *et al.*, 'Electrically pumped quantum-dot lasers grown on 300 mm patterned Si photonic wafers', *Light Sci Appl*, vol. 11, no. 1, pp. 1–8, 2022, doi: 10.1038/s41377-022-00982-7.

[164] W. Q. Wei *et al.*, 'Monolithic Integration of Embedded III-V Lasers on SOI', 2022.

[165] J. Selvidge *et al.*, 'Non-radiative recombination at dislocations in InAs quantum dots grown on silicon', *Appl Phys Lett*, vol. 115, no. 13, 2019, doi: 10.1063/1.5113517.

[166] S. Y. Hu *et al.*, 'Lateral carrier diffusion and surface recombination in InGaAs/AlGaAs quantum-well ridge-waveguide lasers', *J Appl Phys*, vol. 76, no. 8, pp. 4479–4487, 1994, doi: 10.1063/1.357279.

[167] D. Naidu, P. M. Smowton, and H. D. Summers, 'The measured dependence of the lateral ambipolar diffusion length on carrier injection-level in Stranski-Krastanov quantum dot devices', *J Appl Phys*, vol. 108, no. 4, 2010, doi: 10.1063/1.3471812.

[168] D. Bimberg *et al.*, 'InAs – GaAs Quantum Pyramid Lasers : In Situ Growth , Radiative Lifetimes and Polarization Properties', *Jpn. J. Appl. phys.*, vol. 35, pp. 1311–1319, 1995.

[169] A. Fiore *et al.*, 'Time-resolved optical characterization of InAs/InGaAs quantum dots emitting at 1.3 μm', *Appl Phys Lett*, vol. 76, no. 23, pp. 3430–3432, 2000, doi: 10.1063/1.126668.

[170] M. Gurioli, A. Vinattieri, M. Zamfirescu, M. Colocci, S. Sanguinetti, and R. Nötzel, 'Recombination kinetics of InAs quantum dots: Role of thermalization in dark states', *Phys Rev B Condens Matter Mater Phys*, vol. 73, no. 8, pp. 1–6, 2006, doi: 10.1103/PhysRevB.73.085302.

[171] P. D. Buckle *et al.*, 'Photoluminescence decay time measurements from self-organized InAs/GaAs quantum dots', *J Appl Phys*, vol. 86, no. 5, pp. 2555–2561, 1999, doi: 10.1063/1.371092.

[172] S. Osborne *et al.*, 'State filling in InAs quantum-dot laser structures', *IEEE J Quantum Electron*, vol. 40, no. 12, pp. 1639–1645, 2004, doi: 10.1109/JQE.2004.837331.

[173] E. Harbord, P. Spencer, E. Clarke, and R. Murray, 'The influence of size distribution on the luminescence decay from excited states of InAs/GaAs self-assembled quantum dots', *J Appl Phys*, vol. 105, no. 3, pp. 0–5, 2009, doi: 10.1063/1.3073934.

[174] I. Yonenaga and K. Sumino, 'Behaviour of dislocations in GaAs revealed by etch pit technique and X-ray topography', *J Cryst Growth*, vol. 126, no. 1, pp. 19–29, 1993, doi: 10.1016/0022-0248(93)90223-J.

[175] K. Mukherjee *et al.*, 'Kinetically limited misfit dislocations formed during post-growth cooling in III-V lasers on silicon', *J Phys D Appl Phys*, vol. 54, no. 49, 2021, doi: 10.1088/1361-6463/ac24c9.

[176] F. Grillot *et al.*, 'Physics and applications of quantum dot lasers for silicon photonics', *Nanophotonics*, vol. 9, no. 6, pp. 1271–1286, 2020, doi: 10.1515/nanoph-2019-0570.

[177] K. H. Chang, R. Gilbala, D. J. Srolovitz, P. K. Bhattacharya, and J. F. Mansfield, 'Crosshatched surface morphology in strained III-V semiconductor films', *J Appl Phys*, vol. 67, no. 9, pp. 4093–4098, 1990, doi: 10.1063/1.344968.

[178] M. A. Lutz, R. M. Feenstra, F. K. Legoues, P. M. Mooney, and J. O. Chu, 'Influence of misfit dislocations on the surface morphology of Si1-xGex films', *Appl Phys Lett*, vol. 66, p. 724, 1995, doi: 10.1063/1.114112.

[179] F. Hiwatashi and K. Yamaguchi, 'Selective growth of self-organizing InAs quantum dots on strained InGaAs surfaces', *Appl Surf Sci*, vol. 130–132, no. September 1997, pp. 737–741, 1998, doi: 10.1016/S0169-4332(98)00146-9.

[180] C. C. Thet, S. Sanorpim, S. Panyakeow, and S. Kanjanachuchai, 'The effects of relaxed InGaAs virtual substrates on the formation of self-assembled InAs quantum dots', *Semicond Sci Technol*, vol. 23, no. 5, pp. 3–8, 2008, doi: 10.1088/0268-1242/23/5/055007.

[181] T. Hakkarainen, A. Schramm, A. Tukiainen, R. Ahorinta, L. Toikkanen, and M. Guina, 'Lateral Ordering of InAs Quantum Dots on Cross-hatch Patterned GaInP', *Nanoscale Res Lett*, vol. 5, no. 12, pp. 1892–1896, 2010, doi: 10.1007/s11671-010-9747-2.

[182] A. E. Zhukov *et al.*, 'Injection Lasers Based on InGaAs Quantum Dots in an AlGaAs Matrix', 1998.

[183] A. Stintz, G. T. Liu, A. L. Gray, R. Spillers, S. M. Delgado, and K. J. Malloy, 'Characterization of InAs quantum dots in strained In[sub x]Ga[sub 1−x]As quantum wells', *Journal of Vacuum Science & Technology B: Microelectronics and Nanometer Structures*, vol. 18, no. 3, p. 1496, 2000, doi: 10.1116/1.591412.

[184] L. Seravalli, G. Trevisi, and P. Frigeri, '2D-3D growth transition in metamorphic InAs/InGaAs quantum dots', *CrystEngComm*, vol. 14, no. 3, pp. 1155–1160, 2012, doi: 10.1039/c1ce06192e.

[185] A. G. Cullis, D. J. Norris, T. Walther, M. A. Migliorato, and M. Hopkinson, 'Stranski-Krastanow transition and epitaxial island growth', *Phys Rev B Condens Matter Mater Phys*, vol. 66, no. 8, pp. 1–4, 2002, doi: 10.1103/PhysRevB.66.081305.

[186] C. Heidelberger *et al.*, 'Efficient Optical Coupling between III-V Semiconductor and SiNxWaveguides via Heteroepitaxial Integration', *2021 IEEE Photonics Conference, IPC 2021 - Proceedings*, no. 111, pp. 21–22, 2021, doi: 10.1109/IPC48725.2021.9593053.

[187] M. Müller, A. Cerezo, G. D. W. Smith, L. Chang, and S. S. A. Gerstl, 'Atomic scale characterization of buried InxGa1-xAs quantum dots using pulsed laser atom probe tomography', *Appl Phys Lett*, vol. 92, no. 23, p. 233115, 2008, doi: 10.1063/1.2918846.

[188] A. D. Giddings *et al.*, 'Composition profiling of InAs quantum dots and wetting layers by atom probe tomography and cross-sectional scanning tunneling microscopy', *Phys Rev B*, vol. 83, p. 205308, 2011, doi: 10.1103/PhysRevB.83.205308.

[189] P. Wang, A. L. Bleloch, M. Falke, P. J. Goodhew, J. Ng, and M. Missous, 'Direct measurement of composition of buried quantum dots using aberration-corrected scanning transmission electron microscopy', *Appl Phys Lett*, vol. 89, no. 7, 2006, doi: 10.1063/1.2335361.

[190] Q. Li and K. M. Lau, 'Epitaxial growth of highly mismatched III-V materials on (001) silicon for electronics and optoelectronics', *Progress in Crystal Growth and Characterization of Materials*, vol. 63, no. 4, pp. 105–120, 2017, doi: 10.1016/j.pcrysgrow.2017.10.001.

[191] J. Selvidge *et al.*, 'Reduced dislocation growth leads to long lifetime InAs quantum dot lasers on silicon at high temperatures', *Appl Phys Lett*, vol. 118, no. 19, p. 192101, May 2021, doi: 10.1063/5.0052316.

[192] H. Saito and T. Kawakami, 'The New Origin of Dark-Line Defects in Planar-Stripe DH Lasers', *IEEE J Quantum Electron*, vol. 13, no. 8, pp. 564–567, 1977.

[193] M. J. Robertson, B. Wakefield, and P. Hutchinson, 'Strain-related degradation phenomena in long-lived GaAlAs stripe lasers', *J Appl Phys*, vol. 52, no. 7, pp. 4462–4466, 1981, doi: 10.1063/1.329372.

[194] K. Kondo, O. Ueda, S. Isozumi, S. Yamakoshi, K. Akita, and T. Kotani, 'Positive Feedback Model of Defect Formation in Gradually Degraded GaAIAs Light Emitting Devices', *IEEE Trans Electron Devices*, vol. 30, no. 4, pp. 321–326, 1983, doi: 10.1109/T-ED.1983.21124.

[195] J. H. Neethling, A. Janse Van Vuuren, E. J. Olivier, and P. A. Van Aken, 'TEM and HAADF STEM imaging of dislocation loops in irradiated gaas', *Acta Phys Pol A*, vol. 136, no. 2, pp. 245–249, 2019, doi: 10.12693/APhysPolA.136.245.

[196] Z. Xiangjie, L. Xiang, L. Guanlin, S. Ling, Z. Shiyong, and Q. Haihua, 'Highly reliable quantum dot laser directly grown on CMOS compatible Si (001) substrate', *2023 Optical Fiber Communications Conference and Exhibition (OFC)*, 2023, doi: 10.23919/OFC49934.2023.10116887.

[197] R. Jones, A. Umerski, P. Sitch, M. I. Heggie, and S. Öberg, 'First-Principles Calculations of Dislocations in Semiconductors', *physica status solidi (a)*, vol. 137, no. 2, pp. 389–399, 1993, doi: 10.1002/pssa.2211370211.

[198] C. Shang *et al.*, 'Design Rules for Addressing Material Asymmetry Induced by Templated Epitaxy for Integrated Heteroepitaxial On-Chip Light Sources', *Adv Funct Mater*, 2023, doi: 10.1002/adfm.202304645.

[199] M. Uematsu and K. Wada, 'Time dependence of recombination-enhanced impurity diffusion in GaAs', *Appl Phys Lett*, vol. 60, no. 13, pp. 1612–1614, 1992, doi: 10.1063/1.107217.

[200] P. J. Phillips, M. C. Brandes, M. J. Mills, and M. de Graef, 'Diffraction contrast STEM of dislocations: Imaging and simulations', *Ultramicroscopy*, vol. 111, no. 9–10, pp. 1483–1487, 2011, doi: 10.1016/j.ultramic.2011.07.001.

[201] D. Hull and D. J. Bacon, *Introduction to Dislocations*, Fifth. Oxford: Elsevier, 2011.

[202] O. Ueda, S. Isozumi, S. Yamakoshi, and T. Kotani, 'Defect structure of degraded Ga1-xAlxAs double-heterostructure light-emitting diodes', *J Appl Phys*, vol. 50, no. 2, pp. 765–772, 1979, doi: 10.1063/1.326042.

[203] O. Ueda, 'Reliability issues in III-V compound semiconductor devices: optical devices and GaAs-based HBTs', *Microelectronics Reliability*, vol. 39, pp. 1839–1855, 1999, [Online]. Available: www.elsevier.com/locate/microrel

[204] M. Zenari *et al.*, 'Identification of dislocation-related and point-defects in III-As layers for silicon photonics applications', *J Phys D Appl Phys*, vol. 54, no. 28, 2021, doi: 10.1088/1361-6463/abf9dc.

[205] M. Buffolo *et al.*, 'Origin of the Diffusion-Related Optical Degradation of 1.3 µm Inas QD-LDs Epitaxially Grown on Silicon Substrate', *IEEE Journal of Selected Topics in Quantum Electronics*, vol. 28, no. 1, pp. 1–9, 2022, doi: 10.1109/JSTQE.2021.3091960.

[206] C. Jiang *et al.*, 'Reliability enhancement of InGaAs/AlGaAs quantum-well lasers on on-axis Si (001) substrate', *APL Mater*, vol. 11, no. 9, Sep. 2023, doi: 10.1063/5.0162387.

[207] W. J. Fritz, L. B. Bauer, and C. S. Miller, 'Analysis of aluminum gallium arsenide laser diodes failing due to nonradiative regions behind the facets', in *Proceedings: International Reliablity Physics Symposium*, IEEE, 1989, p. 59. [Online]. Available: https://ieeexplore.ieee.org/document/36318

[208] R. G. Waters, 'Diode laser degradation mechanisms: A review', *Prog Quantum Electron*, vol. 15, no. 3, pp. 153–174, 1991, doi: 10.1016/0079-6727(91)90004-2.

[209] E. T. Hughes *et al.*, 'Dislocation Formation and Filtering in III-V Regrowth on GaAs Bonded on Si', *Cryst Growth Des*, vol. 22, pp. 5852–5860, 2022, doi: 10.1021/acs.cgd.2c00309.

[210] E. T. Hughes *et al.*, 'Dislocation-Induced Structural and Luminescence Degradation in InAs Quantum Dot Emitters on Silicon', *physica status solidi (a)*, 2023, doi: 10.1002/pssa.202300114.